Using Solar-sail Induced Dynamics to Increase the Warning Time for Solar Storms Heading Towards Earth

Master Thesis

Niels Bakx

Delft University of Technology

TU Delft

Using Solar-sail Induced Dynamics to Increase the Warning Time for Solar Storms Heading Towards Earth

Master Thesis

by

Niels Bakx

to obtain the degree of Master of Science
at the Delft University of Technology,
to be defended publicly on Friday September 24th, 2021 at 10:00 AM.

Student number:	4559975	
Project duration:	January 11, 2021 – September 24, 2021	
Supervisor:	Dr. M. J. Heiligers	
Thesis committee:	Dr.ir. W. van der Wal,	Committee chair
	Dr. M. J. Heiligers,	Supervisor
	Dr. A. Menicucci	External Examinator

Cover image credits: J.J. de Haan, NASA/SDO, Planetary Society
www.nasa.gov/subject/3165/space-weather/, www.planetary.org/

This thesis is confidential and cannot be made public until September 24, 2021.

TU Delft

Preface

Space flight has been a passion of mine for as long as I can remember. This made the decision of going to Delft, studying Aerospace engineering, and a thesis in a space topic very easy. I became familiar with the concept of solar sailing during my studies and it immediately amazed me. While ”riding on a beam of light” seems to only exist in science fiction movies, the concept has actually flown and proven to work. I feel very lucky to have had the opportunity to apply the concept of solar sailing in my thesis work and I sincerely hope that this work can contribute to the body of knowledge of (solar-sail) trajectories for solar-storm detection.

Before you are to (hopefully) enjoy my thesis work, I want to highlight some people that have raised this work to another level. First, I want to thank my friends and family for being the rubber duck[1] by listening to my unsolicited talks, which were essentially me thinking out loud. Next to that, I would like to thank Jeannette for her supervision, dedication, valuable input, and fun talks throughout this thesis project. Our weekly meetings were essential in steering me in the right way. Thanks to Jeannette, this work has been submitted to the CEAS Aerospace Europe Conference 2021.

Niels Bakx
Delft, September 2021

[1] Retrieved from https://rubberduckdebugging.com/. Date accessed: 02-09-2021.

Abstract

Coronal Mass Ejections (CMEs), also called solar storms, that are on a trajectory to intersect the Earth may cause, among others, the breakdown of power grid transformers, the malfunction of Earth-orbiting spacecraft, and disruptions in navigation and communication systems. The impact of a solar storm is predicted to be in the order of trillions of euros and there is a probability of 12% that such an event occurs within a decade. Nowadays, society is getting more and more dependent on technology which leads to an ever-increasing impact. It is therefore essential that society becomes aware of an approaching storm in a timely manner, predicted to be two to three days, such that sufficient measures can be taken to mitigate the impact. These storms are currently detected by spacecraft at or near the Sun-Earth L_1 point. Because of the difference in time between the solar-storm arrival and the spacecraft warning signal reception at Earth, a warning time of 30 to 60 minutes is achieved. This warning time can be increased by placing a spacecraft further upstream of the CME propagation path, i.e., closer to the Sun.

This thesis work aims to do exactly what is written in the previous sentence, by designing periodic trajectories that travel upstream of the CME propagation path by using a solar sail as sole propulsion device. Due to the propellant-less nature of a solar sail, the trajectories can be maintained as long as the operational lifetime of the spacecraft equipped with a solar sail. The propellant-less feature is achieved by reflecting photons off a highly reflective membrane, generating a continuous thrust. Previous work aiming to increase the warning time for solar storms considered the use of heteroclinic connections between Artificial Equilibrium Points (AEPs) in the vicinity of the sunwards solar-sail displaced L_1 (SL_1) point. The results showed that an average increase in warning time of approximately a factor 15 can be obtained. This work builds on that work by also considering heteroclinic connections with AEPs in the vicinity of the SL_5 point, thereby opening up the possibility of increasing the warning time even further. These trajectories are found by defining the problem as an optimal control problem and will be solved in $\mathcal{PSOPT}$, a particular implementation of a direct pseudospectral method. An initial guess is required and consists of heteroclinic connections between AEPs in the vicinity of the SL_1 and SL_5 point. These connections utilise a piece-wise constant (solar-sail) steering law, which is obtained by a grid search and genetic algorithm.

The optimal control problem utilises an objective function that comprises three elements: maximisation of the average and maximum increase in warning time along the trajectory and minimisation of the distance to the CME-axis. The last element results in maximising the probability that a spacecraft in the trajectory detects a CME, as not all CMEs have the same shape. By defining the relative importance between the three elements, a periodic solar-sail trajectory can be obtained that satisfies a particular requirement or preference. With one spacecraft available and employing an ideal solar-sail model, near-term solar-sail technology (a lightness number of 0.05) can achieve a maximum increase in warning time equal to approximately a factor 29.5 without compromising the other two elements. In addition, an inverse relationship exists between maximisation of the average increase in warning time and maximisation of the probability of CME detection. This correlation is indicated by a particular set of trajectories that have an average increase in warning time and a probability of CME detection of [28.5, 49%], [24.2, 72%], [19.1, 89%], and [10.5, 100%]. In addition, the implementation of solar-sail optical imperfections yields a modest impact of at most 2.5% on the performance of a trajectory. The small impact may be attributed to the small control effort of the periodic solar-sail trajectories (a maximum value of the solar-sail pitch angle, α, of $\pm$ 18 deg). Furthermore, advances in solar-sail technology are assessed by increasing the solar-sail lightness number: an increase of 0.01 results in a performance increase of 1% to 8%, depending on the objective parameter and the nature of the trajectory.

Despite the promising results, the warning time that is achieved by a spacecraft in a periodic solar-sail trajectory from this thesis work does not fulfil the time requirement to prepare society for an approaching solar storm. However, it is suspected that the combination of a solar-sail spacecraft in a trajectory as designed in this thesis together with a spacecraft to predict CME events, such as a spacecraft in the vicinity of the L_5 point, provides a sufficiently prompt and accurate warning signal.

Contents

Nomenclature

Abbreviations

AEP	Artificial Equilibrium Point
AIAA	American Institute of Aeronautics and Astronautics
AU	Astronomical Unit
CME	Coronal Mass Ejection
CRTBP	Circular Restricted Three-Body Problem
ERTBP	Elliptical Restricted Three-Body Problem
GA	Genetic Algorithm
LGL	Legendre-Gauss-Lobatto
PCRTBP	Planar Circular Restricted Three-Body Problem
PSOPT	Pseudospectral Optimisation
RPS	Region of Practical Stability
SEP	Solar Energetic Particle
SL_1	Sub-Lagrange point 1
SL_5	Sub-Lagrange point 5
UD	Unit Distance

Latin symbols

$I - IV$	Selection of optimised trajectories
A	Jacobian
a	Acceleration
B_f, B_b	Front and back non-Lambertian coefficients
$C(x, y, z)$	Synodic reference frame
d	Distance to CME-axis
F	Force
J	Objective function
k	Increase in warning time with respect to current missions at L_1
l	Radial coordinate coronal mass ejection
m	Mass
$\hat{\vec{m}}$	Solar-sail acceleration total unit direction
N	Number of Legendre-Gauss-Lobatto nodes
n	Coefficient of front flattening
N_1	Initial guess trajectory 1
N_2	Initial guess trajectory 2
$\hat{\vec{n}}$	Solar-sail acceleration normal unit direction
P	Probability of CME detection
$P(l, \gamma)$	Polar reference frame
q	Objective function boolean
Q_p	Objective function boolean
r	Position
R_t	Toroidal height
$\tilde{r}$	Reflectivity coefficient
s	Specular reflection coefficient
T	Trajectory period
t	Time
$\hat{\vec{t}}$	Solar-sail acceleration tangent unit direction
U	Effective potential
u	Control
$\tilde{U}$	Modified effective potential
v	Velocity
w	Objective function weight
x, y, z	Position coordinates in the CRTBP
$\vec{x}$	Spacecraft state

Greek symbols

α	Solar-sail pitch angle

$\tilde{\alpha}$	Real part of eigenvalue
β	Solar-sail lightness number
$\tilde{\beta}$	Imaginary part of eigenvalue
γ	Angular coordinate coronal mass ejection
γ_{hw}	Half-width angle
ϵ	Linear perturbation
ϵ_f, ϵ_b	Front and back emissivity coefficients
θ	Solar-sail cone angle
$\tilde{\theta}$	Hyper-plane angle
λ	Eigenvalue
μ	Mass ratio
$\vec{v}$	Eigenvector
$\sum$	Hyper-plane
ϕ	Angle between the solar-sail normal and total acceleration vector
ω	Angular velocity

Subscripts

avg	Average
id	Ideal solar-sail model
max	Maximum
opt	Optical solar-sail model
p	Point
RS	Radial size
s	Solar sail
sc	Spacecraft

Superscripts

$\ddot{}$	Second-order differentiation with respect to time
$\dot{}$	First-order differentiation with respect to time
$\hat{}$	Unit vector
$\vec{}$	Vector

Other symbols

$\mathcal{O}$	In the order of
$\mathcal{T}$	Stability class
∇	Gradient operator

1 Introduction

This chapter introduces the thesis work. At first, the relevancy is highlighted in Sec. 1.1 by giving an overview of the problem at hand: the need for an increase in solar-storm warning time. After that, the concept of solar sailing is outlined in Sec. 1.2, which is considered in this thesis to solve the problem at hand. Subsequently, Sec. 1.3 defines the research objective and questions. Finally, the structure of this report is given in Sec. 1.4.

1.1. Space Weather

The space between the Sun and the Earth is not as empty as humans had imagined in the 1950s [1]. It is estimated that every second the Sun emits approximately one million tonnes (10^9 kg) of charged particles outwards, called the solar wind, into its environment [2]. The outer atmosphere of the Sun, the corona, is so hot that the pressure is larger than the Sun's own gravity, leading to the outflow of the wind. The solar wind creates the interplanetary magnetic field as it carries the Sun's magnetic field into space, interacting with all bodies in the solar system, including Earth. Usually, the Sun's activity does not harm Earth's environment, as Earth's magnetosphere and atmosphere protect it from solar wind activities [2]. However, the Sun's activity is neither uniform nor steady so (large) disturbances can create peaks in energy releases that may impose a risk on Earth's environment [2]:

- *Solar flares* are outbursts of radiation from the Sun in the order of 10^{19} J to 10^{25} J and can affect Earth's ionosphere, leading to disruptions in, for instance, navigation and communication signals. These outbursts might be responsible for large restructuring of the magnetic field in the Sun's corona resulting in larger Sun activity events, which are listed below [1, 3].
- *Solar Energetic Particles* (SEPs) form due to the dynamic processes in the coronal and interplanetary plasma that highly accelerate charged particles; protons, electrons, and ions ranging from a few keV to GeV. SEPs can reach velocities up to half the speed of light, arriving at Earth a few minutes later. They can lead to the malfunctioning of spacecraft hardware outside the magnetosphere and an increase in the radiation dose of astronauts [1].
- *Coronal Mass Ejections* (CMEs), also known as solar storms, are explosive releases of plasma from the corona into the solar system. These ejections have a mass of typically 10^{11} kg to 10^{13} kg and are the strongest contributor to space weather [2]. If they are on a trajectory to intersect the Earth, they can interact with Earth's magnetic field, which may ultimately lead to geomagnetic storms that induce an electric current in wires and temporarily increase the radiation dose for humans [4].

The focus of this study will be on the detection of CMEs, as these are the strongest contributor to space weather. A solar storm can, among others, cause the breakdown of power grid transformers, the malfunctioning of Earth-orbiting spacecraft, and disruptions in navigation and communication systems [5]. Reference [6] has predicted a 12% chance of a solar storm occurring within a decade, making it a realistic event in a lifetime. The impact of such a solar storm may be in the order of trillions of euros [7, 8]. As society is getting more and more dependent on technology, it is expected that the impact of

a solar storm will only increase over the years. It is therefore essential that a solar storm is detected with sufficient warning time, such that adequate measures can be taken to mitigate the impact.

Currently, solar storms are detected by spacecraft orbiting the Sun-Earth L_1 point, such as SOHO (ESA/NASA, 1995), ACE (NASA, 1997), WIND (NASA, 2004), and the Deep Space Climate Observatory (NOAA/NASA, 2015) [9]. Due to the difference in time between a solar storm arriving at Earth and the spacecraft warning signal reception at Earth, a solar-storm warning time of 30 to 60 minutes can be achieved [10]. Consequently, this warning time can be increased by placing a spacecraft upstream of the path of the CME, i.e., closer to the Sun, thereby allowing for an earlier detection compared to current missions. It is estimated that two to three days are required to fully prepare for solar-storm disruption, which indicates the scope for improvement compared to a current warning time of 30 to 60 minutes [11]. The concept of solar sailing may aid in placing a spacecraft further upstream, which will be elaborated upon in the next section.

1.2. Solar Sailing

The first practical ideas of using a solar sail date back 100 years ago, to 1920. Tsiolkovsky and Tsander discussed using ”tremendous mirrors of very thin sheets” for mission applications [10]. It was not until 1950 that this concept was published in popular literature. Finally, in 2010, the first solar sail was successfully deployed by JAXA: the IKAROS mission [12]. Not much later NASA launched its first successful solar-sail mission: NanoSail-D2 [13]. The Planetary Society added LightSail-1 and -2 to the list of successful solar-sail missions in 2015 and 2019, respectively [14]. Planned solar-sail missions are NASA’s NEA Scout (end 2021) and JAXA’s OKEANOS (2026) mission [15, 16].

Solar sails have become increasingly popular because of their propellant-less nature: by reflecting solar photons off a highly reflective sail membrane, a continuous form of thrust is generated [10]. As opposed to traditional propulsion methods, solar sails do not require propellant to generate thrust. The continuous solar-sail thrust may reduce mission costs as the need for propellant is reduced/eliminated, which leads to the decrease in launch mass. In addition to that, new mission applications that were previously deemed infeasible can become a reality [4, 10].

The continuous solar-sail acceleration may aid in the field of solar-storm detection in several ways. Firstly, this acceleration results in a sunwards shift of the Sun-Earth L_1 point, called the SL_1 (sub-L_1) point. As this equilibrium point is closer to the Sun and therefore closer to the origin of the CME, a spacecraft at or near this location may achieve an increase in warning time of approximately a factor 1.8 compared to current missions at L_1 [9]. Furthermore, by tilting the solar sail with respect to the Sun-Earth line, the continuous solar-sail acceleration vector is tilted as well. This allows for a surface of Artificial Equilibrium Points (AEPs). Solar-sail assisted manifolds originating from the AEPs (including the SL_1 point) may allow for the spacecraft to travel even further upstream of the CME propagation path, thereby potentially increasing the solar-storm warning time significantly [17].

There has not yet been an actual solar-sail mission dedicated to solar-storm detection but theoretical studies have shown the potential. In particular, NASA’s Geostorm and Sunjammer mission concepts were designed to be in an orbit about the SL_1 point (achieving an increase in solar-storm warning time of a factor 1.8 with respect to current missions at the L_1 point) [9, 10]. Furthermore, a mission concept relying on so-called SpaceChips utilised the unstable sunward solar-sail assisted manifolds of a halo orbit, which allowed an increase in solar-storm warning time of a factor nine [18, 19]. Although a significant increase in warning time, the main downside of constantly replenishing the manifold with high area-to-mass spacecraft deems this mission concept impractical or infeasible for longer mission durations. To resolve this, a *periodic* solar-sail trajectory should exist that allows the solar-sail spacecraft to travel upstream of the CME propagation path after which it returns to its initial state. Then, the same trajectory can be repeated and, due to the propellant-less nature of a solar sail, be maintained as long as the lifetime of the spacecraft and solar sail. The feasibility of a solar-sail periodic trajectory has been shown by Ref. [17]. This reference found an average increase in solar-storm warning time of approximately a factor 15 by using heteroclinic connections between AEPs in the vicinity of the SL_1 point, as displayed by the solid *PSOPT-2 trajectory* line in Fig. 1.1.

This thesis work will build on the current body of knowledge regarding solar-storm detection by looking for periodic solar-sail trajectories in the vicinity of the SL_1 *and* SL_5 point, which may result in a larger increase in solar-storm warning time as the trajectory may cross the CME-axis further upstream. A graphical impression of such a trajectory is presented in Fig.1.2. An optimal control problem is defined

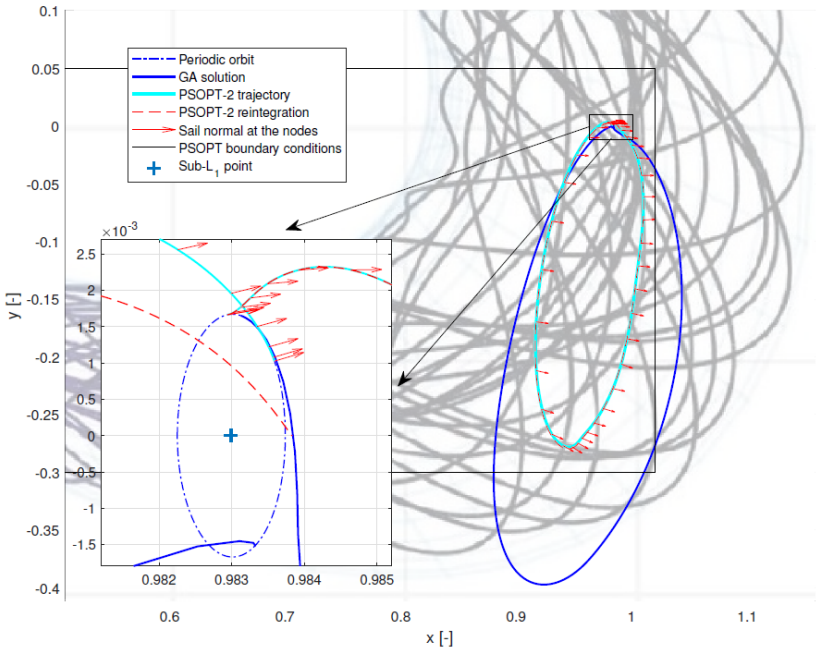

Figure 1.1: The solar-sail trajectory (cyan) that achieves an average increase in solar-storm warning time of a factor 15 retrieved from Ref. [17].

and will be solved in $\mathcal{PSOPT}$, a particular implementation of a direct pseudospectral method [20]. This method requires an initial guess trajectory and consists of heteroclinic connections between AEPs in the vicinity of the SL_1 and SL_5 point. The piece-wise constant steering law of the solar sail on the spacecraft is obtained by a grid search and genetic algorithm.

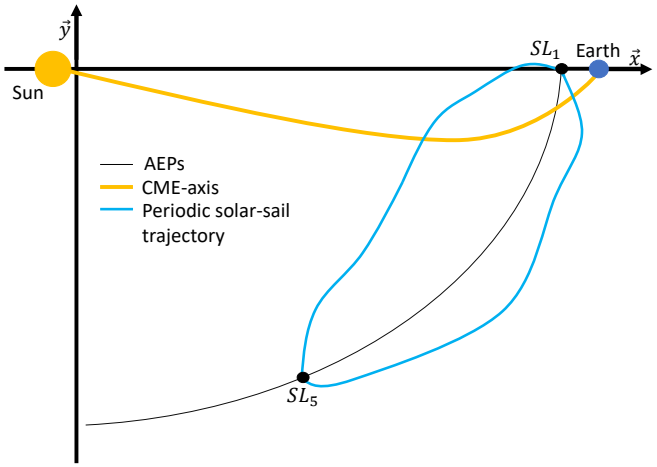

Figure 1.2: Graphical overview of a periodic solar-sail trajectory in the vicinity of the SL_1 and SL_5 point.

1.3. Research Questions

The previous sections outlined the relevancy of solar-storm detection and the potential role of solar sailing in it. As a result, the focus of the thesis work will be on finding periodic solar-sail trajectories that increase the solar-storm warning time with respect to current missions at the Sun-Earth L_1 point. To achieve this, a research objective is defined, which is formulated as

To increase the warning time for solar storms heading towards the Earth with respect to current mission (designs) by designing a periodic solar-sail trajectory that travels as far as possible upstream

of the CME-axis.

This objective can be achieved by answering the following research questions:

A) How can heteroclinic(-like) connections between solar-sail displaced equilibrium points in the vicinity of the SL_1 and SL_5 point be used to generate a trajectory that travels upstream of the CME-axis using a piecewise-constant sail attitude?

B) Can the piecewise-constant sail attitude profile be optimised to a continuously varying sail attitude profile to improve the performance of the solar-storm detection trajectories?

C) What is the effect of including optical imperfections in the solar-sail model on the performance of the solar-storm detection trajectories?

D) What is the effect of mid- to far-term advances in solar-sail technology on the performance of the solar-storm detection trajectories?

1.4. Report Outline

The research questions outlined in the previous section will be addressed in Ch. 2, the main part of the thesis report. This chapter is written in a journal article format. In particular, it is written in a format according to the American Institute of Aeronautics and Astronautics (AIAA), which publishes the Journal of Guidance, Control, and Dynamics, a monthly peer-reviewed scientific journal. Writing it in this form allows for the readiness to submit the thesis to this journal. The journal article is titled *Using Solar-sail Induced Dynamics to Increase the Warning Time for Solar Storms Heading Towards Earth* and begins with another abstract and introduction in Section I, which is a more compact version of the ones that were outlined in this chapter of the thesis report. After that, an overview of the dynamics and models that are used in the thesis are presented in Section II. In Section III the article continues by generating initial-guess trajectories that are used in Section IV to solve the optimal control problem. The main results of the thesis are also presented here. The technical part ends with a sensitivity analysis on the model choices that were made at the beginning of the thesis in Section V. Finally, the journal article ends with the conclusions in Section VI. After the journal article, the thesis report continues with the conclusions and recommendations in which, among others, the research questions will be answered and suggestions will be made for work that can be done as a follow-up study in Ch. 3. Subsequently, Appendix A presents the verification and validation of the models and numerical techniques which are used throughout the thesis. The thesis report ends with Appendix B displaying additional computations to support the thesis results.

2

Journal Article

Using Solar-sail Induced Dynamics to Increase the Warning Time for Solar Storms Heading Towards Earth

N.K.M. (Niels) Bakx*
Delft University of Technology, Delft, Zuid-Holland, 2629HS, The Netherlands

This paper investigates the use of solar-sail technology to increase the warning time for Coronal Mass Ejections (CMEs) heading towards Earth. In addition, this research will build upon the current understanding of using solar-sail dynamics with regards to CME detection by providing insights into the problem characteristics. The warning time is proportional to the distance from the Earth to the spacecraft detecting the CME: a current warning time of 30 to 60 minutes is achieved by satellites at or near the Sun-Earth L_1 point. By considering the actual shape of a CME, the continuous solar-sail acceleration from the solar sail can be used to find a periodic trajectory that travels further upstream of the CME-axis, thereby increasing the warning time with respect to current missions. Finding a periodic solar-sail trajectory can be regarded as an optimal control problem, which requires a near-feasible initial guess trajectory. the latter is found by generating heteroclinic connections between artificial equilibrium points in the vicinity of the sub-L_1 and sub-L_5 point through the use of a grid search and a genetic algorithm. The optimal control problem is solved with a direct pseudospectral method, resulting in four representative trajectories, each having specific (dis)advantages. The performance impact due to (the uncertainty of) non-ideal sail properties, change in lightness number, and variation in CME size are investigated. Ultimately, the most optimal trajectory increases the average and maximum warning time by a factor 20 and 30 with respect to current missions at L_1, respectively, with a 90% probability that the spacecraft detects the CME.

I. Introduction

SPACE weather caused by the Sun can have serious consequences on Earth and its society [1]. Explosive releases of plasma, also called Coronal Mass Ejections (CMEs) or solar storms, that are headed towards Earth interfere with Earth's magnetic field and, among others, expose humans to a larger dose of radiation, disrupt communication and navigation systems, and induce an electric current in wires. If the CME is strong enough, this electric current can, for example, cause power grids to break down and cause Earth-orbiting spacecraft to malfunction [2]. The economic impact of such a solar storm is predicted to be in the order of trillions of euros and the chance of an occurrence of a

*Graduate Student, Department of Astrodynamics and Space Missions, Faculty of Aerospace Engineering, niels.bakx@live.nl

strong solar storm is estimated to be 12% in a decade, making it a realistic occurrence in a lifetime [3–5]. Combined with the fact that there is an increasing dependency in society on technology, it is essential that people receive a timely warning of an approaching solar storm so that adequate measures can be taken to mitigate the impact. It is estimated that two to three days are required to prepare for disruption [6].

Currently, solar storms are detected and warned for by spacecraft orbiting the Sun-Earth L_1 point such as SOHO (ESA/NASA, 1996), ACE (NASA, 1997), WIND (NASA, 2004), and DSCOVR (NOAA/NASA, 2015) [7]. Due to the difference in time between the solar-storm arrival and the spacecraft warning signal reception at Earth, a solar-storm warning time of 30 to 60 minutes can typically be achieved [8]. Consequently, the solar-storm warning time can be increased if the CME is detected further upstream of its propagation path, i.e., closer to the Sun. A solar sail can be utilised to this end by exploiting the continuous solar-sail acceleration to shift the Sun-Earth L_1 point sunward, called the SL_1 (sub-L_1) point [8]. This continuous acceleration results from the reflection of solar photons off a highly reflective membrane, which is, as opposed to conventional methods that depend on expelling mass, only limited by the lifetime of the sail [8]. In addition to a sunwards shift of the L_1 point, solar-sail assisted manifolds of the SL_1 point may be able to substantially increase the solar-storm warning time by allowing the spacecraft to travel even further upstream of the CME propagation path [9].

The first practical ideas of using a solar sail date back to 1920, when Tsiolkovsky and Tsander discussed using "tremendous mirrors of very thin sheets" [8]. In 2010, solar sailing became a reality by the successful launch of JAXA's IKAROS mission, followed by NASA's NanoSail-D2 mission in the same year [10, 11]. These missions were later followed by LightSail-1 (2015) and -2 (2019) from The Planetary Society [12]. Planned missions are NASA's NEA Scout (2021) and JAXA's OKEANOS (2026) [13, 14].

There has not yet been an actual solar-sail mission dedicated to solar-storm detection. However, theoretical studies show promising results of an increase in solar-storm warning time using the concept of solar sailing. In particular, NASA's Sunjammer and the Geostorm mission were designed to be stationed in an orbit about the Sun-Earth SL_1 point, allowing for an increase in solar-storm warning time of almost a factor two compared to traditional missions at the Sun-Earth L_1 point [7, 8]. Another concept exploits the unstable sunward manifold of a solar-sail halo orbit around the Sun-Earth SL_1 point to travel upstream of a CME by constantly replenishing the manifold with small high area-to-mass ratio spacecraft, also called SpaceChips [15, 16]. As there will always be a spacecraft upstream of the CME path, an increase in solar-storm warning time of approximately a factor nine can be achieved compared to mission designs that remain relatively close to the SL_1 point [15]. The main downside of this mission concept is that the lifetime of the mission is restricted by the number of SpaceChips. In addition, note that all these studies assumed that a CME propagates along the Sun-Earth line. A study that considered the actual shape of a CME while it propagates through interplanetary space is Ref. [9], which proposed the use of homo- and heteroclinic connections between Artificial Equilibrium Points (AEPs) in the vicinity of the Sun-Earth SL_1 point to increase the solar-storm warning time [17].

This concept resulted in an average increase in solar-storm warning time of approximately a factor 15 compared to current missions at the L_1 point, which is a substantially larger increase than what is achieved by the Sunjammer and Geostorm mission concept [9]. Furthermore, as opposed to the work in Ref. [15, 16], the trajectory is periodic, meaning that a constant replenishment of spacecraft is not required.

The results of Ref. [9] were promising, but only considered heteroclinic connections in the vicinity of the SL_1 point, thereby potentially restricting the search space too much; the increase in warning time may be further increased by considering heteroclinic connections with AEPs in the vicinity of the SL_5 point as well. Consequently, this study will focus on finding solar-sail periodic trajectories that consist of heteroclinic connections between AEPs in the vicinity of the SL_1 and SL_5 point to increase the solar-storm detection time with respect to current missions at the Sun-Earth L_1 point. A grid search and genetic algorithm is used to generate these trajectories. At the same time, insights into the problem characteristics are provided to build upon the current knowledge of using solar-sail dynamics with regards to solar-storm detection.

The solar-sail periodic trajectories may be further optimised by defining an optimal control problem. The objective of the optimal control problem defined in this work consists of three performance metrices: the average increase in warning time along the trajectory, the average distance to the CME-axis, and the maximum increase in warning time at any point along the trajectory. Consequently, different optimal trajectories can be found by specifying the relative importance of each property. An open-source direct pseudospectral algorithm, $\mathcal{PSOPT}$, is used to solve the optimal control problem [18]. The algorithm requires an (almost-)feasible initial guess trajectory for initiation, which, comprises the results of the grid search and genetic algorithm.

The structure of this paper is as follows. First, Section II presents an overview of the dynamics and the models that are used in the study. In addition, it presents some first order insights into the solar-sail dynamics that can be used in the determination of a trajectory suitable for solar-storm detection. Section III uses these insights to generate (initial-guess) solar-sail periodic trajectories while at the same time build on the current understanding of exploiting solar-sail dynamics for solar-storm detection. These initial guess trajectories are used as an input to the optimal control problem that is defined in Section IV. In addition, this section presents the results to the optimal control problem. Subsequently, Section V performs a sensitivity analysis on the models and parameters that have been used in the analysis, in particular, the solar-sail model, the CME size, and the solar-sail lightness number*. Finally, the paper ends with the conclusions in Section VI.

II. Dynamics

This section presents the models that will be utilised in the remainder of the paper. In particular, the dynamical model, the solar-sail model, and the CME-model are discussed. Moreover, this section will present the effects of the

*The lightness number is defined as the ratio between the solar radiation pressure acceleration and the solar gravitational acceleration [8].

addition of a solar-sail acceleration to the classical (i.e., unperturbed) dynamics and its potential usefulness with regards to solar-storm detection. Each section presents a model or insight that acts as a building block to be able to generate periodic solar-sail trajectories suitable for solar-storm detection in the next sections.

A. Dynamical Model

Following the approach taken in previous studies [7, 9], the Sun-Earth Circular Restricted Three-Body Problem (CRTBP) is adopted as the dynamical model. In particular, a two-dimensional formulation, referred to as the planar CRTBP (PCRTBP), is employed as a CME that is headed towards Earth shows a clear correlation between its path and the ecliptic plane (more information on this is given in Section II.C) [17]. As a result, limiting this study to the motion of a solar-sail spacecraft in the ecliptic plane is justified. The PCRTBP describes the two-dimensional motion of an infinitesimally small mass (spacecraft), m, under the gravitational influence of the masses of the two primaries: the Sun's mass, m_1, and the Earth's mass, m_2. The gravitational influence of the spacecraft on the two primaries is neglected. In addition, it is assumed that the Sun and the Earth move in circular orbits about the barycenter of the system. A graphical overview of the dimensionless Sun-Earth PCRTBP can be seen in Fig. 1.

The reference frame that is used is a synodic reference frame, $C(x, y, z)$, with the origin C at the barycenter, the x-axis is oriented alongthe line from the Sun to the Earth, the z-axis in the direction perpendicular to the ecliptic plane, and the y-axis in the direction to complete the right-handed reference frame. The frame rotates around the z-axis at a constant angular velocity of $\vec{\omega} = \omega\hat{\vec{z}}$ equal to the angular velocity of the Earth around the Sun.

The PCRTBP can be made dimensionless by defining a mass ratio, μ, as [8]

$$\mu = \frac{m_2}{m_1 + m_2} \tag{1}$$

and is equal to 3.0404x10^{-6} in the Sun-Earth system. The unit of mass is set equal to the sum of the masses of the Sun and the Earth and the unit of length as the distance between the Sun and the Earth. Using Eq. (1), the dimensionless masses of the Sun and the Earth become $1 - \mu$ and μ, respectively. As the distance of a primary body with respect to the barycenter has an inverse relation to its mass, the dimensionless distance of the Sun and Earth with respect to the barycenter become μ and 1 - μ, respectively. Finally, the unit of time is set to $1/\omega$, with $\omega = 1$, such that one year becomes 2π in dimensionless time units.

In the synodic reference frame $C(x, y, z)$ the motion of the spacecraft is described by [8]

$$\ddot{\vec{r}} = \vec{a}_s - \nabla U - 2\vec{\omega} \times \dot{\vec{r}} \tag{2}$$

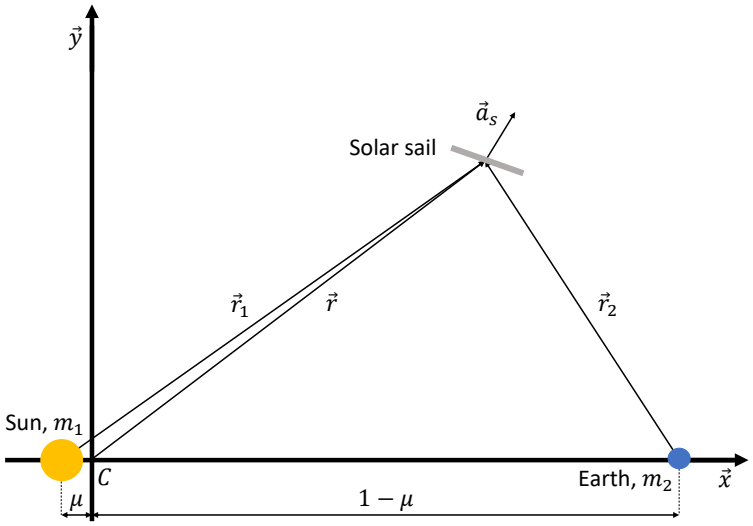

Fig. 1 Graphical overview of (a solar sail in) the Sun-Earth planar circular restricted three-body problem.

where $\vec{r} = [x \quad y \quad z]^T$, $\vec{a}_s$ is the solar-sail acceleration, and U is the effective potential, which is equal to [8]

$$U = -\frac{x^2 + y^2}{2} - \left(\frac{1-\mu}{r_1} + \frac{\mu}{r_2}\right) \tag{3}$$

where the position vectors from the Sun and the Earth to the spacecraft are denoted as $\vec{r}_1$ and $\vec{r}_2$, respectively, $r_1 = |\vec{r}_1|$, $r_2 = |\vec{r}_2|$, $\vec{r}_1 = [x+\mu \quad y \quad z]^T$, and $\vec{r}_2 = [x-(1-\mu) \quad y \quad z]^T$. As mentioned before, two-dimensional motion is considered, resulting in $z = 0$.

B. Solar-sail Model

In this study, for the definition of the solar-sail acceleration both an ideal and an optical solar-sail model are adopted. Both models assume that the sail is perfectly flat. However, while the ideal model assumes pure specular reflection of the incident photons, the optical sail model accounts for absorption, diffuse reflection, and thermal emission [8]. The ideal model is more insightful, while the optical solar-sail model is more realistic than an ideal model and therefore more relevant [8]. Therefore, at first, the ideal solar-sail model is used which is later replaced by the optical model in the sensitivity analysis (see Ch. V).

The solar-sail acceleration can be expressed in a term that is tangent to the solar sail, $a_t\hat{\vec{t}}$ and a component normal to the sail, $a_n\hat{\vec{n}}$ as

$$\vec{a}_s = a_s\hat{\vec{m}} = a_t\hat{\vec{t}} + a_n\hat{\vec{n}} \tag{4}$$

where $\hat{\vec{m}}$ is a unit vector in the direction of the total solar-sail acceleration. A graphical representation of the solar-sail acceleration components can be seen in Fig. 2. The solar-sail pitch angle, α, is defined as the angle between the incoming

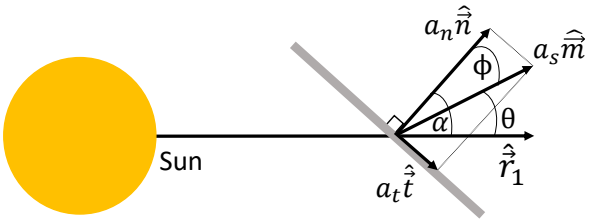

Fig. 2 Non-ideal solar-sail acceleration components adapted from Ref. [19].

photons ($\hat{\vec{r}}_1$) and the solar-sail normal direction ($\hat{\vec{n}}$). The solar-sail pitch angle will be limited to $\alpha \in [-70, 70]$ deg as within this range the optical solar-sail model is able to model real sail effects within 1-2% accuracy [20]. An auxiliary angle can be defined as

$$\phi = \arctan\left(\frac{a_t}{a_n}\right) \tag{5}$$

which results in

$$\theta = \alpha - \phi \tag{6}$$

The magnitude of the acceleration components tangent and normal to the solar sail, a_t and a_n, respectively, can be expressed as [8]

$$\begin{cases} a_n = \dfrac{1}{2}\beta\dfrac{1-\mu}{r_1^2}\left[(1+\tilde{r}s)\cos^2\alpha + B_f(1-s)\tilde{r}\cos\alpha + (1-\tilde{r})\dfrac{\varepsilon_f B_f - \varepsilon_b B_b}{\varepsilon_f + \varepsilon_b}\cos\alpha\right] \\ a_t = \dfrac{1}{2}\beta\dfrac{1-\mu}{r_1^2}(1-\tilde{r}s)\cos\alpha\sin\alpha \end{cases} \tag{7}$$

where β is the solar-sail lightness number, which is the defined as the ratio between the solar radiation pressure and the solar gravitational acceleration, $\tilde{r}$ is the reflectivity coefficient, s is the coefficient of specular reflection, B_f and B_b are the non-Lambertian coefficients of the front and back side of the solar sail, respectively, and ε_f and ε_b are the front and back side emissivity coefficients, respectively. Note that the dynamical model presented in Section II.A is given in the synodic reference frame $C(x, y, z)$, which means that the solar-sail acceleration should also be expressed in this frame. An explicit expression for the solar-sail orientation in the $C(x, y, z)$ frame is retrieved from Ref. [21][†]:

$$\begin{aligned} m_x &= \frac{x-\mu}{r_1}\cos\theta + \frac{y}{r_3}\sin\theta \\ m_y &= \frac{y}{r_1}\cos\theta - \frac{x-\mu}{r_3}\sin\theta \end{aligned} \tag{8}$$

where $r_3 = \sqrt{(x-\mu)^2 + y^2}$. Then, the solar-sail acceleration in frame $C(x, y, z)$ is defined as $\vec{a}_s = \begin{bmatrix} a_s m_x & a_s m_y \end{bmatrix}^T$.

[†]The clock angle, used to define the solar-sail orientation in three-dimensional space, is set equal to 90 deg in the two-dimensional formulation used in this paper.

In this study, a lightness number of $\beta = 0.05$ is considered initially, which is in accordance with expected near-term technological advances [22]. The effect of a change in the value of the lightness number on the performance of the solar-storm detection trajectories will be examined in Section V. The values and uncertainties of the coefficients for the ideal and optical solar-sail model are presented in Table 1 and are retrieved from NASA's NEA Scout mission [23]. Note that there is no uncertainty in the coefficient set of the ideal solar-sail model, because they are an implicit result of the assumptions of the model. In addition, when the coefficient set of the ideal solar-sail model is substituted in Eq. (7), only a solar-sail acceleration component normal to the sail remains ($a_t = 0$). Consequently, the direction of the total solar-sail acceleration is the same as the direction of the solar-sail normal acceleration ($\vec{m} = \vec{n}$ and therefore $\theta = \alpha$) and the solar-sail acceleration as in Eq. (7) reduces to [8]

$$\vec{a}_s = \beta \frac{1-\mu}{r_1^2} (\hat{\vec{r}}_1 \cdot \hat{\vec{n}})^2 \hat{\vec{n}} \tag{9}$$

Then, using Eq. (2), Eq. (8), and Eq. (9), the motion of the spacecraft as a function of the sail parameters (α, β) can be rewritten as [24]

$$\vec{\ddot{r}} = \begin{bmatrix} -\dfrac{\partial \tilde{U}}{\partial x} + 2\dot{y} + \beta \frac{1-\mu}{r_1^2} \frac{y}{r_3} \cos^2 \alpha \sin \alpha \\ -\dfrac{\partial \tilde{U}}{\partial y} - 2\dot{x} - \beta \frac{1-\mu}{r_1^2} \frac{x-\mu}{r_3} \cos^2 \alpha \sin \alpha \end{bmatrix} \tag{10}$$

where $\tilde{U} = -\frac{x^2+y^2}{2} - (1 - \beta \cos^3 \alpha) \frac{1-\mu}{r_1} - \frac{\mu}{r_2}$ and is referred to as the modified effective potential.

Table 1 The coefficient set and its uncertainty retrieved from Ref. [23] for both an ideal and optical solar-sail model.

	Coefficient	$\tilde{r}$, -	s, -	B_f, -	B_b, -	e_f, -	e_b, -
Ideal	Value	1.0	1.0	-	-	-	-
	Uncertainty	-	-	-	-	-	-
Optical	Value	0.91	0.94	0.79	0.67	0.025	0.27
	Uncertainty	0.005	0.04	0.05	0.05	0.005	0.005

C. Coronal Mass Ejection model

The CME-model that describes the propagation of a CME headed towards Earth is retrieved from Ref. [17] and is presented in Fig. 3. It takes into account all key evolutionary aspects and the magnetic field configuration. The key evolutionary aspects are deflection, rotation, expansion, pancaking, front flattening, and rotational skew. The first three aspects relate to the changes in orientation of a CME in interplanetary space, caused mostly by the solar wind. Pancaking is the effect of a latitudinal stretch caused by the radial propagation of a CME. Furthermore, front flattening

happens when a CME propagates much faster than the speed of the solar wind, which induces a drag force on the CME and thereby flattens the front part. Finally, rotational skew occurs due to the rotation of the Sun and can be modelled as a rotational deformation around the axis perpendicular to the line connecting the Sun and the Earth. These key evolutionary aspects can generally be expressed by a force balance as [17]

$$\vec{F}_H = \vec{F}_G + \vec{F}_B \tag{11}$$

where $\vec{F}$ denotes a force vector and the subscripts H, G, and B correspond to hydrodynamic streamlining, gravity, and magnetic tension, respectively. The numerical solution describing the axis of the CME (Fig. 12) to the force balance is defined in a polar reference frame $(P(l, \gamma))$ with the origin P at the center of the Sun, l is the radius, and γ is the angular coordinate which is defined to be positive in counterclockwise direction. The numerical solution is equal to [17]

$$l(\gamma) = R_t \cos^n(a\gamma) \tag{12}$$

where $R_t = 1 + \mu$ is the toroidal height of the CME, $n = 0.25$ is the coefficient of front flattening, and $a = \frac{\pi}{2\gamma_{hw}}$ where $\gamma_{hw} = 25$ deg is the angular half-width of the axis [17].

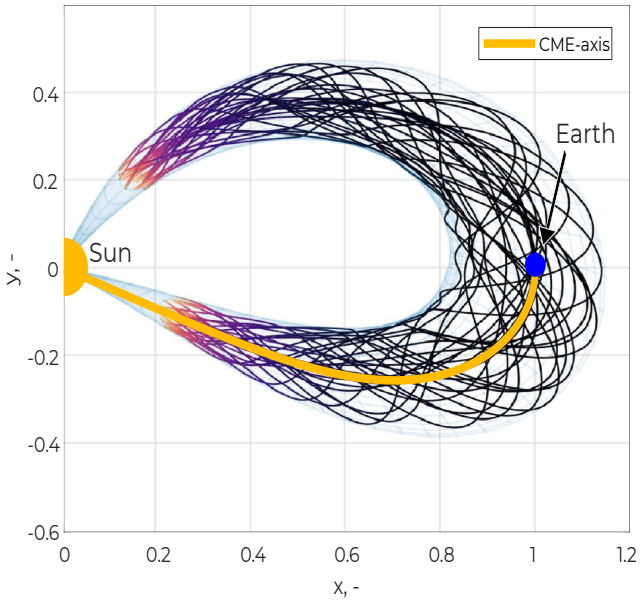

Fig. 3 Coronal Mass Ejection axis (CME-axis) with the CME-model from Ref. [17] projected onto the ecliptic plane in the synodic reference frame $C(x, y, z)$.

In this study, the CME-model is restricted to the ecliptic projection of the CME-axis and the CME boundary lines as an objective for the spacecraft to travel upstream of it. The inner and outer boundary lines are modelled with Eq. (12)

using $[R_t, n, \gamma_{hw}] = [0.815, 0.18, 15]$ and $[1.115, 0.20, 32]$, respectively [17]. As a result, the radial size of the CME is 0.33 AU, which is equal to mean radial size of all detected CMEs during solar cycle 23 (1996 - 2009) [25]. Note that only the "bottom part" (i.e., the fourth quadrant of the (x, y)-plane) of the CME is taken into consideration, as shown in Fig. 3. Because of the dynamics of the Sun and the Earth, incoming CMEs propagate in an anti-clockwise direction. As a result, upstream CME detection is restricted to the fourth quadrant of the (x, y)-plane. Furthermore, from the fourth quadrant the spacecraft is able to look at the surface of the Sun that is about to rotate towards the Earth, thereby allowing for earlier and better *predictions* of space weather events [26]. Although the CME *prediction* feature is not considered in this study, it is still worthwhile to recognise it for possible follow-up studies.

D. Equilibrium Points

An equilibrium point is defined as a location where, once an object is placed there with zero velocity, no net acceleration acts on the body, i.e., $\ddot{\vec{r}} = \dot{\vec{r}} = \vec{0}$. Substituting these conditions into Eq. (2) and assuming an ideal solar-sail model, the location of an equilibrium point can be found by

$$\nabla U = \vec{a}_s = \beta \frac{1-\mu}{r_1^2} (\hat{\vec{r}}_1 \cdot \hat{\vec{n}})^2 \hat{\vec{n}} \tag{13}$$

In the classical case ($\beta = 0$), solving Eq. (13) for the positional coordinates of the equilibrium points leads to the five well-known Lagrange points in the (x, y)-plane. Including a solar-sail acceleration into the dynamical model allows for surfaces of equilibria, which are referred to as AEPs. Equation (13) can only be satisfied if the operator ∇ is in the same direction as $\hat{\vec{n}}$, which imposes a constraint on the required solar-sail acceleration to realise an AEP, and has to be equal to $\hat{\vec{n}} = \nabla U / |\nabla U|$. Rewriting Eq. (13) leads to the required lightness number to maintain an AEP as

$$\beta = \frac{r_1^2}{1-\mu} \frac{\nabla U \cdot \hat{\vec{n}}}{\left(\hat{\vec{r}}_1 \cdot \hat{\vec{n}}\right)^2} \tag{14}$$

A constraint should be imposed on the solar-sail acceleration as it cannot point towards the Sun, which can be mathematically described as $\hat{\vec{r}}_1 \cdot \hat{\vec{n}} \geq 0$. The AEPs as a function of lightness number ($\beta \in [0, 0.1]$) in the vicinity of the Sun-Earth L_1, L_2, and L_5 point appear in Fig. 4. As can be seen, the surface of AEPs shifts sunwards for an increase in lightness number. The AEPs corresponding to a lightness number of $\beta = 0.05$ including the required solar-sail orientation can be seen in Fig. 5. Note that the AEP along the line between the Sun and the respective Lagrange point is referred to as a sub-Lagrange point. In Fig. 5, the SL_1 and SL_5 point are highlighted.

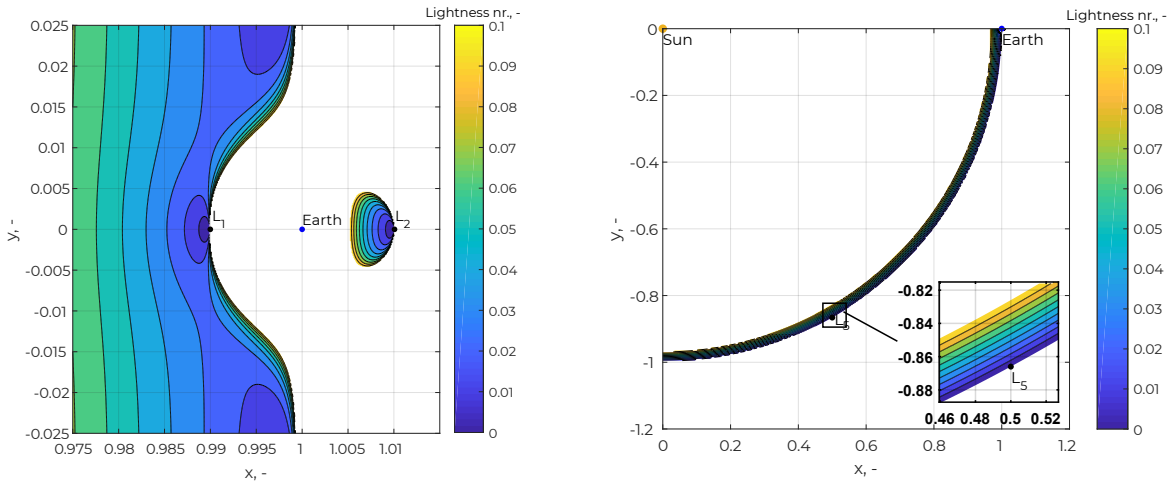

(a) The vicinity of the L_1 and the L_2 point. **(b) The vicinity of the L_5 point.**

Fig. 4 Surfaces of Artificial Equilibrium Points (AEPs) in the vicinity of the Sun-Earth L_1, L_2, and L_5 point as a function of lightness number ($\beta \in [0, 0.1]$).

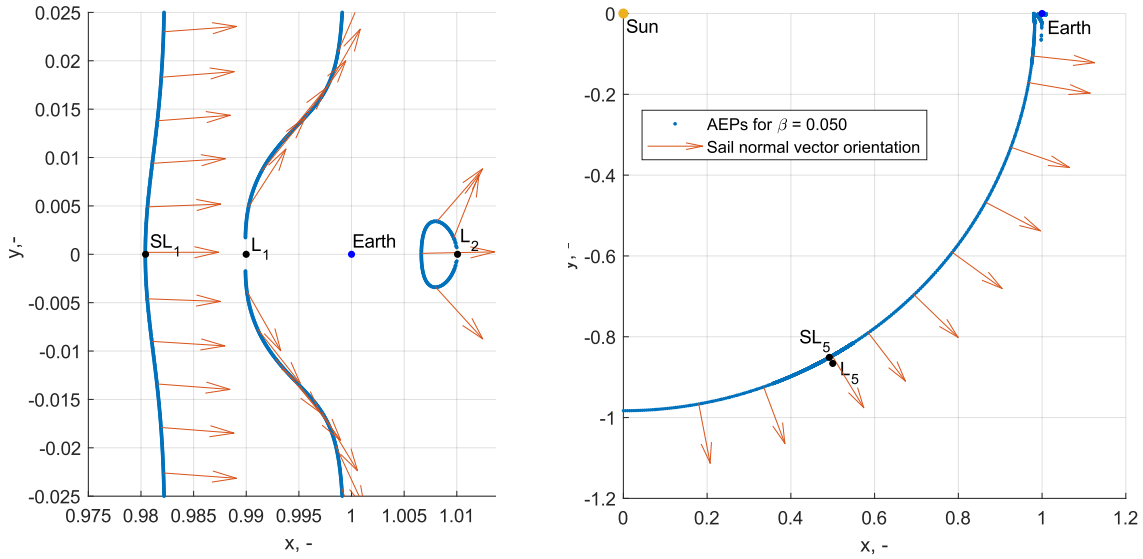

(a) The vicinity of the SL_1 point. **(b) The vicinity of the SL_5 point.**

Fig. 5 Artificial Equilibrium Points (AEPs) and the required solar-sail orientation for a lightness number of $\beta = 0.05$ in the vicinity of the SL_1 and SL_5 point.

E. Manifolds

To gain insight into any possible (natural) motion of a spacecraft with a solar sail at an equilibrium point, the stability of the equilibrium point should be assessed at first. The AEPs in the vicinity of the SL_1 and SL_5 point are classified into three categories according to their (linear) stability properties and can be seen in Fig. 6 [27].

The classes are defined as a function of the eigenvalues of the Jacobian, A, as [27]

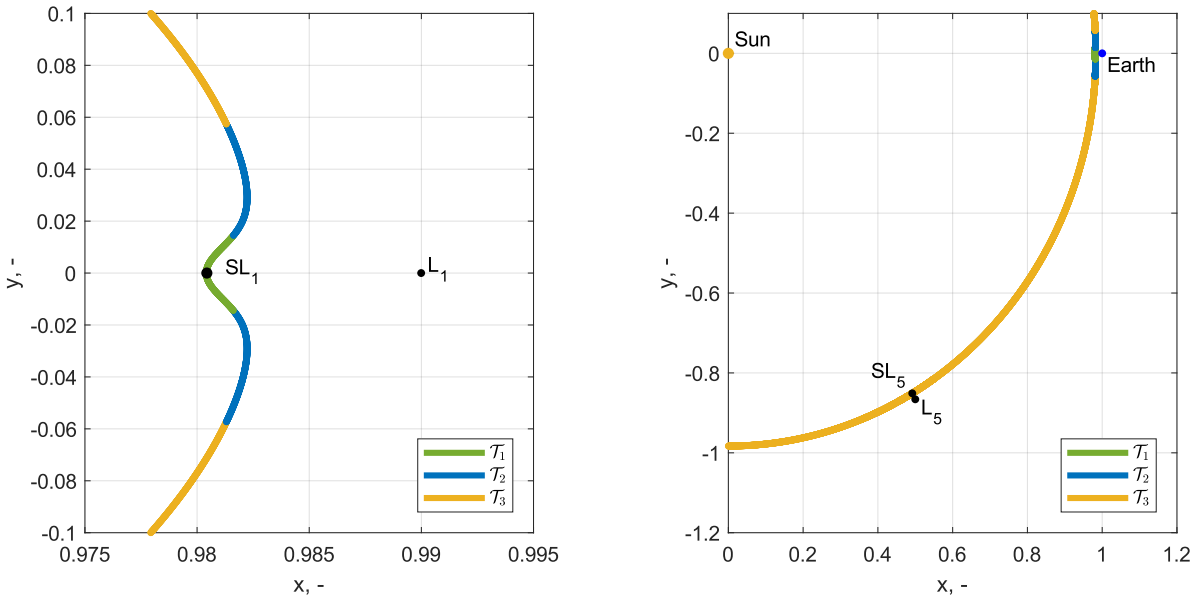

(a) The vicinity of the SL_1 point.

(b) The vicinity of the SL_5 point.

Fig. 6 Stability classes of the AEPs in the vicinity of the SL_1 and the SL_5 point [27].

- Class $\mathcal{T}_1$: AEPs with eigenvalues: $\lambda_1 = \tilde{\alpha}_1 > 0$, $\lambda_2 = \tilde{\alpha}_2 < 0$, $\lambda_{3,4} = \tilde{\alpha}_3 \pm \tilde{\beta}_3 i$ with $|\tilde{\alpha}_3| < |\tilde{\beta}_3|$. The AEPs in this class are unstable.
- Class $\mathcal{T}_2$: AEPs with all eigenvalues complex: $\lambda_{1-4} = \tilde{\alpha}_{1,2} \pm \tilde{\beta}_{1,2} i$ and $|\tilde{\alpha}_{1,2}| > 0.001$. The AEPs in this class show some instability due to a real part larger than 0.001.
- Class $\mathcal{T}_3$: AEPs with all eigenvalues complex: $\lambda_{1-4} = \tilde{\alpha}_{1,2} \pm \tilde{\beta}_{1,2} i$ and $|\tilde{\beta}_{1,2}| < 0.001$. The AEPs in this class are either stable ($\tilde{\alpha}_{1,2} = 0$) or almost stable ($|\tilde{\alpha}_{1,2}| \in [0.000, 0.001]$) as the time to leave the vicinity of the AEP is large.

Furthermore, the Jacobian is defined as [8]

$$A = \begin{bmatrix} 0 & I \\ \left.\frac{\partial \ddot{r}}{\partial \vec{r}}\right|_{\vec{r}_0} & 2\Omega \end{bmatrix}; \quad \Omega = \begin{bmatrix} 0 & 1 \\ -1 & 0 \end{bmatrix} \tag{15}$$

From Fig. 6 it can be seen that a small portion of the AEPs have unstable (linear) stability characteristics (class $\mathcal{T}_1$, $\mathcal{T}_2$). A result of this characteristic is that when the state undergoes a small linear perturbation, natural motion, i.e., manifolds, away from/towards the AEP occurs. Manifolds can be obtained by perturbing the state in the direction of the stable and unstable eigenvectors as

$$\vec{x} = \vec{x}_0 \pm \epsilon \vec{v} \tag{16}$$

where $\vec{x}$ is the state (position and velocity coordinates) of the spacecraft, $\vec{v}$ denotes the stable or unstable eigenvector of the Jacobian, the subscript 0 indicates the conditions at the considered AEP, and ϵ is a small linear perturbation (10^{-6}). Then, the unstable and stable manifolds are obtained by integrating the state $\vec{x}$ forwards and backwards in time, respectively.

It should be noted that a small fraction of the AEPs in Fig. 6 belong to classes $\mathcal{T}_1$ and $\mathcal{T}_2$, meaning that only a minority of AEPs have unstable and stable manifolds [27]. To generate equivalent manifold trajectories for AEPs from class $\mathcal{T}_3$, the solar sail may be pitched in an orientation that is different from what is required to maintain the respective AEP. It introduces a perturbing acceleration at the equilibrium point that is several orders larger than the linear perturbation ϵ [9]. Strictly speaking, the resulting manifold-like trajectories are not true manifolds because an active change in sail attitude is required to initiate the motion; the spacecraft does thus not naturally move away or towards the AEP. However, to ease the notation in this paper, these manifold-like trajectories will be referred to as manifolds from hereon.

The manifolds as a function of pitch angle for several AEPs in the vicinity of the SL_1 and SL_5 point can be seen in Fig. 7. From inspection, a trend in the manifolds can be derived. First, it can be seen that the induced perturbation due to the variation of the solar-sail orientation at the considered AEP is large enough such that unstable and stable manifold-like trajectories can be obtained from the AEPs that fall under class $\mathcal{T}_3$. In addition, for pitch angles $\alpha > 0$, the stable and unstable manifolds propagate in a counterclockwise manner about the Sun whereas the manifolds for $\alpha < 0$ propagate in a clockwise manner about the Sun. This insight will be used in subsequent chapters.

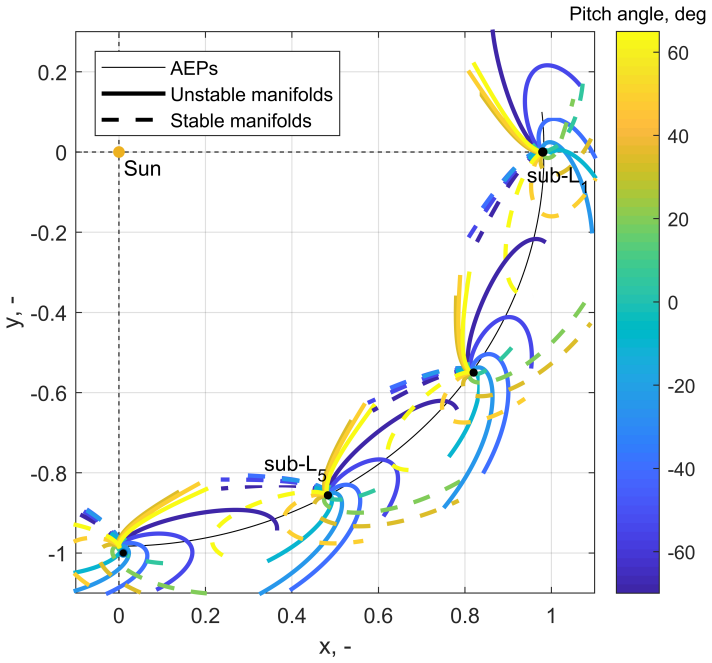

Fig. 7 Unstable and stable manifold trajectories as a function of the solar-sail pitch angle.

III. Initial Guess Trajectories

Now that the previous section laid out the building blocks to generate periodic solar-sail trajectories, the search for these trajectories can be initiated. It was determined in Section II.E that manifolds of AEPs (that fall under class $\mathcal{T}_3$ in Fig. 6) can be created by changing the solar-sail pitch angle to a value different from what is required to maintain the respective AEP. When an unstable and stable manifold from different AEPs match in four-dimensional position-velocity space, a heteroclinic connection between the AEPs is realised. This paper investigates whether such a connection can be utilised for solar-storm detection. In addition, to guarantee periodicity, a second heteroclinic connection is searched for that allows the spacecraft to travel back towards the AEP from which the first heteroclinic connection was initiated, such that this set of two heteroclinic connections creates a periodic trajectory. Note that this trajectory relies solely on the continuous solar-sail acceleration as its propulsion source. As a result, the lifetime of such a mission is only limited by the operational lifetime of the spacecraft equipped with the solar sail.

This section focuses on finding (almost-)feasible initial guess trajectories. These will be used for the optimisation of periodic solar-sail trajectories in $\mathcal{PSOPT}$, as described in the the introduction of this paper. At first, the problem definition and methodology regarding the search for an initial guess is presented, after which the initial guess generation itself is given. Note that the following assumptions are made:

1) An ideal solar-sail model is used.
2) A lightness number of $\beta = 0.05$ is taken, as discussed in Section II.B, which is in accordance with near-term technological advances [22].
3) A constant CME size is used equal to the mean size of all CMEs detected in solar cycle 23 (1996 - 2009) [25].
4) The (initial-guess) trajectory comprises two heteroclinic connections, that depart and arrive at an AEP in the vicinity of the Sun-Earth SL_1 and SL_5 points.
5) The solar-sail pitch angle is constant throughout each leg (manifold) of the trajectory (more information on this is given in Section III.A).

A. Methodology

The problem set-up and terminology is graphically presented in Fig. 8. The trajectory that will be travelling upstream of the CME-axis is composed of two heteroclinic connections between points p_1 and p_2, which are AEPs located in the vicinity of the SL_1 and the SL_5 points. The first connection allows the spacecraft to travel from p_1 to p_2 and the second connection from p_2 back to p_1. By this definition, the spacecraft is able to repeat the same trajectory. Each heteroclinic connection consists of an unstable manifold that allows the spacecraft to move away from the AEP at p_1, and a stable manifold that results in motion towards the AEP at p_2. In addition, each segment of the trajectory adopts a constant pitch angle (α_{1-4}). The state vector of unstable and stable manifolds should match each other in the four-dimensional position-velocity space at the Poincaré section $\sum = \{y = x \tan\tilde{\theta}\}$. This Poincaré section is a hyper-plane where $\tilde{\theta}$ is the

angle between the Sun-Earth line and the hyper-plane measured in the (x, y)-plane. The position and velocity error between the state vector of the stable and unstable manifold on the hyper-plane is denoted as Δr_i and Δv_i, where $i = 1, 2$ and indicates the first or second heteroclinic connection, respectively. Following Ref. [28], a connection is regarded feasible when the dimensionless position and velocity error satisfies $\Delta r_i \leq 10^{-3}$ and $\Delta v_i \leq 10^{-2}$ (i.e., 1.5x10^5 km and 0.30 km/s), respectively.

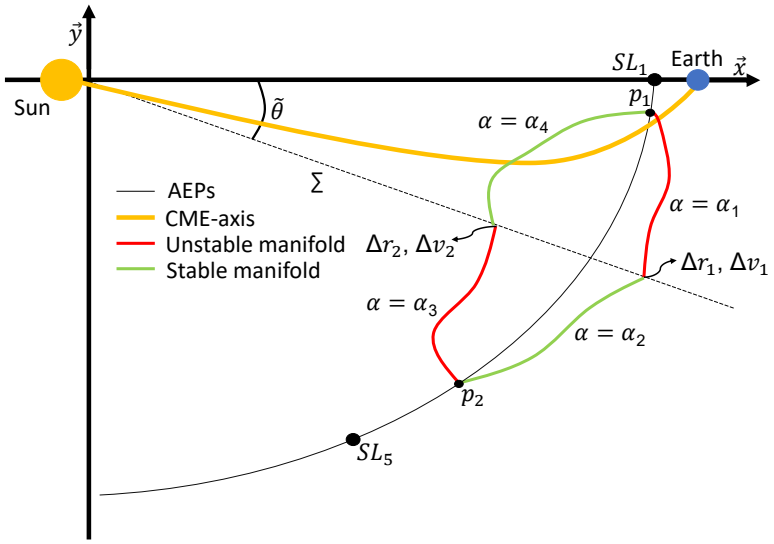

Fig. 8 Problem set-up and terminology of finding a heteroclinic connection between AEPs at p_1 and p_2.

Initial guess trajectories will be chosen based on the minimisation of two different objective functions. The first objective function, J_1, searches for a trajectory that travels furthest upstream of the CME-axis, i.e., maximises the *maximum* increase in warning time with respect to current missions at the Sun-Earth L_1 point, $k_{\max}$, and is mathematically defined as

$$J_1 = \frac{1}{k_{\max}} + q \cdot \left(\Delta r_1 + \Delta r_2 + \frac{\Delta v_1 + \Delta v_2}{10} \right) \tag{17}$$

Note that $k_{\max}$ is determined by the point on the trajectory that is located furthest upstream of the CME-axis. In Eq. (17), q is defined as

$$q = \begin{cases} 1 & \text{if} \quad \Delta r_{1,2} > 10^{-3} \quad \text{or} \quad \Delta v_{1,2} > 10^{-2} \\ 0 & \text{if} \quad \Delta r_{1,2} \leq 10^{-3} \quad \text{or} \quad \Delta v_{1,2} \leq 10^{-2} \end{cases} \tag{18}$$

which is put in place to add a penalty to the objective function when the trajectory is infeasible. In addition, the weights equal to one and $\frac{1}{10}$ in Eq. (17) are used to scale the state error by one order smaller ($O(10^{-3})$) than the magnitude of $\frac{1}{k_{\max}}$ (approximately $O(10^{-2})$) such that the performance of a trajectory is appropriately impacted if it is infeasible. The second objective function, J_2, aims for a trajectory that maximises the *average* increase in warning time with respect to

current missions at the Sun-Earth L_1 point, k_{avg}, and is mathematically defined as

$$J_2 = \frac{1}{\int_0^T \frac{k(t)}{T} dt} + q \cdot \left(\Delta r_1 + \Delta r_2 + \frac{\Delta v_1 + \Delta v_2}{10} \right) \tag{19}$$

where $k(t)$ is the increase in warning time along the trajectory, T is the period of the trajectory, and q is retrieved from Eq. 18. The weights equal to one and $\frac{1}{10}$ are chosen with the same rationale as in Eq. (17).

The determination of the increase in warning time with respect to current missions at the Sun-Earth L_1 point, k, at a particular point, p, is visualised in Fig. 9. If point p lies in the CME detection zone, i.e., in-between the CME boundary

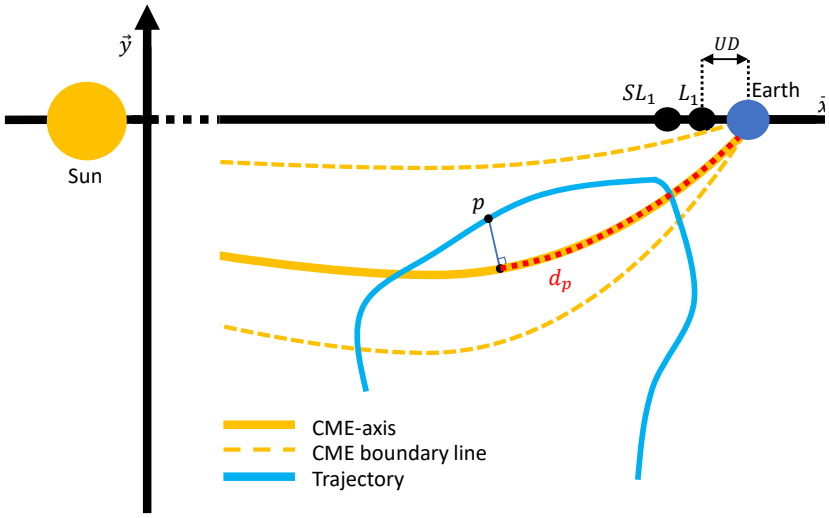

Fig. 9 Definition of the increase in warning time with respect to current missions that are at the Sun-Earth L_1 point.

lines, the increase in warning time is obtained by finding the perpendicular projection of p onto the CME-axis and dividing the arc length of the CME-axis from that point to the Earth, d_p, by the distance between the Earth and the L_1 point, UD, as

$$\begin{aligned} k &= \frac{d_p}{UD} \\ UD &= x_{\text{Earth}} - x_{L_1} \end{aligned} \tag{20}$$

UD is defined to be the distance between the Earth and the Sun-Earth L_1 point, where current CME detection missions are located [7]. With this definition, k_p is the increase in warning time factor with respect to current missions that are placed at or near the classical L_1 point.

B. Initial Guess Generation

A grid search is performed on various selected AEPs (presented in the next section) and the solar-sail pitch angles, α_{1-4}, to gain first-order insights into the dynamics of the problem and how they relate to the characteristics of the trajectories. After that, trajectories are sought for within the subset of feasible grid-search trajectories that minimise objective functions J_1 and J_2. Finally, a genetic algorithm (GA) will be used to find true initial guess trajectories. Note that some of the insights of the grid search will be used in the genetic algorithm to achieve a more effective search.

1. Grid search: minimum error in state

Heteroclinic connections are sought for between five selected AEPs where the starting AEP can be selected from $p_1 = [SL_1, P_3]$ and the arrival AEP can be selected from $p_2 = [P_1, SL_5, P_2, P_3]$. The points are graphically presented in Fig. 10 and an overview of the coordinates of these points is given in Table 2. In addition to SL_1 and SL_5, P_1 is selected as the point located at the boundary of the considered set of AEPs, P_2 is located halfway between SL_1 and SL_5, and P_3 is the AEP that crosses the CME-axis. Using this selection of p_1 and p_2, it is guaranteed that the resulting trajectory crosses the CME-axis at least once. Several variable hyper-plane simulations have been performed and it was concluded that a hyper-plane at the mid-distance between p_1 and p_2 contains sufficiently accurate trajectory results, which is also concluded in Ref. [29]. This model assumption will be taken into account, allowing for one fewer variable in the grid search (namely, $\tilde{\theta}$). The grid search consists of every combination of $p_1, p_2,$, α_{1-4} where $\alpha_{1,4} = [-70 : 0.25 : 0]$ degrees, and $\alpha_{2,3} = [0 : 0.25 : 70]$ degrees. The minimum and maximum solar-sail pitch angle value of ±70 degrees is in accordance with Section II.B [20]. Furthermore, the rationale behind the decision to only consider negative and positive values for $\alpha_{1,4}$ and $\alpha_{2,3}$, respectively, is outlined in Section II.E.

Table 2 Position coordinates of the five AEPs that are selected as p_1 and p_2 for the grid search.

	P_1	SL_5	P_2	P_3	SL_1
x-coordinate, -	0.000	0.483	0.849	0.978	0.980
y-coordinate, -	-0.983	-0.856	-0.496	-0.100	0.000

For each combination of the grid search, the following steps are performed to obtain a (periodic solar-sail) trajectory:

1) Forward propagate the unstable manifold at p_1 using $\alpha = \alpha_1$ until the hyper-plane $\sum$ is crossed.
2) Backward propagate the stable manifold at p_2 using $\alpha = \alpha_2$ until the hyper-plane $\sum$ is crossed.
3) Forward propagate the unstable manifold at p_2 using $\alpha = \alpha_3$ until the hyper-plane $\sum$ is crossed.
4) Backward propagate the stable manifold at p_1 using $\alpha = \alpha_4$ until the hyper-plane $\sum$ is crossed.
5) Evaluate the norm difference between the unstable and stable manifold state vector at the hyper-plane crossing, i.e., at the linkage, (Δr_i and Δv_i for $i = 1, 2$), where $\Delta r_i \leq 10^{-3}, \Delta v_i \leq 10^{-2}$ (i.e., 1.5x10^5 km and 0.30 km/s) is regarded as a feasible trajectory.

6) Determine the maximum increase in warning time ($k_{\max}$), the average increase in warning time (k_{avg}), the period (T), the fraction of time spent in the CME detection zone (t/T), and the number of required spacecraft to maintain continuous CME monitoring (n_{sc}), i.e., to ensure that there will always be a spacecraft in the CME detection zone.

For each combination of p_1 and p_2 the trajectories that have the smallest error in the state at the linkage, $\Delta(r+v)_{\min}$, are displayed in Fig. 10. Note that the objective in these grid-search results is to minimise the state error at the hyper-plane, rather than objective functions J_1 or J_2 (which will be used in subsequent sections). A summary of the properties of the trajectories is given in Table 3.

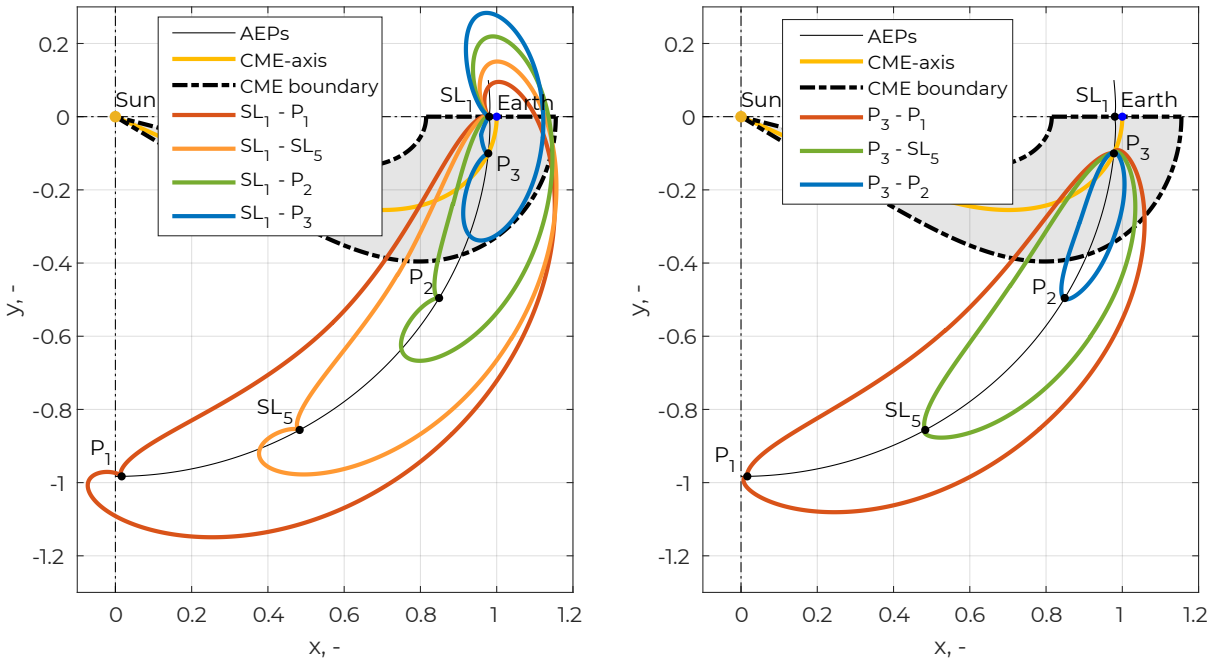

(a) $p_1 = SL_1$ **and** $p_2 = [P_1, SL_5, P_2, P_3]$**.** **(b)** $p_1 = P_3$ **and** $p_2 = [P_1, SL_5, P_2]$**.**

Fig. 10 Grid search: trajectories with minimal state error. The CME-model and the CME-axis are given for reference.

A general trend regarding the location where the trajectory crosses the CME-axis can be retrieved from Fig. 10. When p_1 tends towards SL_1 and p_2 towards P_1, the CME-axis is crossed furthest upstream, i.e., the maximum increase in warning time is maximised. This is confirmed by looking at Table 3 displaying a maximum increase in warning time of a factor 43.13 for the trajectory connecting $SL_1 - P_1$. In addition, it can be seen that when p_1 and p_2 tend towards P_3 the average increase in warning time is maximised. This is illustrated by the trajectory connecting $P_3 - P_2$ enabling an average increase in warning time of a factor 9.53, which is a maximisation of this parameter compared to the other trajectories. From these observations it can be concluded that the objective functions J_1 and J_2 oppose each other when

Table 3 Grid search: solar-sail orientation and trajectory properties. These trajectories have a minimum error in the state at the linkage ($\Delta(r+v)_{\text{min}}$).

$p_1 - p_2$	α_1, deg	α_2, deg	α_3, deg	α_4, deg	T, yr	t/T, -	n_{sc}, -	k_{max}, -	k_{avg}, -
$SL_1 - P_1$	-42.00	44.75	21.00	-19.25	3.8062	0.1390	8	43.13	2.19
$SL_1 - SL_5$	-49.00	50.50	12.75	-11.25	3.8221	0.1572	7	39.36	2.50
$SL_1 - P_2$	-55.25	56.25	6.25	-4.50	3.8218	0.2407	5	33.50	3.68
$SL_1 - P_3$	-60.00	60.75	2.75	-0.25	3.6948	0.6563	2	26.56	6.91
$P_3 - P_1$	-15.25	15.50	51.00	-51.50	3.3774	0.3283	4	42.76	4.98
$P_3 - SL_5$	-9.50	9.75	65.25	-65.75	3.1282	0.3821	3	40.13	5.92
$P_3 - P_2$	-4.00	4.25	4.50	-4.25	3.7990	0.5739	2	32.85	9.53

selecting p_1 and p_2, making it interesting to consider them separately and select a different initial guess trajectory for each.

The solar-sail pitch angle of the trajectories in Table 3 shows a correlation in the form of $\alpha_2 = -\alpha_1 \pm 2.75$ deg and $\alpha_4 = -\alpha_2 \pm 2.50$ deg. However, these trajectories are optimised to minimise the state error. A possible correlation between the pitch angle for all *feasible* trajectories, i.e., trajectories where $\Delta r \leq 10^{-3}, \Delta v \leq 10^{-2}$, is obtained by looking at Fig. 11. This figure maps the correlation in solar-sail pitch angle of all *feasible* trajectories from the grid search. Looking at Fig. 11b, it can be seen that all feasible combinations of α_3 and α_4 have a correlation in the form of

$$\alpha_4 = -\alpha_3 \pm 5.5 \text{ deg} \tag{21}$$

This correlation can be employed in the genetic algorithm to restrict the search space, resulting in a more effective search. A similar correlation can be found for the majority of trajectories from p_1 to p_2, as can be seen in Fig. 11a. However, there are some trajectories that do not follow this trend. In order to ensure that the search space is not too restricted, a correlation between α_1 and α_2 will not be employed in the genetic algorithm.

From Table 3 it can be seen that the period of all trajectories is approximately the same with a value of approximately 3.5 years, whereas the fraction of time spent in the CME detection zone (t/T) varies significantly for the trajectories, from approximately 0.13 to 0.57. This fraction determines the number of spacecraft required to achieve continuous CME monitoring. In general, it is seen that when p_1 tends towards P_3, the fraction of time spent in the CME detection zone is maximised as this point lies within it that zone. As a result, trajectories with a larger *average* increase in warning time spend more time in the CME propagation zone (larger t/T) than trajectories with a larger *maximum* increase in warning time. It is therefore expected that, in order to find a trajectory that maximises the *maximum* increase in warning time, i.e., minimisation of J_1, a constellation of multiple spacecraft is required to maintain continuous CME monitoring. On the other hand, it is expected that a trajectory that maximises the *average* increase in warning time, i.e., minimisation of J_2, requires only one spacecraft to achieve continuous CME monitoring.

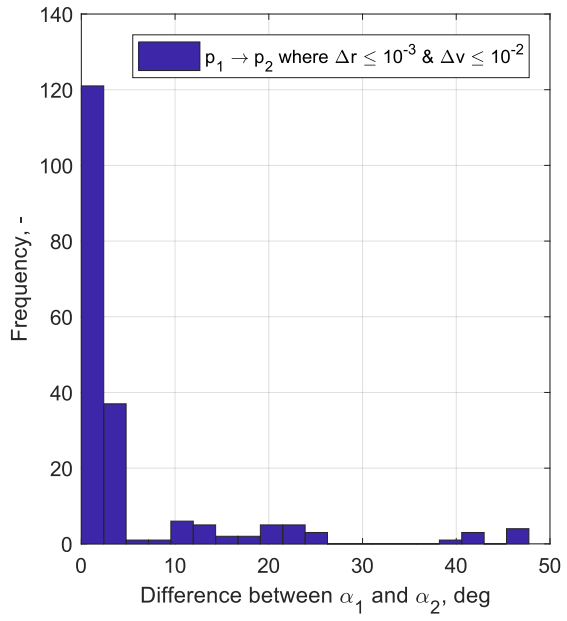

(a) First leg of the trajectory ($p_1 \rightarrow p_2$).

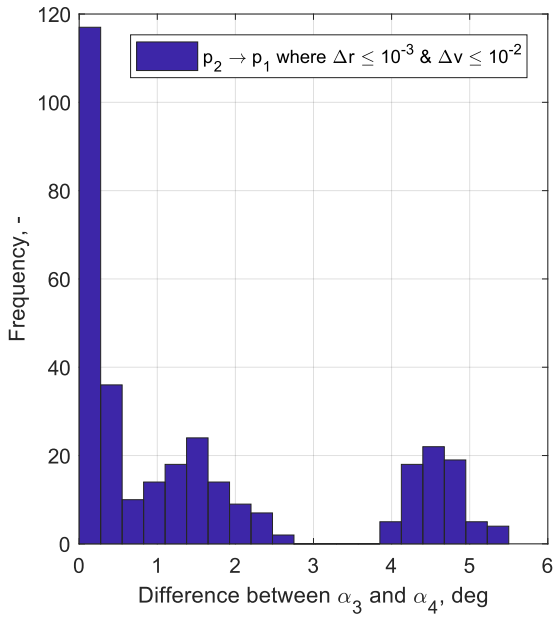

(b) Second leg of the trajectory ($p_2 \rightarrow p_1$).

Fig. 11 Grid search: histogram of the difference in solar-sail pitch angle at the linkage for all feasible trajectories.

2. Grid search: minimum in objective function

Within the subset of feasible grid-search trajectories (i.e., trajectories where $\Delta r_i \leq 10^{-3}$ and $\Delta v_i \leq 10^{-2}$), it is interesting to look for the trajectories that minimise J_1 and J_2. These trajectories are presented in Fig. 12 and Fig. 13, respectively, and an overview of the properties appear in Table. 4 and Table. 5, respectively. Note that the grid-search trajectories that minimise the state error have been given for reference. Furthermore, the trajectories that resulted from the GA will be explained in the next section. Finally, regarding the minimisation of J_2, both trajectories for $[p_1, p_2] = [SL_1, P_3]$ and $[P_3, P_2]$ have been given such that a more comprehensible comparison can be made.

The minimisation of J_1 results in a trajectory that connects SL_1 and P_1, which is in accordance with the expectation that was laid out in the previous section, and achieves a maximum increase in warning time of a factor 44.86. Note that the first part of the trajectory, the heteroclinic connection from p_1 to p_2, is the same for the grid search with the two different objectives ($\Delta(r+v)_{\text{min}}$ and $J_{1,\text{min}}$). The similarity can be explained by the fact that the objective J_1 only plays a role in the second part of the trajectory; the part where the maximum increase in warning time is actually achieved. Therefore, the sole purpose of the first part of the trajectory is to minimise the state error.

The trajectory that minimises J_2 achieves an average increase in warning time of a factor 10.35 and is obtained with $[p_1, p_2] = [P_3, P_2]$. It is however expected that this average increase in warning time can be further maximised by designing a trajectory that is fully spent within the CME propagation zone, which will be done in the next section. Note

that the trajectories are identical for $\Delta(r+v)_{\min}$ and $J_{2,\min}$ for $[p_1, p_2] = [SL_1, P_3]$. This is because of the method that the trajectory for $J_{2,\min}$ is selected: the algorithm evaluates J_2 for the feasible trajectories between SL_1 and P_3, but if there are no feasible trajectories between SL_1 and P_3, it selects the trajectory for $\Delta(r+v)_{\min}$ to minimise the state error. As the grid search did not give any feasible trajectories for this set of $[p_1, p_2]$, the trajectories are identical. Secondly, in general, the period of the trajectories for $J_{2,\min}$ is larger compared to the trajectories for $\Delta(r+v)_{\min}$, which can be attributed to the fact that the pitch angles for the trajectories of $J_{2,\min}$ are smaller than the trajectories of $\Delta(r+v)_{\min}$. As a result, a smaller perturbation acceleration acts on the equilibrium state at the AEP, therefore requiring more time to move away from/towards the AEP.

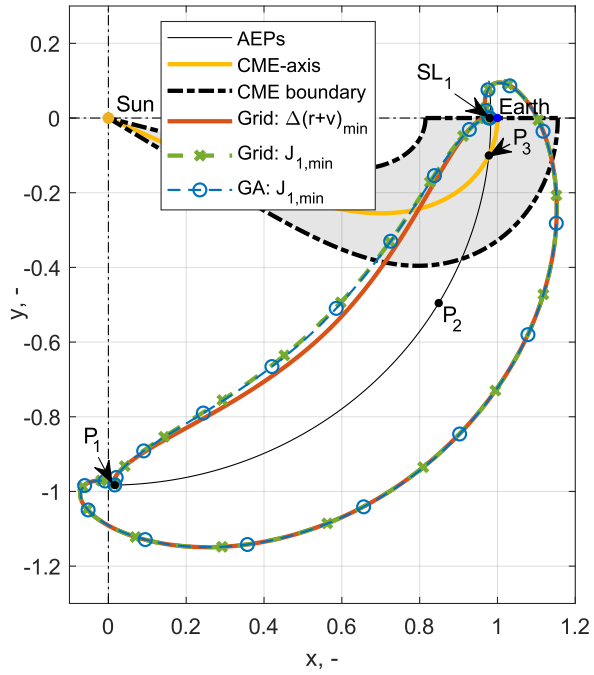

Fig. 12 Genetic algorithm and grid search: trajectories that maximise the maximum increase in warning time obtained with the grid search (green), the genetic algorithm (blue), and the trajectory that minimises the state error obtained with the grid search (red). The CME-model and the CME-axis are given for reference.

Table 4 Genetic algorithm and grid search: properties of the trajectories that minimise J_1 (Eq. (17)) and the grid-search trajectory that minimises the state error.

$p_1 - p_2$	Method	α_1, deg	α_2, deg	α_3, deg	α_4, deg	$\tilde{\theta}$, deg	T, yr	t/T, -	n_{sc}, -	k_{max}, -	k_{avg}, -
$SL_1 - P_1$	Grid: $\Delta(r+v)_{\min}$	-42.00	44.75	21.00	-19.25	-44.52	3.8062	0.1390	8	43.13	2.19
	Grid: $J_{1,\min}$	-42.00	44.75	43.75	-49.25	-44.52	3.4936	0.1436	7	44.86	2.13
$p_1 \in [P_3, SL_1]$ $p_2 \in [P1, P3]$	GA: $J_{1,\min}$	-39.04	43.31	44.91	-49.45	-44.52	3.4454	0.1513	7	44.86	2.19

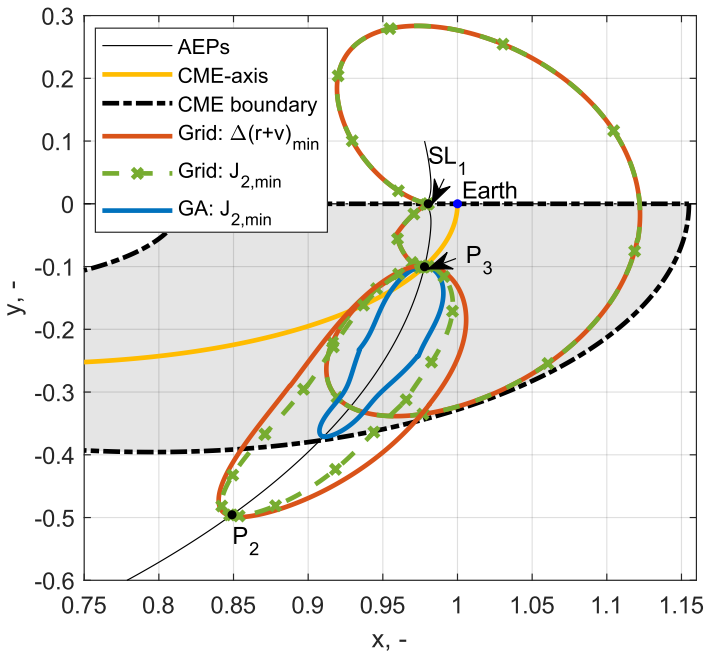

Fig. 13 Genetic algorithm and grid search: trajectories that maximise the average increase in warning time obtained with the grid search (green), the genetic algorithm (blue), and the trajectory that minimises the state error obtained with the grid search (red). The CME-model and the CME-axis are given for reference.

Table 5 Genetic algorithm and grid search: properties of the trajectories that minimise J_2 (Eq. (19)) and the grid-search trajectory that minimises the state error.

$p_1 - p_2$	Method	α_1, deg	α_2, deg	α_3, deg	α_4, deg	$\tilde{\theta}$, deg	T, yr	t/T, -	n_{sc}, -	k_{max} -	k_{avg}, -
$SL_1 - P_3$	Grid: $\Delta(r+v)_{min}$	-60.00	60.75	2.75	-0.25	-2.93	3.6948	0.6563	2	26.56	6.91
	Grid: $J_{2,min}$	-60.00	60.75	2.75	-0.25	-2.93	3.6948	0.6563	2	26.56	6.91
$P_3 - P_2$	Grid: $\Delta(r+v)_{min}$	-4.00	4.25	6.00	-5.75	-18.07	3.5792	0.5679	2	33.42	9.53
	Grid: $J_{2,min}$	-2.50	2.50	3.50	-3.25	-18.07	4.6243	0.5922	2	32.32	10.35
$p_1 \in [P_3, SL_1]$ $p_2 \in [P2, P3]$	GA: $J_{2,min}$	-1.50	1.00	1.02	-1.51	-14.00	5.8043	1.000	1	29.05	21.27

3. Genetic algorithm search

The grid search was limited to a small set of AEPs for p_1 and p_2 which, although convenient to gain first-order insight into the problem characteristics, restricts the search space too much. Consequently, the results obtained in the grid search cannot be regarded as the final results in the search for initial guesses, i.e., the trajectories that minimise J_1 and J_2 from Eq. (17) and Eq. (19), respectively. A genetic algorithm is employed to find these two initial guesses with

the following bounds on the decision variables

$$\begin{bmatrix} -70 \\ 0 \\ 0 \\ -1 \\ P_3 \\ P_1 \end{bmatrix} \leq \begin{bmatrix} \alpha_1 \\ \alpha_2 \\ \alpha_3 \\ M_1 \\ p_1 \\ p_2 \end{bmatrix} \leq \begin{bmatrix} 0 \\ 70 \\ 70 \\ 1 \\ SL_1 \\ P_3 \end{bmatrix} \tag{22}$$

where

$$\begin{aligned} \alpha_4 &= -\alpha_3 + 5.5M_1 \\ -70 &\leq \alpha_4 \leq 0 \end{aligned} \tag{23}$$

Note that the pitch angle correlation between α_3 and α_4 that is presented in Fig. 11b has been applied to restrict the search space by means of a decision variable $M_1 \in [-1, 1]$ that correlates α_4 to α_3 as can be seen in Eq. (23). Furthermore, p_1 and p_2 are a discretised set of AEPs between the specified bounds with a (distance) mesh of 0.001. In addition, the hyper-plane angle, $\tilde{\theta}$, is set to the mid-distance of p_1 and p_2, as was specified before [29]. Note that the trajectory is computed using the first four steps of the methodology outlined in the previous section. After that, the objective function J_1 or J_2 is evaluated. The *MATLAB* function *ga.m* is employed with the population size and the maximum number of generations set to 150 and 50, respectively. These values are obtained by trial and error as it was observed that these are sufficient values to allow for convergence. The GA is run for seeds [0,1,2,3,4] for both objective functions, and the results and a discussion of the results is provided below.

Initial guess: maximisation of the maximum increase in warning time

The trajectories that resulted from the GA that minimise J_1 can be seen in Fig. 12 and an overview of the trajectory properties appear in Table 4. Note that the trajectories that resulted from the grid search that minimised the state error and J_1 are also given.

The optimal trajectory found by the GA connects SL_1 and P_1, i.e.., $[p_1, p_2] = [SL_1, P_1]$, and achieves a maximum increase in warning time of a factor 44.86. This is in accordance with the trajectory obtained with the grid search for $J_{1,\text{min}}$, see Fig. 12. From this it can be concluded that, although the GA is a more robust method to determine an initial guess trajectory, the grid search method matches the result from the GA, while being a far more CPU efficient method. However, note that insight into the selection of p_1 and p_2 is required for the grid search method.

The minor differences between the trajectory from the GA and the trajectory from the grid search can be attributed to the fact that the grid search is limited to a discrete search space for all solar-sail pitch angles with a step size of 0.25 deg, whereas the GA is able to evaluate these angles on a continuous spectrum. The number of spacecraft required to maintain continuous CME monitoring is seven, which is also in accordance with the grid search results. All in all, it can be concluded that the grid search is able to find sufficiently accurate trajectories. However, as the trajectory that was found by the GA has a slightly larger average increase in warning time compared to the trajectory that was found in the grid search (2.19 over 2.13), the GA trajectory will be selected as the first initial guess for the optimal control problem.

Initial guess: maximisation of the average increase in warning time

The GA is run with the objective to minimise J_2 as displayed in Eq. (19). The results can be seen in Fig. 13 and an overview of the properties of the trajectories can be seen in Table 5.

It is seen that the trajectory found by the GA, as expected, lies completely in the CME propagation zone where $p_1 = P_3$ and $[x_{p_2}, y_{p_2}] = [0.910, -0.371]$, thereby requiring one spacecraft to guarantee continuous CME monitoring. This is in accordance with the hypothesis that was laid out in the grid search in the previous section. In addition, the optimal location of p_1 is P_3 due to the fact that this point is located furthest upstream of the CME-axis compared to the set of AEPs that is considered for p_1. Consequently, p_2 equals the AEP that allows the spacecraft to travel furthest upstream of the CME-axis, while still allowing for a trajectory that lies completely in the CME propagation zone. This trajectory has an average increase in warning time of a factor 21.27, which is a significant improvement of approximately a factor two compared to the results found by the grid search. All in all, this trajectory will be selected as the second initial guess for the optimal control problem.

4. Initial guess overview

The first initial guess aims to maximise the maximum increase in warning time and will from hereon be referred to as trajectory N_1. The second initial guess maximises the average increase in warning time and will be referred to as trajectory N_2. These trajectories, as well as the increase in warning time as a function of time, can be seen in Fig. 14. Seven spacecraft equally spaced in time that follow trajectory N_1 are required to always have one spacecraft in the CME detection zone. The increase in warning time for such a constellation is indicated by the dotted line in Fig. 14b.

IV. Optimal Control Problem

The trajectories displayed in the previous section give a good indication into the capabilities of solar sailing for solar-storm detection. However, these trajectories are practically infeasible as there are discontinuities in the solar-sail pitch angle profile as well as minor discontinuities in the state at the Poincaré section. In addition, these trajectories are sub-optimal as the solar-sail pitch angle remains constant throughout the unstable and stable manifolds of the trajectory.

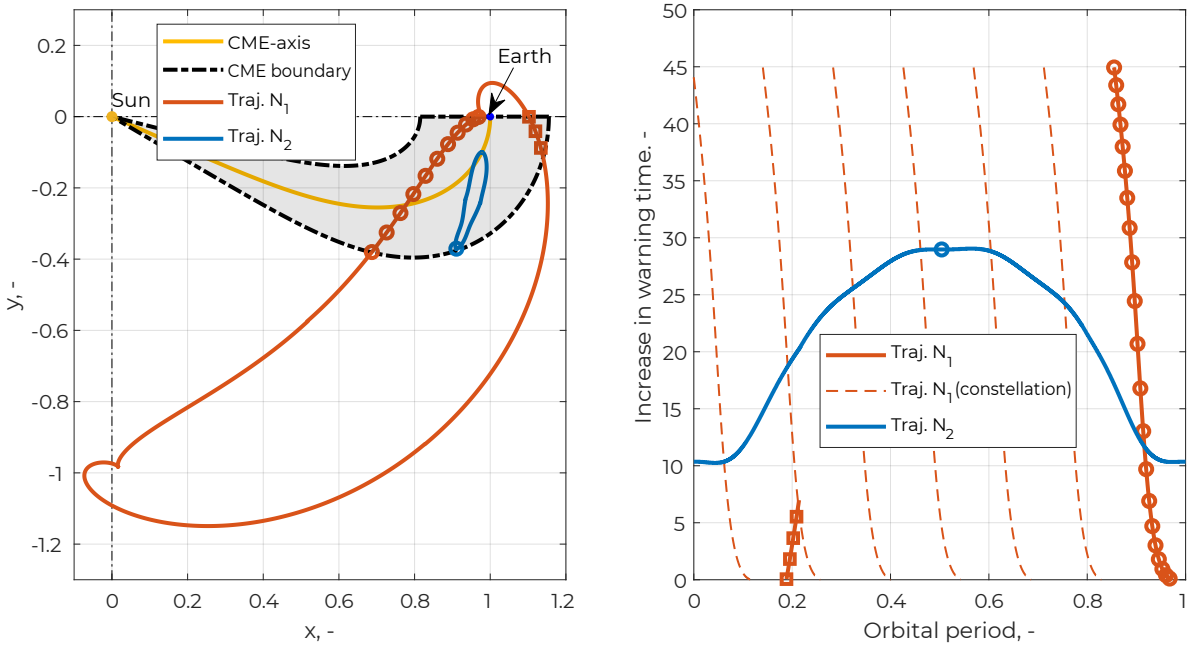

(a) The CME-model and CME-axis have been given for reference.

(b) Increase in warning time as a function of the orbital period of the trajectories.

Fig. 14 Overview of the trajectories that are selected as an initial guess for the optimisation with $\mathcal{PSOPT}$. Trajectory N_1 maximises the maximum increase in warning time and trajectory N_2 maximises the average increase in warning time. The round and square markers are given to correlate the two subfigures.

Finally, the trajectories have been optimised for one sole purpose; maximising either the average of maximum increase in warning time. It is interesting to take multiple factors, e.g., a combination of both, into account during the design of such a trajectory. An optimal control problem can be defined which takes away all of these limitations.

A direct pseudospectral method, in particular the C++ open-source implementation $\mathcal{PSOPT}$, will be used to solve the optimal control problem [18]. This method discretises the continuous time interval into a finite number of collocation points (Legendre-Gauss-Lobatto (LGL) nodes) and uses Legendre polynomials to approximate the state profile. The optimal control problem, that will be further elaborated upon in the following sections, contains the following problem characteristics: a single-phase problem with continuous time nonlinear dynamics, bounds on the state and control variables, a path constraint on the state variables, a combination of an integral and endpoint cost function, a free final time, and boundary constraints. $\mathcal{PSOPT}$ is able to deal with these characteristics [18].

Note that the first three assumptions outlined in Section III ($\beta = 0.05$, the use of an ideal solar-sail model, and a constant CME size) still apply here, whereas the last two assumptions (the trajectory comprises two heteroclinic connections and a constant solar-sail pitch angle throughout each leg of the trajectory) are no longer applicable. In addition, an assumption is added specifying that there is no constraint on the rate of change of the solar-sail pitch angle.

A. Methodology

In general, an optimal control problem can be defined as finding the state history $\vec{x}(t) = \mathbb{R}^{n_x}$ and the control history $\vec{u}(t) = \mathbb{R}^{n_u}$ where $t \in [t_0, t_f]$ that minimises a particular cost function J. For the problem at hand, J is defined as

$$\begin{aligned} J &= -w_1 \cdot k_{\text{avg}} + w_2 \cdot d_{\text{avg}} - w_3 \cdot k_{\max} \\ &= -w_1 \sum_{p=2}^{N} k_{\text{p}} \frac{(t_p - t_{p-1})}{t_N} + w_2 \sum_{p=2}^{N} ||\vec{r}_p - \vec{r}_{\text{CME,nearest}}|| \frac{(t_p - t_{p-1})}{t_N} - w_3 \cdot \max(k_{\text{p}}) \end{aligned} \tag{24}$$

where w_1, w_2, and w_3 are weights that can be varied to indicate relative importance, p is the considered collocation node, N is the total number of LGL nodes, and the subscript "CME,nearest" denotes the closest point on the CME-axis to the positional state of p. Recall that k_p is determined using the strategy that is outlined in Fig. 9. From Eq. (24) it can be seen that J consists of three components: the first term aims at maximising the *average* increase in warning time, the second term aims to minimise the *average* distance to the CME-axis (defined in Fig. 3), and the third term aims to maximise the *maximum* increase in warning time. The first and the third term were already used in the initial guess generation and the second term is added here. The average distance to the CME-axis is introduced as it increases the *probability* of detection. As the shape of the CME from the model laid out in Section II.C is based on an average of all detected CMEs in solar cycle 23 (1996 - 2009) [25], a trajectory that lies completely within the depicted CME boundary lines does not guarantee detection of all CMEs heading towards Earth. Consequently, while assuming that the CME-axis remains constant for all CMEs heading towards Earth, moving closer to the CME-axis increases the probability of detection. A quantitative analysis on this probability will be performed in Section V.C. Note that the cost function is scaled in time (the term $\frac{t_p - t_{p-1}}{t_N}$) as the LGL nodes are not equally spaced in time [18].

The state history is composed of the position and velocity state of the spacecraft in the Sun-Earth synodic reference frame, $C(x, y, z)$, as

$$\vec{x}(t) = [x(t) \quad y(t) \quad v_x(t) \quad v_y(t)]^T \tag{25}$$

having the following bounds

$$[0 \quad -1 \quad -0.5 \quad -0.5]^T \leq \vec{x}(t) \leq [1.15 \quad 0 \quad 0.5 \quad 0.5]^T \tag{26}$$

These bounds have been set such that the spacecraft is able to move in the fourth quadrant of the (x, y)-plane, as was illustrated in Section II.C. The control history is the solar-sail pitch angle profile

$$u(t) = \alpha(t) \tag{27}$$

limited between the bounds (as determined in Section II.B).

$$-70 \text{ deg} \leq u(t) \leq 70 \text{ deg} \tag{28}$$

The bounds on the time are set as

$$t_0 = 0, \qquad 10 \leq t_f \leq 50 \tag{29}$$

which corresponds to 1.59y $\leq t_f \leq$ 7.96y in dimensional time units. The values have been chosen based on the period of the initial guess trajectories which are in the order of 3.5 years.

To guarantee periodicity, the state and control at the initial and final time are set equal to each other as

$$\vec{x}(t_0) = \vec{x}(t_f) \qquad \vec{u}(t_0) = \vec{u}(t_f) \tag{30}$$

Note that the evaluation of the cost function in Eq. (24) starts at $p = 2$, because $p = 1$ and $p = N$ are effectively the same as a result of the requirement that the initial and final state have to be equal to each other (such that periodicity is guaranteed). Furthermore, note that there is no constraint on the *value* of the initial and final state and control, i.e., the trajectory does not have to depart/end at an AEP as opposed to the initial guess problem definition. The relaxation of this implicit constraint may lead to a "more optimal" trajectory as the search space is enlarged.

A path constraint is imposed on the problem to ensure that the spacecraft always remains within the CME zone. It is defined as

$$y_{\text{CME,boundary,L}}(x_p) \leq y_p \leq y_{\text{CME,boundary,U}}(x_p) \tag{31}$$

where $y_{\text{CME,boundary,L}}(x_p)$ and $y_{\text{CME,boundary,U}}(x_p)$ are the lower and upper y-coordinate of the CME boundary, respectively, and are modelled as an eighth order polynomial. As a result of this constraint, the required number of spacecraft to maintain a constellation of continuous CME monitoring is one. This constraint is implemented to be able to properly compare the performance of the different optimised solutions (due to various relative weight specifications in Eq. 24) as a discrepancy in the required number of spacecraft yields the comparison inconsistent and unusable.

$\mathcal{PSOPT}$ ensures that *only* at the nodes of the solution the state and control abides to the dynamics, the imposed constraints, and the bounds. To check whether the entire trajectory adheres to them, re-integration will be done in *MATLAB*. Two types of re-integration are executed: full re-integration and node-to-node re-integration. Full re-integration takes the initial conditions from $\mathcal{PSOPT}$ and integrates the state until the final time. The control, i.e., the solar-sail pitch angle, is interpolated from the $\mathcal{PSOPT}$ solution using shape-preserving piecewise cubic interpolation [30]. The difference in state at $t = t_f$ between the re-integrated solution and the final node of the $\mathcal{PSOPT}$ solution is an indication of the validity of the $\mathcal{PSOPT}$ solution, i.e., the constraints are adhered to across the full trajectory

and not only at the nodes. Secondly, node-to-node integration takes the state at node $N = 1$ and integrates until the next node, and repeats this process for nodes $N \in [2, N-1]$. Again, the solar-sail pitch angle is interpolated from the $\mathcal{PSOPT}$ solution using the shape-preserving piecewise cubic method. Node-to-node integration is relevant to gain insight into the control effort and the trajectory when the solution accuracy from the full re-integration is not sufficient yet. The validity of the $\mathcal{PSOPT}$ solution is assessed by a summation over all nodes of the difference in state between the re-integrated solution and the $\mathcal{PSOPT}$ solution. This method mitigates any divergence behaviour as it effectively initialises the integration multiple times across the $\mathcal{PSOPT}$ solution. The same error values as in the initial guess generation of $\Delta r \leq 10^{-3}$ and $\Delta v \leq 10^{-2}$ are taken as a reference to regard a trajectory as valid [28].

B. Optimal Control Problem

The weights w_1, w_2, and w_3 in the cost function that is defined in Eq. (24) can be varied to change the relative importance. In an effort to eliminate the subjectivity in choosing a set of weights, a large number of combinations of sets of weights are evaluated. Consequently, an inventory of the capabilities of using a solar sail for solar-storm detection is obtained.

1. Inventory

In total, approximately 600 combinations have been evaluated with the weights ranging between $w_1 = [0, 1]$, $w_2 = [0, 4000]$, and $w_3 = [0, 1]$. These ranges have been chosen such that each component in the cost function can be emphasised with equal (relative) importance, as the magnitude of d_{avg} is smaller than the magnitude of k_{avg} and k_{max}. Trajectories N_1 and N_2 (Fig. 14), are used as an initial guess for the set of weights $[w_1, w_2, w_3] = [1, 0, 0]$ and $[w_1, w_2, w_3] = [0, 0, 1]$, respectively. Next to that, a continuation method is employed in which the set of weights are gradually varied and the solution of the previous optimisation problem is taken as an initial guess. It is expected that this method increases the convergence (rate) of the full inventory. The continuation method is executed in a sequential order where two weights are kept fixed and one is increased gradually. For example, the solution to the optimisation problem with weights $[w_1, w_2, w_3] = [1, 2000, 0.5]$ is used as an initial guess for the optimisation problem with weights $[w_1, w_2, w_3] = [1, 2000, 0.55]$. If an optimisation problem does not converge, e.g., the maximum number of iterations is exceeded, other initial guesses are provided as an input. Taking the example above, alternative initial guesses would be $[w_1, w_2, w_3] = [1, 2000, 0.6]$ or $[w_1, w_2, w_3] = [1, 1750, 0.55]$.

The maximum number of iterations is set to 3000, the convergence tolerance is set to 10^{-4}, and the number of LGL nodes has been set to $N = 25$ taking computational limitations into account. The inventory of the converged solutions is presented in Fig. 15. In addition, four trajectories are indicated that have the following properties:

- Trajectory I is selected to be the trajectory that maximises the average increase in warning time: $\max(k_{\text{avg}})$.
- Trajectory II is selected to be the trajectory that minimises the average distance to the CME-axis: $\min(d_{\text{avg}})$.

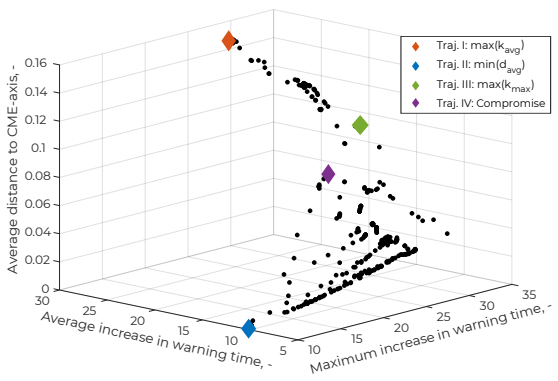

(a) Isometric view.

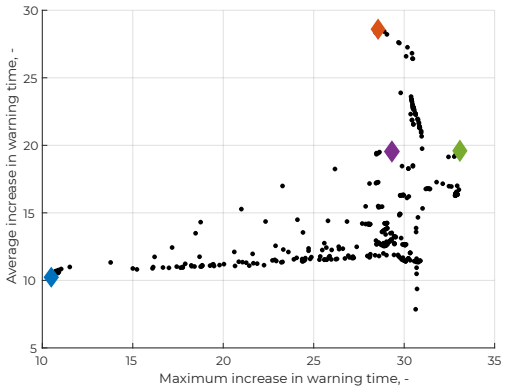

(b) Side view displaying the correlation between the maximum and average increase in warning time.

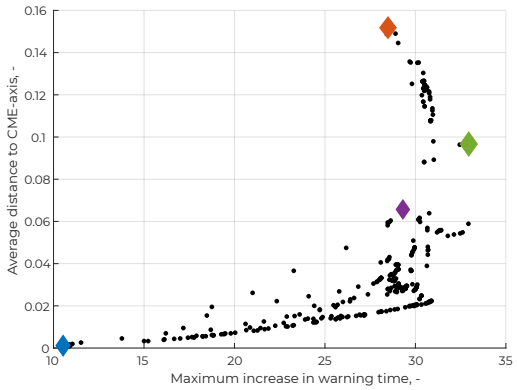

(c) Side view displaying the correlation between the maximum increase in warning time and the average distance to the CME-axis.

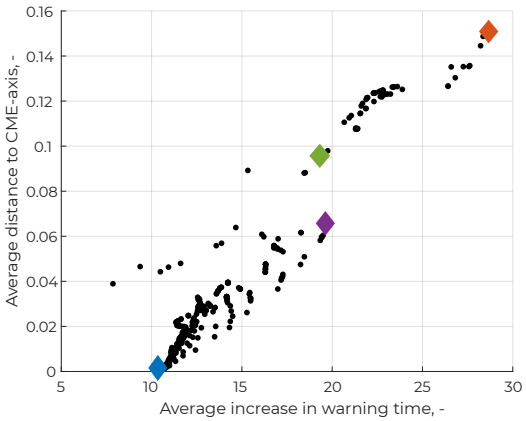

(d) Side view displaying the correlation between the average increase in warning time and the average distance to the CME-axis.

Fig. 15 $\mathcal{PSOPT}$: Inventory of the properties of converged solar-sail trajectories using a number of nodes $N = 25$.

- Trajectory III is selected to be the trajectory that maximises the maximum increase in warning time: $\max(k_{\max})$.
- Trajectory IV is selected to be the trajectory that is a compromise between the three objective value elements (k_{avg}, d_{avg}, and $k_{\max}$).

Several observations in the solar-sail inventory can be made. For an average and maximum increase in warning time of a factor 10, the average distance to the CME-axis is zero (see the blue marker in Fig. 15). In addition, the maximum increase in warning time can be as large as a factor of approximately 31 while keeping both the average increase in warning time and the average distance to the CME-axis small as indicated by the black dots in the bottom right of Fig. 15b and Fig. 15c. Increasing the average increase in warning time does however impact the average distance to the CME-axis; these two objectives demonstrate a linear relationship as presented in Fig. 15d. This trend can be

explained by looking at the definition of how the increase in warning time is defined in Fig. 9; any point within the CME detection zone takes the nearest point on the CME-axis as a reference to determine the increase in warning time. If the average increase in warning time is desired to be increased, the spacecraft tends to not only go upstream of the CME-axis, but also away from the CME-axis to remain in the vicinity of an AEP. This observation can be illustrated by taking a detailed look at trajectories I and II (indicated by the red and blue marker) from Fig. 15, obtained with weights $[w_1, w_2, w_3] = [1, 0, 0]$ and $[1, 4000, 0]$, respectively. The positional state and control profiles are displayed in Fig. 16 and their properties are presented in Table 6. As can be seen from the figure, solely maximising the average increase in warning time results in a trajectory that is (almost) stationary in close proximity of an AEP furthest upstream of the CME-axis, while still remaining within the CME detection zone. The trajectory is different from the result obtained by the GA presented in Section III.B.3, which is due to the decision variable bound of p_1, specifying it had to be an AEP in between P_3 and SL_1. On the other side, solely optimising for $\min(d_{\text{avg}})$ results in a trajectory that remains (almost) stationary in close proximity of an AEP on the CME-axis. Note that the magnitude of the solar-sail pitch angle, and therefore the solar-sail control effort, is small as displayed in Fig. 16b.

Table 6 $\mathcal{PSOPT}$: properties of trajectories I-IV that are displayed in Fig. 16 and Fig. 18.

Trajectory	k_{avg}, -	d_{avg}, -	k_{max}, -	T, yr
I: $\max(k_{\text{avg}})$	28.48	0.1508	28.51	1.60
II: $\min(d_{\text{avg}})$	10.51	7.328e-4	10.53	4.64
III: $\max(k_{\text{max}})$	24.22	0.1017	29.46	2.76
IV: Compromise	19.09	0.05389	29.17	4.69

The two trajectories displayed in Fig. 16 have a re-integration error well below $\Delta r \leq 10^{-3}$ and $\Delta v \leq 10^{-2}$ such that the trajectories can be regarded as feasible. However, the re-integration errors of the trajectories that are associated with $\max(k_{\text{max}})$ and a compromise between the three elements, trajectory III and IV ($[w_1, w_2, w_3] = [1, 125, 0.125]$ and $[1, 250, 0.15]$, respectively, in Eq. (24)), as indicated in Fig. 15 are both in the order of 0.4 and are therefore not valid [28]. An explanation for these relatively high re-integration errors can be explained by the number of nodes that is used in the optimisation. For a small number of nodes, $N = 25$ in this case, the solar-sail pitch angle interpolation becomes less accurate as there are larger time steps in-between data points, resulting in an overall less accurate re-integration. Consequently, before any conclusions can be drawn from trajectory III and IV, the optimisation solutions should be refined, i.e., more nodes should be added, which might result in valid and therefore realistic trajectories.

2. Mesh-refinement

The coarse solutions that are presented in the solar-sail inventory do not all comply with the feasibility requirement and it is expected that adding more LGL nodes to the solution decreases re-integration errors. $\mathcal{PSOPT}$ has a built-in

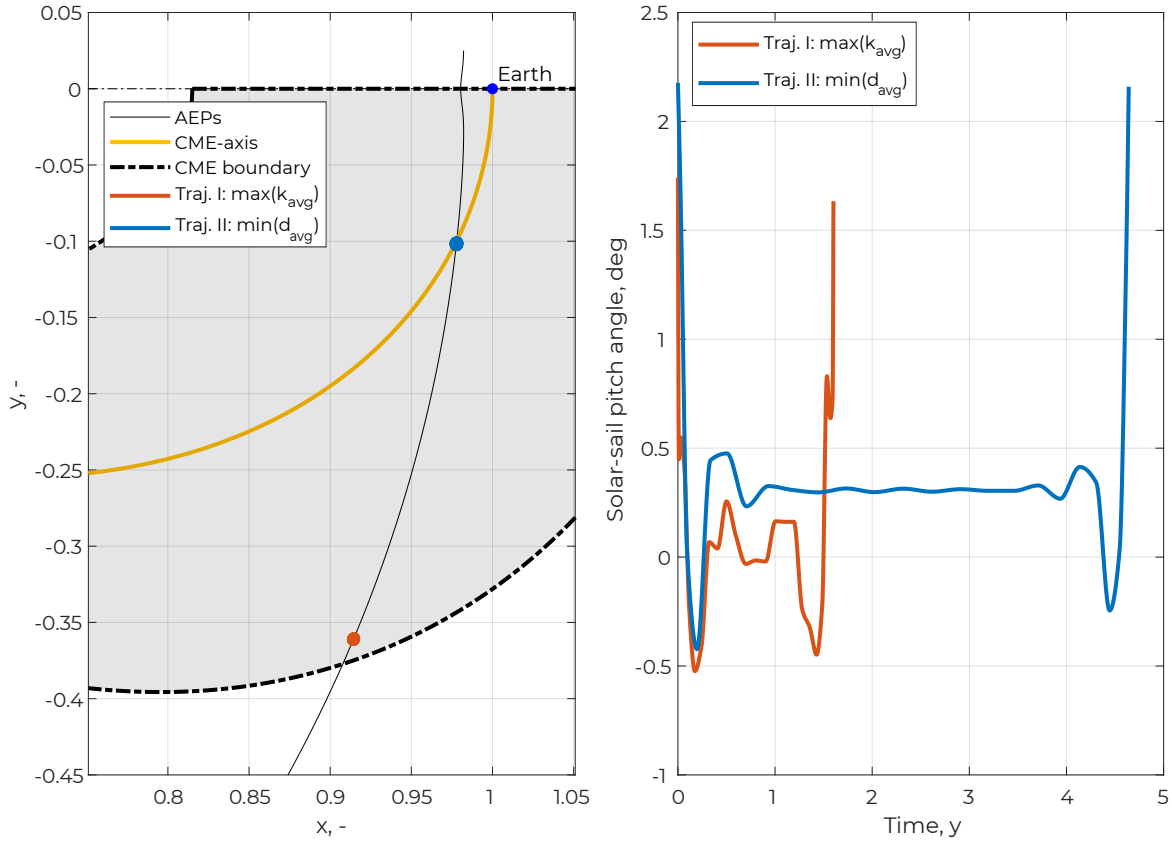

(a) Positional state. **(b) Control profile.**

Fig. 16 $\mathcal{PSOPT}$: trajectory I (max(k_{avg})) and II (min(d_{avg})) within the solar-sail inventory using a number of nodes of $N = 25$ for both trajectories.

functionality to gradually add more nodes to the optimisation problem, using the solution of the previous evaluation as an initial guess [18]. This mesh-refinement process is executed on trajectories III and IV until the validity requirement is met. The re-integration errors as a function of the number of nodes of the solution can be seen in Fig. 17.

It is observed that trajectory III complies with the validity requirement, both in position and velocity, at $N = 65$ and that trajectory IV satisfies it at $N = 85$. The mesh-refined trajectories III and IV are displayed in Fig. 18 and their properties are displayed in Table 6. Note that for trajectory III the maximum increase in warning time has reduced from approximately 32.93 to 29.46 whereas the average increase in warning time increased from 19.23 to 24.22 and the distance to the CME-axis reduced from 0.097 to 0.090. This change in properties is because the solution for $N = 25$ did not satisfy the path constraint outlined in Eq. (31) *in-between* the nodes, which resulted in a trajectory that was partly spent outside of the CME detection zone. As a result, the spacecraft was able to travel further upstream of the CME-axis. Computations have been done where the path constraint outlined in Eq. (31) is dropped, and it is observed

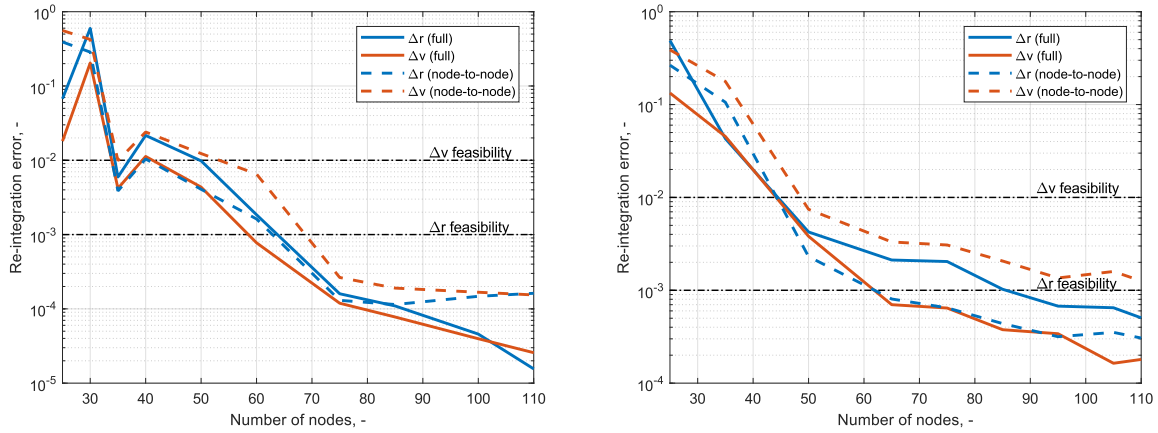

(a) Trajectory III (max($k_{\max}$)) **(b) Trajectory IV (compromise)**

Fig. 17 Full and node-to-node re-integration errors as a function of the number of nodes used for the optimisation solution of trajectory III (max($k_{\max}$)) and IV (compromise).

that substantially higher values for the maximum increase in warning time can be obtained. The mesh-refinement also explains the increase in the average increase in warning time and the decrease of the average distance to the CME-axis, as the mesh-refinement resulted in a trajectory where the spacecraft spends *all* of its time in the CME detection zone. In addition, it is logical that trajectory III, i.e., maximising the maximum increase in warning time, was not obtained with weights $[w_1, w_2, w_3] = [0, 0, 1]$. It is more a coincidence where the optimisation solution would show the behaviour that only *at* the nodes the path constraint in Eq. 31 is satisfied, such that a spacecraft could travel outside the CME zone *in-between* the nodes to go further upstream of the CME-axis. In fact, Fig. 15 displays that the "real" maximum value for $k_{\max}$, i.e., approximately 29.5, was obtained by numerous combinations of $[w_1, w_2, w_3]$. Trajectory IV shows approximately the same properties for $N = 25$ and $N = 85$ (apart from the re-integration error) as this trajectory for $N = 25$ did not travel outside the CME zone *in-between* the nodes.

The value for the maximum increase in warning time is approximately the same for the two trajectories. In addition, this value closely corresponds to the value for the maximum increase in warning time obtained for trajectory I. It gives the impression that such a value can easily be obtained. It can be concluded that the optimisation is more a trade-off between the average increase in warning time and the average distance to the CME-axis, as was also observed in Fig. 15 by the larger correlation between these two elements.

The optimised and mesh-refined solutions for trajectory III and IV show a multi-loop trajectory. One loop of this trajectory has the goal to travel furthest upstream of the CME-axis. This loop is almost identical for the two trajectories (Fig. 18a) and is characterised by the maximum value in solar-sail pitch angle of approximately -15 deg. The other loops are a result of a trade-off between the average increase in warning time and the average distance to the CME-axis; if a loop is closer to the CME-axis, both the average increase in warning time and the average distance to the CME-axis are

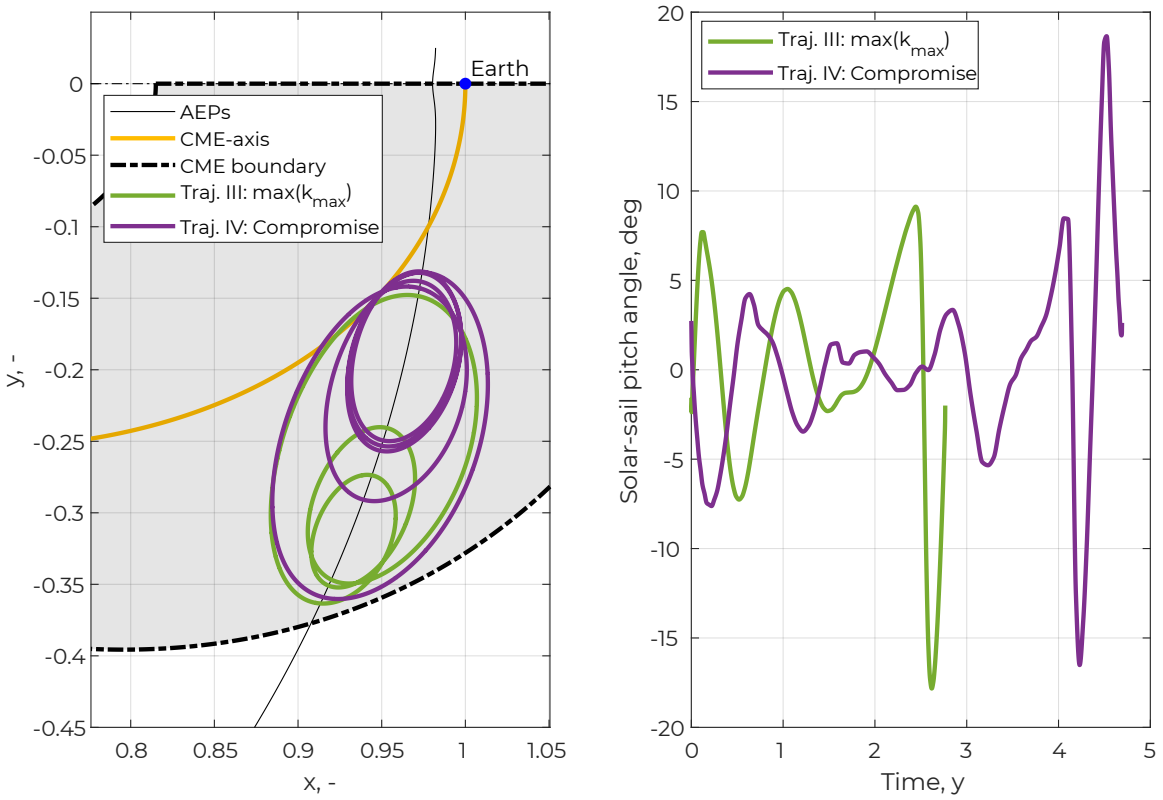

(a) Positional state. **(b) Control profile.**

Fig. 18 $\mathcal{PSOPT}$: the mesh-refined trajectories III (max($k_{\max}$)) and IV (compromise) within the solar-sail inventory using a number of nodes of $N = 65$ and $N = 85$, respectively.

smaller than when this loop is further upstream of it. Lastly, note that it is assumed that the solar sail has no constraint on the rate of change of the pitch angle, while in reality there is a practical limitation. The results show a maximum value of this rate of change in trajectory IV of 0.33 degrees per *day*. Compared to a practical limitation of the rate of change of 144 degrees per *hour*, the trajectories still satisfy the practical constraint [31].

3. Overview

An overview of the properties of the four trajectories that were outlined in the previous sections is given in Table 6. In addition, the increase in warning time and distance to the CME-axis as a function of the orbital period for trajectories I-IV are presented in Fig. 19. As was mentioned before, trajectories I and II have been optimised in $\mathcal{PSOPT}$ using a number of LGL nodes of $N = 25$, while trajectories III and IV require a number of nodes of $N = 65$ and $N = 85$, respectively, such that the re-integration errors are below the validity constraint. Note that the properties of trajectories I and II remain (practically) constant throughout the orbital period. This is because the optimised trajectories are essentially stationary in close proximity of an AEP within the CME detection zone. In addition, note that trajectories III

and IV show the same oscillatory behaviour in the properties as in the state and control profile presented in Fig. 18. As was said before, one of the loops in the trajectory has the purpose to maximise the maximum increase in warning time, while the other loops are a balance between the average increase in warning time and the average distance to the CME-axis. Finally, note that other points in the inventory (Fig. 15) can be selected to obtain a trajectory with desired properties. For instance, while still reaching the maximum increase in warning time, the balance between the average increase in warning time and the average distance to the CME-axis, i.e., probability of CME detection, can be shifted to satisfy a particular requirement/preference. Consequently, a possible mesh-refinement using the strategy outlined in the previous section may be performed to render a trajectory valid.

The periodic solar-sail trajectories displayed in this section exhibit an (average and maximum) increase in solar-storm warning time in the range of a factor 20 to 30 with respect to current missions at L_1 (which achieve a warning time of 30 to 60 minutes). This results in an absolute warning time of approximately 10 to 30 hours. It is well short of the requirement of two to three days to fully prepare for disruption outlined in Ref. [6]. It is therefore advised to consider other methods such as a spacecraft at L_5 that allows for earlier *predictions* of solar storms: a spacecraft from the viewpoint of L_5 is able to look at the surface of the Sun that rotates towards Earth four to five days later [1]. Still, a spacecraft that enables for earlier *detection* is essential in preparing society for an event as it takes away the (great) uncertainty of the magnitude and direction associated with a solar storm [1, 6]. A combination of a spacecraft at L_5 and a solar-sail spacecraft in a periodic solar-sail trajectory outlined in this section may therefore be the solution to receive a timely warning of an approaching solar storm.

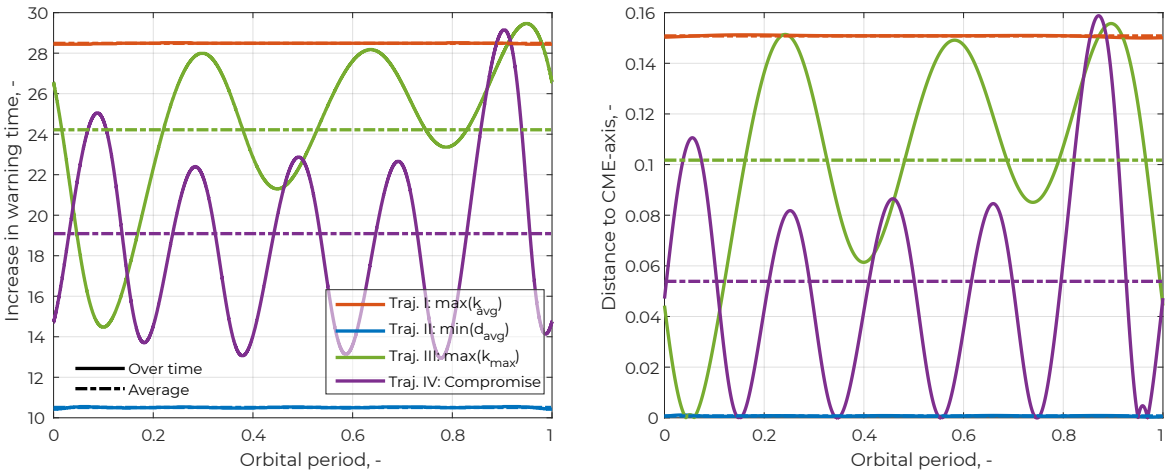

(a) Increase in warning time. **(b) Distance to the CME-axis.**

Fig. 19 $\mathcal{PSOPT}$: the objective values as a function of the orbital period for trajectories I-IV.

V. Sensitivity Analysis

The results that are presented in the previous section have been computed using:

1) An ideal solar-sail model
2) A lightness number of $\beta = 0.05$
3) A constant CME size

In this section, the impact of these model choices are assessed by implementing an optical solar-sail model, by varying the lightness number, and by changing the CME size.

A. Optical Solar-sail Model

The optical solar-sail model is given in Section II.B and the corresponding set of coefficients are presented in Table 1, which are retrieved from NASA's NEA Scout mission [23]. The trajectories I-IV, obtained with an ideal solar-sail model, are used as an initial guess to generate trajectories I_{opt}-IV_{opt}. Note that the subscript "opt" denotes the use of an optical solar-sail model and that the same set of weights ($[w_1, w_2, w_3]$) are selected that have been used to compute trajectory I-IV. An overview of the properties and the difference with respect to the ideal solar-sail model can be seen in Table 8. The difference is computed as

$$\Delta_{\text{id}} = \left| \frac{i_{\text{opt}} - i_{\text{id}}}{i_{\text{id}}} \right| \text{x}100\% \tag{32}$$

where i is the property of the trajectory (k_{avg}, d_{avg}, k_{max}), and the subscript "id" denote the use of an ideal solar-sail model. It is observed that the difference with respect to an ideal solar-sail model remains relatively small; the properties of trajectories I_{opt}, III_{opt}, and IV_{opt} have at most a difference of approximately 2%. These relatively small differences can be attributed to the fact that the solar-sail pitch angle remains small ($\alpha \in [-20 \text{ deg}, 20 \text{ deg}]$) for all trajectories (both for an ideal and optical solar-sail model). As a result, the solar-sail acceleration component tangent to the sail (Eq. (7)) remains small meaning that the difference between the ideal and optical solar-sail model is kept to a minimum [8]. Still, an explanation for the difference in performance can be attributed to the magnitude of the normal solar-sail acceleration, which is larger for an ideal solar-sail model than for an optical sail model.

Table 7 $\mathcal{PSOPT}$: properties of trajectories I-IV evaluated using an optical solar-sail model and the difference with respect to the ideal solar-sail model, Δ_{id}. The models are described in Section II.B and the coefficients used in the models are given in Table 1.

Trajectory	k_{avg}, -	Δ_{id} (%)	d_{avg}, -	Δ_{id} (%)	k_{max}, -	Δ_{id} (%)
I_{opt}: max(k_{avg})	28.36	0.42	0.1509	0.07	28.39	0.42
II_{opt}: min(d_{avg})	10.12	3.71	0.0007713	5.25	10.14	3.70
III_{opt}: max(k_{max})	24.11	0.45	0.1023	0.59	29.31	0.51
IV_{opt}: Compromise	19.02	0.37	0.05498	2.02	29.00	0.58

The relatively larger differences of 3-5% that are associated with trajectory II_{opt} can be related to two phenomena.

The first phenomenon, which explains the difference in the average and maximum increase in warning time, relates to a steeper gradient of the CME-axis as it approaches the Earth (Fig. 3). The decrease in the solar-sail acceleration of the optical solar-sail model compared to the ideal solar-sail model results in an AEP shift backwards, i.e., further away from the Sun. Trajectory $\mathrm{II_{opt}}$ is practically a trajectory that is stationary in close proximity of the AEP on the CME-axis, relatively close to the Earth compared to trajectories $\mathrm{I_{opt}}$, $\mathrm{III_{opt}}$, and $\mathrm{IV_{opt}}$. Therefore, taking the steeper gradient of the CME-axis as it approaches the Earth into account, trajectory $\mathrm{II_{opt}}$ (evaluated with an optical solar-sail model) has a larger shift towards the Earth than the other trajectories, explaining the larger difference. The second phenomenon explains the relatively large percentage difference regarding all three properties, and especially the average distance to the CME-axis. The values of the properties of trajectory $\mathrm{II_{opt}}$ are smaller than the values of the properties for trajectories $\mathrm{I_{opt}}$, $\mathrm{III_{opt}}$, and $\mathrm{IV_{opt}}$. Taking the average distance to the CME-axis as an example, which is in the order of $O(10^{-4})$ for trajectory $\mathrm{II_{opt}}$ compared to $O(10^{-1})$, $O(10^{-1})$, and $O(10^{-2})$ for trajectories $\mathrm{I_{opt}}$, $\mathrm{III_{opt}}$, and $\mathrm{IV_{opt}}$, respectively, a small increase of this property leads to a relatively large percentage difference. Still, the magnitude of the average distance to the CME-axis of trajectory $\mathrm{II_{opt}}$ remains small $O(10^{-4})$.

The coefficient set for the optical solar-sail model has an uncertainty as outlined in Table 1. It raises the question whether and how much these uncertainties impact the trajectories. Therefore, trajectories $\mathrm{I_{opt}}$-$\mathrm{IV_{opt}}$ have been computed using the lower and upper bound of the coefficient set which is defined as

$$C_l = C_{\mathrm{nom}} - \mathrm{Uncertainty}_C \qquad C_u = C_{\mathrm{nom}} + \mathrm{Uncertainty}_C \tag{33}$$

where C is the coefficient set of the optical solar-sail model, the subscript "l" and "u" indicate the lower and upper bound of the coefficient set, respectively, and the subscript "nom" denotes the nominal value. Trajectories $\mathrm{I_{opt}}$-$\mathrm{IV_{opt}}$ have been used as an initial guess to compute the trajectories using the lower and upper bound, which are denoted as trajectories $\mathrm{I_{opt,l}}$-$\mathrm{IV_{opt,l}}$ and $\mathrm{I_{opt,u}}$-$\mathrm{IV_{opt,u}}$, respectively. An overview of the properties and the difference with respect to the nominal optical solar-sail model, Δ_{opt}, is presented in Table 8. The difference is computed using Eq. 32 but now using the values of $i_{\mathrm{opt},l}$ or $i_{\mathrm{opt},u}$ and i_{opt}, respectively. Overall, it can be observed that the percentage differences remain mostly relatively small compared to the properties of trajectories $\mathrm{I_{opt}}$-$\mathrm{IV_{opt}}$: <0.5%. The property that does have a larger percentage difference is the average distance to the CME-axis. Again, due to the same reason for the difference between the (nominal) optical and ideal solar-sail model, it can be attributed to the fact that the magnitude of the average distance to the CME-axis is relatively small ($O(10^{-4})$). Resulting from that, a small increase/decrease of this property results in a relatively larger percentage difference.

All in all, as the percentage differences Δ_{id} and Δ_{opt} are relatively small, it can be concluded that the use of an optical solar-sail model and its uncertainty in the coefficient set does not lead to a considerable difference in the (properties of the) optimised trajectories as compared to an ideal solar-sail model. As a result, the ideal solar-sail model can be used

to model the solar-sail dynamics with sufficient accuracy. However, trajectories I_{opt}-IV_{opt} will be used in subsequent sections as it is slightly more realistic and therefore more relevant.

Table 8 $\mathcal{PSOPT}$: properties of trajectories I-IV evaluated with the lower and upper bound of the optical solar-sail model coefficient set using the uncertainties from Ref. [23] and the difference with respect to the (nominal) optical solar-sail model coefficient set, Δ_{opt}.

Trajectory	Lower bound of the coefficient set (C_l)						Upper bound of the coefficient set (C_u)					
	k_{avg}, -	Δ_{opt} (%)	d_{avg}, -	Δ_{opt} (%)	k_{max}, -	Δ_{opt} (%)	k_{avg}, -	Δ_{opt} (%)	d_{avg}, -	Δ_{opt} (%)	k_{max}, -	Δ_{opt} (%)
$I_{opt,l/u}$: max(k_{avg})	28.35	0.035	0.1509	0.00	28.37	0.070	28.37	0.035	0.1509	0.00	28.39	0.00
$II_{opt,l/u}$: min(d_{avg})	10.09	0.30	0.0007903	2.46	10.1	0.39	10.16	0.40	0.0007821	1.40	10.17	0.296
$III_{opt,l/u}$: max(k_{max})	24.10	0.041	0.1023	0.00	29.29	0.068	24.14	0.12	0.1024	0.098	29.31	0.00
$IV_{opt,l/u}$: Compromise	19.01	0.053	0.05516	0.33	29.00	0.00	19.03	0.053	0.05489	0.16	29.02	0.069

B. Change in Lightness Number

Up to now, all trajectories have been computed using a lightness number of $\beta = 0.05$ which is in accordance with expected near-term technological advances [22]. Current state-of-the-art solar-sail technology can achieve lightness numbers of approximately 0.01 as NASA's NEA Scout mission will demonstrate [32]. In the (near- to far-term) future it is expected that solar-sail technology can achieve values of up to $\beta = 0.1$ [33]. In order to gain insight into the current and near to far-term possibilities regarding the use of solar sailing in solar-storm detection, trajectories I_{opt}-IV_{opt} will be computed for $\beta = [0.01, 0.1]$ and will be referred to as $I_{opt,\beta}$-$IV_{opt,\beta}$. Note that the optical solar-sail model is utilised here and that the same set of weights, $[w_1, w_2, w_3]$, is taken that has been used to compute trajectories I-IV. The optimised solutions are obtained using a continuation method on the lightness number, similar to the method used in previous sections.

An overview of the optimised solutions and the performance difference with respect to the nominal solution for $\beta = 0.05$ of trajectories $I_{opt,\beta}$ and $II_{opt,\beta}$ are presented in Fig. 20. Note that all resulting trajectories are (still) stationary trajectories in close proximity of an AEP. For an increase in lightness number, the surface of AEPs shifts sunwards as was observed in Fig. 4. As a result, trajectories $I_{opt,\beta}$ and $II_{opt,\beta}$ will shift sunwards for an increase in lightness number, thereby increasing the average and maximum increase in warning time. The percentage difference of these two properties is approximately 1% and 8% per change in lightness number of $\beta = 0.01$, respectively. The difference in these two magnitudes can be attributed to the two phenomena that were outlined in Section V.A which are related to the small magnitude of the property values and the steeper gradient of the CME-axis as it approaches the Earth. In addition, the average distance to the CME-axis decreases for an increase in lightness number for trajectories $I_{opt,\beta}$ and $II_{opt,\beta}$. This decrease for trajectory $I_{opt,\beta}$ has to do with the shift of the surface of AEPs sunwards, which indirectly reduces the average distance to the CME-axis as well. Instead, the relatively larger percentage difference for the average distance to the CME-axis for trajectory $II_{opt,\beta}$ can be explained by the relatively small property value ($O(10^{-4})$).

The solutions for $\beta \in [0.01, 0.1]$ and the performance difference with respect to the nominal solution of trajectories

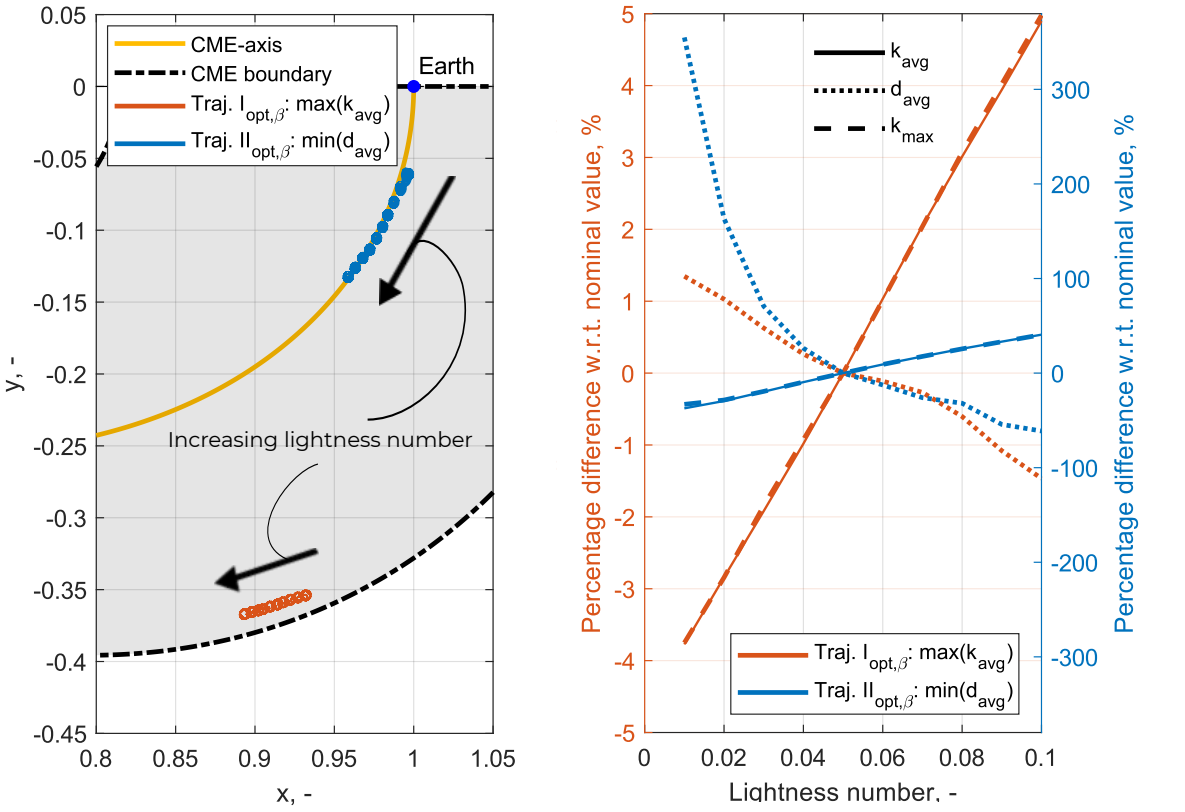

(a) Positional state.

(b) Performance difference with respect to the nominal lightness number.

Fig. 20 $\mathcal{PSOPT}$: trajectories $\mathrm{I}_{\mathrm{opt},\beta}$ and $\mathrm{II}_{\mathrm{opt},\beta}$ using $\beta \in [0.01, 0.1]$ and the difference in performance with respect to the nominal solution.

$\mathrm{III}_{\mathrm{opt},\beta}$ and $\mathrm{IV}_{\mathrm{opt},\beta}$ are given in Fig. 21. Note that Fig. 21a only shows the part of the trajectory where the maximum increase in warning time is achieved, to maintain a clear overview of the trajectories and indication of the trend in positional state for an increase in lightness number. In general, an increase in lightness number increases the average and maximum increase in warning time by approximately 1% per change in lightness number of $\beta = 0.01$ for both trajectory $\mathrm{III}_{\mathrm{opt},\beta}$ and $\mathrm{IV}_{\mathrm{opt},\beta}$. This trend is approximately the same as the trend that was obtained for trajectory $\mathrm{I}_{\mathrm{opt},\beta}$. In addition, the average distance to the CME-axis differs by approximately 2% and 5% per change in lightness number of $\beta = 0.01$ for trajectory $\mathrm{III}_{\mathrm{opt},\beta}$ and $\mathrm{IV}_{\mathrm{opt},\beta}$, respectively. However, these trends are general; as the lightness number tends towards $\beta = 0.01$ and 0.1 (furthest away from the nominal value of $\beta = 0.05$), this trend is no longer valid; in particular for the average distance to the CME-axis for trajectory $\mathrm{III}_{\mathrm{opt},\beta}$ and for the average increase in warning time for trajectory $\mathrm{III}_{\mathrm{opt},\beta}$ and $\mathrm{IV}_{\mathrm{opt},\beta}$. This observation can most likely be assigned to the set of weights, $[w_1, w_2, w_3]$, used in Eq. 24. The set of weights are chosen based on the inventory of solar-sail trajectories for $\beta = 0.05$, as displayed in Fig. 15. When the lightness number changes, the dynamics of the problem vary considerably meaning that the inventory

of Fig. 15 might not be representative anymore. Therefore, a new set of weights should be chosen for a change in lightness number, especially when the lightness number differs substantially from the nominal value of $\beta = 0.05$. This is illustrated by changing the set of weights ($[w_1, w_2, w_3] = [0.98, 112, 0.125]$) for trajectory $\text{III}_{\text{opt},0.01}$, indicated by the grey dots in Fig. 21b, from which it can be seen that the properties approximately continue on the same trend as observed near $\beta = 0.05$.

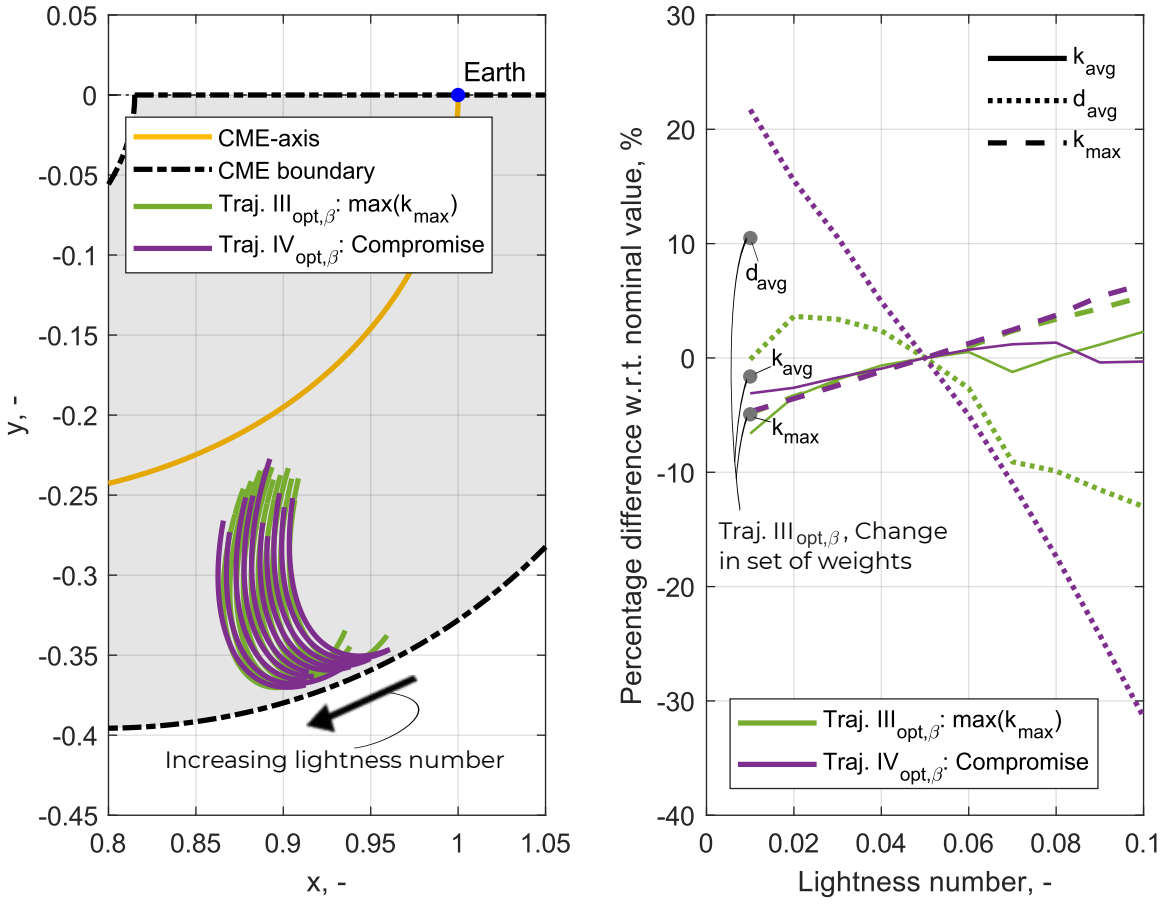

(a) Positional state. Note that only the part is highlighted where the maximum increase in warning time is achieved.

(b) Performance difference with respect to the nominal value as a function of lightness number.

Fig. 21 $\mathcal{PSOPT}$: trajectories $\text{III}_{\text{opt},\beta}$ and $\text{IV}_{\text{opt},\beta}$ using $\beta \in [0.01, 0.1]$ and the difference in performance with respect to the nominal solution (which is the solution for $\beta = 0.05$).

Overall, it can be concluded that an increase in lightness number increases the performance (increases k_{avg} and k_{max}, decreases d_{avg}) of the trajectories. The magnitude of the increase in performance depends on the nature of the trajectory; trajectories closer to the Earth benefit more from an increase in lightness number than trajectories that are further away from Earth.

C. Change in Coronal Mass Ejection size

The CME-model that was laid out in Section II.C is based on an average of all detected CMEs in solar cycle 23 (1996 - 2009) [25]. An implicit assumption that is made in this paper is that the CME-model is constant for all CMEs while the CME size in reality varies [25]. The assumption has implications on the probability that a CME is detected as a variation in CME size might result in a trajectory that no longer spends the full orbital period in the CME detection zone (i.e., within the CME boundary lines).

While still assuming the CME-axis to be constant for all CMEs that are on a trajectory to intersect the Earth, the radial size can be varied. For the two-dimensional formulation that is used in this paper, the radial size reduces to the width of the CME projected onto the ecliptic plane. The radial size distribution for all detected CMEs during solar cycle 23 measured at the Sun-Earth L_1 point can be seen in Fig. 22a [25]. Note that the mean value, 0.33 AU, is equal to the nominal radial size of the CME-model used in this paper (Fig. 3). The result of an increase or decrease in CME radial size on the CME-model is presented in Fig. 22b. It can be seen that the CME covers more area (compared to the "nominal" CME-model) as the radial size increases. On the contrary, the region for CME detection becomes smaller as the radial size of the CME decreases.

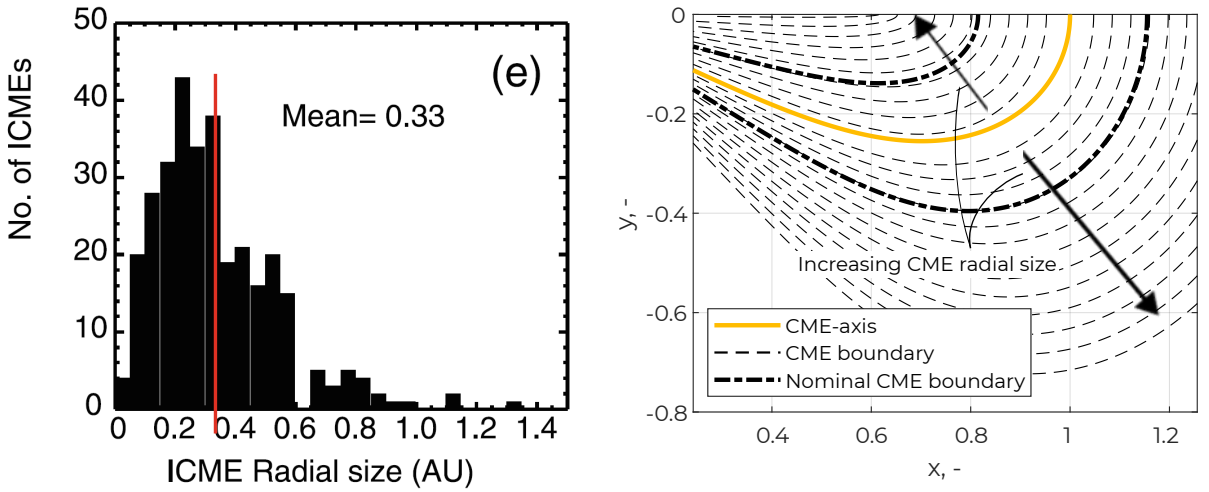

(a) CME radial size distribution [25].

(b) The result of a change in radial size on the CME-model.

Fig. 22 CME radial size distribution of all detected CMEs during solar cycle 23, measured at the Sun-Earth L_1 point [25], and its effect on the CME-model.

The probability that a spacecraft in a particular trajectory detects a CME of a certain radial size, P_{RS} (where the subscript "RS" refers to radial size), is quantified by how much time the solar-sail trajectory spends in the CME detection zone, t, as

$$P_{\mathrm{RS}} = \frac{t}{T}\mathrm{x}100\% \tag{34}$$

where T is the orbital period of the trajectory. The *total* probability that a spacecraft in a particular trajectory detects a

CME, P_{total}, can be estimated using the CME radial size distribution (Fig. 22a) as

$$P_{\text{total}} = \sum_{\text{RS=min(RS)}}^{\text{RS=max(RS)}} P_{RS} \cdot \frac{f_{RS}}{f} \tag{35}$$

where min(RS) and max(RS) are the minimum and maximum radial sizes of the detected CMEs, f_{RS} is the number of detected CMEs with radial size RS (Fig. 22a), and f is the *total* number of detected CMEs. Note that all of the numbers are based on data from solar cycle 23 [25].

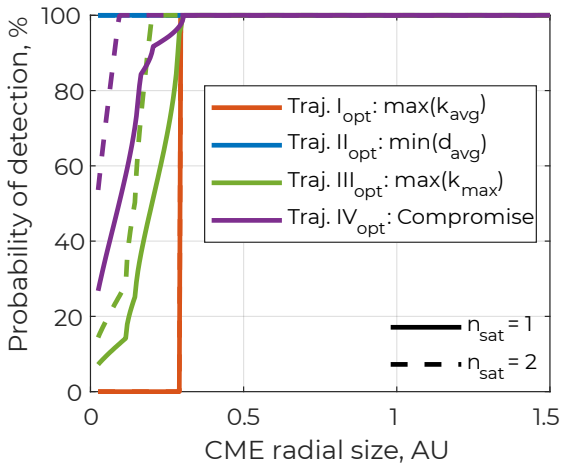

Fig. 23 The probability of detection (Eq. (34)) as a function of the CME radial size for one or two spacecraft in trajectories I_{opt}-IV_{opt}, based on CME data of solar cycle 23 [25].

The probability that a CME of a certain radial size is detected is assessed for the nominal ($\beta = 0.05$) trajectories I_{opt}-IV_{opt} using Eq. (34) and can be seen in Fig. 23. In addition, taking Eq. (35), the *total* probability that a CME is detected by a spacecraft in these trajectories is given in Table 9. The probabilities have also been computed for the case that there are two spacecraft equally spaced in time in the respective trajectory. Several observations can be made from the results. First, for the nominal radial size of 0.33 AU and larger, the probability of detection for all trajectories is 100%. This is due to the path constraint that was imposed on the optimal control problem which stated that the trajectory had to remain in the *nominal* CME detection zone (Eq. (31)). Second, CMEs smaller than 0.33 AU are never detected by trajectory I_{opt} and always detected by trajectory II_{opt}, which are due to the nature of the trajectories as explained in Section IV.B. As a result, the total probability of detection is 48.73% and 100.0% for a spacecraft in trajectory I_{opt} and II_{opt}, respectively. Note that it is expected that trajectory I_{opt} would have a total probability of detection of 50% as the trajectory is stationary in close proximity of an AEP located at the boundary of the *mean* CME radial size. The slight mismatch (1.27%) can be assigned to the fact that the probability distribution has been calculated on the basis of the frequency bins in Fig. 22a; it is assumed that the mean CME radial size of the frequency bin is midway, while in reality this may not be the case. Third, the probability of detection for a spacecraft in trajectory IV_{opt} is larger than the

probability for trajectory III_{opt}, equal to 89.12% and 72.22%, respectively. Although these trajectories are of the same nature (multi-loop, as presented in Section IV.B), the average distance to the CME-axis is smaller for trajectory IV_{opt} than trajectory III_{opt}. As a result, trajectory IV_{opt} spends more time closer to the CME-axis than trajectory III_{opt}, thereby increasing its total probability that a CME is detected. Finally, adding a second spacecraft in the trajectory only results in a larger CME detection probability for trajectories III_{opt} and IV_{opt}, equal to 86.68% and 98.64%, respectively, as the total fraction of time that one of the spacecraft spends in the CME detection zone increases. Trajectory I_{opt} and II_{opt} are stationary in close proximity of an AEP (Section IV.B), which leaves the probability of CME detection unaffected by the addition of a spacecraft (in the same trajectory).

Table 9 The total probability that a CME is detected by a spacecraft in trajectories I_{opt}-IV_{opt}, based on CME data of solar cycle 23 [25].

Trajectory		I_{opt}: max(k_{avg})	II_{opt}: min(d_{avg})	III_{opt}: max(k_{max})	IV_{opt}: Compromise
P_{total}, %	$n_{sc} = 1$	48.73	100.0	72.22	89.12
	$n_{sc} = 2$	48.73	100.0	86.68	98.64

Ideally, a CME that is heading towards Earth should always be detected, which leaves trajectory II_{opt} as the only desired option. However, the results in Table 9 should be taken with reservation as it is based on multiple assumptions, such as a constant CME-axis for all CMEs. In addition, the probability characteristic does not account for the fact that a spacecraft in the vicinity of the CME detection zone, but not in it, can still provide valuable data, e.g., by using optical instruments [34]. Finally, trajectories I_{opt}-IV_{opt} are computed with the nominal CME-model (Fig. 3), not taking any detection probabilities or CME size variations into account. This leaves room for subsequent analyses/optimisations that do consider these factors, possibly increasing the probability characteristics.

Taking both the performance (Table 8) and the probability that a CME is detected into account, trajectory IV_{opt} can be regarded as the "most optimal" trajectory out of the four. Trajectories I_{opt} and III_{opt} have a relatively small probability that a spacecraft in this trajectory detects a CME and trajectory II_{opt} has relatively small performance characteristics. Trajectory IV_{opt} is a compromise between these aspects; it has relatively good performance characteristics as it achieves an average and maximum increase in warning time of a factor of approximately 20 and 30, respectively. In addition, it has a probability of 90% that a spacecraft in this trajectory detects a CME. When an additional spacecraft is considered, this probability increases to approximately 99%. Finally, as was outlined in Section IV.B, the balance between the average increase in warning time and the probability of CME detection can be shifted to satisfy a particular requirement or preference.

VI. Conclusion

In this paper, solar-sail periodic trajectories in the vicinity of the Sun-Earth SL_1 and SL_5 points have been investigated to increase the solar-storm warning time with respect to current missions at the Sun-Earth L_1 point. These periodic trajectories present a trade-off three objectives: maximising the maximum and average increase in warning time as well as minimising the average distance to the CME-axis, which increases the probability that a CME is detected. Being closer to the CME-axis means that a larger fraction of CMEs can be detected, as not all CMEs are of the same size. In this study, a mean CME size, ideal solar-sail model, and a lightness number of $\beta = 0.05$ are used to compute trajectories. The search for solar-sail periodic trajectories is initiated with a grid search and genetic algorithm to find a set of two heteroclinic connections (outward and inward) between AEPs in the vicinity of the SL_1 and SL_5 points using a piece-wise constant solar-sail control law. With this definition, the spacecraft is able to return to its initial state and the trajectory is therefore periodic. From the results, it can be concluded that the grid search provides sufficiently accurate trajectories given that the AEPs of the heteroclinic connections are known; otherwise the more effective and easy-to-implement genetic algorithm ought to be used to allow the AEPs to be variable. Two trajectories have been selected for further optimisation by defining an optimal control problem and solving it with $\mathcal{PSOPT}$. Four trajectories have been obtained by specifying the relative importance of the three objectives. These trajectories have a continuously varying sail attitude control law. Trajectory I maximises the average increase in warning time, equal to approximately a factor 28.5, which results in a spacecraft practically stationary in close proximity of an AEP furthest upstream of the CME-axis. Because of the location of the AEP, it has a probability of approximately 49% of detecting a CME. On the other hand, trajectory II minimises the average distance to the CME-axis which results in a spacecraft practically stationary in close proximity of this axis, thereby having a 100% probability of CME detection, and has an average (and maximum) increase in warning time of approximately a factor 10.5. Trajectory III was initially selected to maximise the maximum increase in warning time, which was equal to a factor 29.5. However, it was observed that this maximum increase in warning time could easily be achieved for a range of values for the other two objectives, allowing to find a trajectory that satisfies a particular requirement or preference. Trajectory III is thus a somewhat random compromise between the three objectives. The same holds for trajectory IV. Trajectory III and IV have an average increase in warning time and probability of CME detection of approximately [24.2, 72%] and [19.1, 89%], respectively. In general, a larger increase in average warning time results in a smaller probability that a CME is detected (for a maximum increase in warning time of approximately a factor 29.5). It is concluded that trajectory IV is the "most optimal" trajectory when all three objectives are taken into account.

Finally, a sensitivity analysis has been conducted to assess the effect of the solar-sail model, lightness number, and CME-model. Compared to the ideal solar-sail model, the optical solar-sail model yields a modest decrease in performance of up to 2.5%. An increase in lightness number of 0.01 yields a performance increase in the (average, maximum) increase in warning time of approximately 1% and an increase in the probability of CME detection of

approximately 8%. These magnitudes can change depending on the nature of the trajectory. In general, when the trajectory is relatively close to the Earth the performance is more sensitive to a change in lightness number than trajectories further away as the CME-axis has a steeper gradient when it approaches the Earth. The obtained trajectories show a significant improvement in solar-storm warning time over current missions at L_1. However, compared to the requirement of two to three days to fully prepare for disruption, alternative methods such as a spacecraft able to *predict* CME events at L_5 should be considered as well. Still, a spacecraft that is able to *detect* a solar storm is essential in preparing society for an event as it takes away the great uncertainty that is accompanied with prediction.

References

[1] Milan, S., et al., "KuaFu: Exploring the Sun-Earth connection," *Astronomy and Geophysics*, Vol. 53, No. 4, 2012, pp. 4.21 – 4.24. https://doi.org/10.1111/j.1468-4004.2012.53421.x.

[2] Vulpetti, G., Johnson, L., and Matloff, G., *Solar sails: A novel approach to interplanetary travel*, 2015. https://doi.org/10.1007/978-1-4939-0941-4.

[3] Eastwood, J., Hapgood, M., Biffis, E., Benedetti, D., Bisi, M., Green, L., Bentley, R., and Burnett, C., "Quantifying the Economic Value of Space Weather Forecasting for Power Grids: An Exploratory Study," *Space Weather*, 2018. https://doi.org/10.1029/2018SW002003.

[4] Homeier, N., and Wei, L., "Solar Storm Risk to the North American Electric Grid," Tech. rep., Atmospheric and Environmental Research (AER), 2013.

[5] Riley, P., "On the probability of occurrence of extreme space weather events," *Space Weather*, Vol. 10, No. 2, 2012. https://doi.org/10.1029/2011SW000734.

[6] Gibney, E., "Europe lines up for solar-storm view," *Nature*, Vol. 541, 2017, p. 271.

[7] Heiligers, J., Diedrich, B., Derbes, B., and McInnes, C., "Sunjammer: Preliminary end-to-end-mission design," *AIAA/AAS Astrodynamics Specialist Conference 2014*, American Institute of Aeronautics and Astronautics, 2014, p. 4127. https://doi.org/10.2514/6.2014-4127.

[8] McInnes, C., *Solar sailing: Technology, Dynamics and Mission Applications*, Springer-Praxis Books in Astronautical Engineering, Springer-Verlag, Berlin, 1999.

[9] Martínez, G., "Solar-sail surfing along invariant manifolds to increase the warning time for solar storms," Master's thesis, 2020. Delft University of Technology.

[10] Tsuda, Y., et al., "Achievement of IKAROS-Japanese deep space solar sail demonstration mission," *Acta Astronautica*, 2013. https://doi.org/10.1016/j.actaastro.2012.03.032.

[11] Johnson, L., Whorton, M., Heaton, A., Pinson, R., Laue, G., and Adams, C., "NanoSail-D: A solar sail demonstration mission," *Acta Astronautica*, 2011. https://doi.org/10.1016/j.actaastro.2010.02.008.

[12] Betts, B., et al., "LightSail 2: Controlled solar sail propulsion using a CubeSat," *Proceedings of the International Astronautical Congress, IAC*, 2019.

[13] McNutt, L., Johnson, L., Clardy, D., Castillo-Rogez, J., Frick, A., and Jones, L., "Near-Earth Asteroid (NEA) Scout," *AIAA SPACE 2014 Conference and Exposition*, 2014.

[14] Mori, O., et al., "Solar power sail mission of OKEANOS," *Astrodynamics*, Vol. 4, 2020, pp. 233 – 248. https://doi.org/10.1007/s42064-019-0067-8.

[15] Heiligers, J., and McInnes, C., "Novel solar sail mission concepts for Space weather forecasting," 2014.

[16] Barnhart, D., Vladimirova, T., and Sweeting, M., "Very-Small-Satellite Design for Distributed Space Missions," *Journal of Spacecraft and Rockets*, Vol. 44, No. 6, 2007, pp. 1294 – 1306. https://doi.org/10.2514/1.28678.

[17] Isavnin, A., "FRiED: A NOVEL THREE-DIMENSIONAL MODEL OF CORONAL MASS EJECTIONS," *The Astrophysical Journal*, Vol. 833, No. 2, 2016, pp. 267 – 276. https://doi.org/10.3847/1538-4357/833/2/267.

[18] Becerra, V., "Solving complex optimal control problems at no cost with PSOPT," *Proceedings of the IEEE International Symposium on Computer-Aided Control System Design*, 2010, pp. 1391–1396. https://doi.org/10.1109/CACSD.2010.5612676.

[19] Heiligers, J., Fernandez, J., Stohlman, O., and Wilkie, K., "Trajectory design for a solar-sail mission to asteroid 2016 HO3," *Astrodynamics*, Vol. 3, No. 3, 2019, pp. 231–246. https://doi.org/10.1007/s42064-019-0061-1.

[20] Spencer, H., and Carroll, K., *Real Solar Sails are Not Ideal, and Yes It Matters*, Springer Berlin Heidelberg, Berlin, Heidelberg, 2014, pp. 921–940. https://doi.org/10.1007/978-3-642-34907-2_55.

[21] McInnes, A., "Strategies for solar sail mission design in the circular restricted three-body problem," Master's thesis, August 2000. Purdue University.

[22] Dachwald, B., Mengali, G., Quarta, A., and Macdonald, M., "Parametric model and optimal control of solar sails with optical degradation," *Journal of Guidance, Control and Dynamics*, Vol. 29, No. 5, 2006, pp. 1170–1178.

[23] Heaton, A., Ahmad, N., and Miller, K., "Near Earth Asteroid Scout Thrust and Torque Model," 2017.

[24] Farrés, A., "Catalogue on the dynamics of a solar sail around L_1 and L_2," *Proceedings of the 4th International Symposium on Solar Sailing*, 2017.

[25] Richardson, I., and Cane, H., "Near-Earth Interplanetary Coronal Mass Ejections During Solar Cycle 23 (1996 - 2009): Catalog and Summary of Properties," *Solar Physics*, Vol. 264, No. 1, 2010, pp. 189–237. https://doi.org/10.1007/s11207-010-9568-6.

[26] Turner, D., and Li, X., "Using spacecraft measurements ahead of Earth in the Parker spiral to improve terrestrial space weather forecasts," *Space Weather*, Vol. 9, No. 1, 2011. https://doi.org/10.1029/2010SW000627.

[27] Farrés, A., and Jorba, A., "Solar sailing with invariant manifolds in the earth-sun system," *Proceedings of the International Astronautical Congress, IAC*, Vol. 7, No. April, 2015, pp. 5323–5333.

[28] Vergaaij, M., and Heiligers, J., "Time-optimal solar sail heteroclinic-like connections for an Earth-Mars cycler," *Acta Astronautica*, Vol. 152, 2018, pp. 474–485. https://doi.org/10.1016/j.actaastro.2018.08.008.

[29] Farrés, A., Heiligers, J., and Miguel, N., "Road map to L4/L5 with a solar sail," *Aerospace Science and Technology*, 2019. https://doi.org/10.1016/j.ast.2019.105458.

[30] "MATLAB 1-D data interpolation," , 2021. Date Accessed: 16-06-2021. URL https://nl.mathworks.com/help/matlab/ref/interp1.html#btwp6lt-1-method.

[31] Wilkie, W., Personal Communication, May 2021. NASA Langley Research Center.

[32] Spencer, D., Johnson, L., and Long, A., "Solar sailing technology challenges," *Aerospace Science and Technology*, Vol. 93, 2019, p. 105276. https://doi.org/10.1016/j.ast.2019.07.009.

[33] Young, R., "Updated Heliostorm Warning Mission: Enhancements Based on New Technology," 2007. https://doi.org/10.2514/6.2007-2249.

[34] "The "no name" space weather mission," , 2017. Date Accessed: 04-06-2021. URL https://www.esa.int/Safety_Security/The_no_name_space_weather_mission.

3

Conclusion & Recommendations

This thesis work investigated periodic solar-sail trajectories to increase the solar-storm warning time with respect to current missions at the Sun-Earth L_1 point. In addition, the thesis provided insights into the problem characteristics to build on the current body of knowledge of using solar-sail dynamics in the field of solar-storm detection. This chapter displays the conclusion of the thesis report in Sec. 3.1, which is based on answering the research questions that were posed in Sec. 1.3. After that, recommendations for further study are laid out in Sec. 3.2.

3.1. Conclusion

The conclusion of the thesis work is divided into separate answers to the research questions that were outlined in Sec. 1.3. After the individual answers, this section will reflect on the thesis work with regards to the need for an increase in solar-storm warning time.

A) *How can heteroclinic(-like) connections between artificial equilibrium points in the vicinity of the SL_1 and SL_5 point be used to generate a periodic solar-sail trajectory that travels upstream of the CME-axis using a piecewise-constant sail attitude?*

A periodic solar-sail trajectory is obtained using two heteroclinic connections. The first heteroclinic connection allows the spacecraft to travel upstream of the CME-axis, while the second heteroclinic connection lets the spacecraft travel back to the AEP from which the first heteroclinic connection initiated. As a result, the mission lifetime is only limited by the lifetime of the spacecraft and the solar sail. The periodic solar-sail trajectories utilise a piece-wise constant steering law, which is obtained by a genetic algorithm. Despite the genetic algorithm being a robust and easy-to-implement method, it can be concluded that a grid search is more effective and ensures sufficiently accurate trajectories are obtained if the boundary conditions of the heteroclinic connections (i.e., the set of two AEPs) is known. This set of AEPs can be obtained relatively easily through first-order computations. Two periodic solar-sail trajectories are generated. The first, N_1, is aimed at maximising the *maximum* increase in warning time, equal to approximately a factor 45 compared to current missions at the L_1 point, while the second, N_2, has the goal to maximise the *average* increase in warning time, equal to approximately a factor 21. Trajectory N_1 does not spend all of its time in the CME detection zone, which means seven spacecraft are required to maintain continuous CME monitoring, as opposed to trajectory N_2 that requires only one spacecraft. The main downside of obtaining periodic solar-sail trajectories using the method outlined here is the fact that the sail attitude is constant throughout each manifold, which renders it sub-optimal. In addition, the trajectories are practically infeasible as there is a discontinuity in the state and control at the linkages of the unstable and stable manifolds. Still, these trajectories act as a good initial guess for the optimal control problem.

B) *Can the piecewise-constant sail attitude profile be optimised to a continuously varying sail attitude profile to improve the performance of the periodic solar-sail trajectories?*

The performance of a periodic solar-sail trajectory is quantified by three objectives: the average and maximum increase in warning time and the average distance to the CME-axis. Minimisation of the last objective increases the probability of detection, taking into consideration the variations in CME shape. Defining the search for a periodic solar-sail trajectory with the aim of increasing the solar-storm warning time as an optimal control problem relieves the limitations that correspond to the use of heteroclinic connections. This is because the solution to the optimal control problem has no discontinuity in the state or control and the sail attitude is allowed to vary continuously. Additionally, the boundary conditions are fixed. In the optimal control problem this constraint is relaxed, potentially leading to a 'more optimal' trajectory as the search space is enlarged. The optimal control problem is solved in $\mathcal{PSOPT}$, a particular implementation of a direct pseudospectral method. An additional constraint has been added to the search space to be able to properly compare the results: the spacecraft should always remain in the CME detection zone such that only one spacecraft is required to maintain continuous CME monitoring. By specifying the relative importance of each objective, in the end, four trajectories have been obtained. These trajectories are outlined below and their properties are summarised in Table. 3.1.

- Trajectory I maximises the average increase in warning time, equal to approximately a factor 28.5, which results in a trajectory practically stationary in close proximity of the AEP on the border of the CME detection zone located furthest upstream of the CME-axis. A spacecraft in this trajectory achieves a maximum increase in warning time and a probability of CME detection of 28.5 and 49%, respectively.
- Trajectory II minimises the distance to the CME-axis, leading to a practically stationary trajectory in close proximity of the AEP that is on the CME-axis. Because of this location, it has an average and maximum increase in warning time of approximately a factor 10.5 and a spacecraft in this trajectory has a probability of 100% of detecting a CME.
- Trajectory III was initially selected to maximise the maximum increase in warning time, but it was observed that approximately a factor of 29.5 could easily be obtained for a range of values for the other two objectives. As a result, trajectory III is a somewhat random compromise between the three objectives. The same holds for trajectory IV. Trajectories III and IV achieve an average and maximum increase in warning time of approximately a factor [24.2, 29.5] and [19.1, 29.1], respectively. In addition, spacecraft in these trajectories have a probability of CME detection of 72% and 89%, respectively. These trajectories are multi-revolutionary where one revolution is attributed to achieving the maximum increase in warning time, while the others are in place to balance the average increase in warning time and the average distance to the CME-axis (i.e., probability of CME detection).

From these trajectories, it is observed that a larger average increase in warning time results in a smaller probability of CME detection, and the balance between them can be shifted to satisfy a specific requirement or preference (while the maximum increase in warning time is not impacted). All in all, it can be said that the performance of the optimised trajectories is improved over the piecewise-constant trajectories, not necessarily in the three objectives but the trajectories are more realistic and therefore more relevant.

Table 3.1: Overview of the properties of trajectories I-IV.

Trajectory	k_{avg}, -	k_{max}, -	P_{total}, %	T, yr
I: max(k_{avg})	28.48	28.51	48.73	1.60
II: min(d_{avg})	10.51	10.53	100.0	4.64
III: max(k_{max})	24.22	29.46	72.22	2.76
IV: Compromise	19.09	29.17	89.12	4.69

C) *What is the effect of including optical imperfections in the solar-sail model on the performance of the solar-storm detection trajectories?*

Instead of utilising an ideal solar-sail model, an optical sail model has been employed to assess the impact on the performance. While the ideal solar-sail model assumes pure specular

reflection of the incident photons, the optical sail model accounts for absorption, diffuse reflection, and thermal emission. These effects introduce a tangent solar-sail acceleration component as well as a smaller normal solar-sail acceleration, which becomes smaller for a larger solar-sail pitch angle, i.e., a larger difference with respect to the ideal solar-sail model. The impact of the model implementation on the performance of trajectories I - IV is at most a modest 2.5%, i.e., a decrease in average and maximum warning time and probability of CME detection. This small impact may be attributed to the small magnitude of the solar-sail pitch angle in the control profile of the trajectories (with a maximum of $\alpha = \pm 18$ deg). As the solar-sail pitch angle remains small, the difference between the two solar-sail models will also remain small.

D) *What is the effect of the current state-of-the-art and mid- to far-term advances in solar-sail technology on the performance of the solar-storm detection trajectories?*

The trajectories in this thesis work have been computed using a lightness number of $\beta = 0.05$, which is in accordance with expected mid-term technological advances. Current state-of-the-art achieves a lightness number of $\beta = 0.01$, while a lightness number of $\beta = 0.1$ is expected in the mid- to far-term future. Therefore, trajectories I - IV have been recomputed using a lightness number in the range of $\beta \in [0.01, 0.1]$. The performance increases proportionally to an increase in lightness number. In particular, it is observed that, in general, an increase in lightness number of 0.01 yields an increase in average and maximum warning time of 1% and an increase in the probability of CME detection of 8%. The magnitude of the increase depends on the nature of the trajectories: a trajectory relatively close to the Earth is more sensitive to a change in lightness number than a trajectory that is further away. This observation may be attributed to the steeper gradient of the CME-axis as it approaches the Earth.

The answers to the research questions show that periodic solar-sail trajectories exist which exhibit an average and maximum increase in solar-storm warning time of approximately a factor 20 to 30 with respect to current missions at L_1. These missions at L_1 have a warning time of 30 to 60 minutes, meaning that the solar-sail propelled trajectories presented in this thesis work can obtain an absolute warning time of 10 to 30 hours. As it is estimated that two to three days are required to prepare for disruption, other methods should be considered to become aware of an approaching solar storm in a timely manner. In particular, a spacecraft stationed at L_5 could provide predictions up to five days. However, due to the great uncertainty of the path and magnitude of the CME that is associated with prediction, a supporting spacecraft is required to gain an accurate insight of a potentially approaching solar storm. For this, an in-situ solar-sail spacecraft may be a good solution. A storm can be predicted by a spacecraft at L_5, from which precautions on Earth may be set in place to reduce the preparation time, and when the solar-sail spacecraft in one of the trajectories presented in this thesis work does detect an approaching solar-storm, the 'real' preparation on Earth can be initiated. Therefore, it is believed that a combination of a spacecraft at L_5 and a solar-sail spacecraft in a periodic solar-sail trajectory presented in this thesis work may be the solution to receive an appropriate warning signal of an approaching solar storm.

3.2. Recommendations

This section outlines numerous recommendations for future work in the area of using solar-sail dynamics in the field of solar-storm detection. The recommendations are divided into three categories to provide a clear overview and can be seen below.

Changes to the (dynamical) model:

- *Implement a three-dimensional dynamical model.*
  This thesis work employed a two-dimensional dynamical model, as a CME headed towards Earth shows a clear correlation between its path and the ecliptic plane. This yields the analysis in a two-dimensional formulation most insightful. In reality, a CME is a three-dimensional structure. Evaluating the motion in three dimensions may result in a 'more optimal' trajectory if, for instance, the solar-sail spacecraft is able to spend a larger fraction of its time upstream of the CME propagation path or closer to the CME-axis compared to the two-dimensional formulation. If a two-dimensional trajectory would be the 'most optimal', the three-dimensional formulation will output

such a trajectory.

- *Implement the elliptical restricted three-body problem (ERTBP).*
  A circular restricted three-body problem (CRTBP) is employed in this thesis work, which assumes, among others, circular motion of the two primaries about the barycenter of the system. The ERTBP accounts for the eccentricity of the two primaries about the barycenter. In reality, the motion of the Sun around the Earth is also elliptical, which means that the implementation of an ERTBP is a more realistic representation of the real problem.

- *Evaluate the fourth-body perturbation of Venus*
  The trajectories that are obtained in this thesis work travel upstream to about 0.88 Astronomical Unit (AU). As Venus orbits the Sun at approximately 0.72 AU, the gravitational influence of Venus on the solar-sail spacecraft may play a role in the real dynamics. It is therefore recommended to implement the gravitational field of Venus as a fourth-body perturbation.

- *Implement a variable velocity profile in the CME model.*
  The CME model in this thesis work implicitly assumes a constant velocity of the CME that is on a trajectory to intersect the Earth: the increase in warning time is determined as the fraction of the CME-axis arc length and the distance between Earth and L_1. However, literature displays a variable velocity profile of the CME propagation path, where the CME travels faster through interplanetary space compared to when it arrives at the Earth. Incorporating this feature yields a more accurate representation of the achievable increase in warning time of a solar-sail spacecraft.

Sensitivity analyses:

- *Evaluate the consequences of the heat flux on the solar sail.*
  As the solar-sail spacecraft is designed to travel further upstream of the CME-axis, i.e., closer to the Sun, the consequences due to the heat flux become more dominant compared to, for instance, a solar-sail spacecraft in low-Earth orbit. It should be ensured that the solar sail is able to handle resulting temperatures and (heat) stresses.

- *Expand the optical solar-sail model coefficient set uncertainty analysis.*
  The uncertainty in the optical solar-sail model coefficient set has been assessed by evaluating two situations: the lower bound of all coefficients and the upper bound of all coefficients. However, the greatest deviation from an ideal solar-sail model is not necessarily achieved with either all coefficients equal to the lower or upper bound. For instance, by looking at the second term of the normal solar-sail acceleration component, a_n; $B_f(1-s)\tilde{r}\cos\alpha$, it is observed that the largest value is achieved by the upper bound of r and B_f and the lower bound of s. Therefore, the uncertainty analysis of the optical solar-sail model coefficient set should be expanded such that multiple combinations of the coefficient values are evaluated.

- *Evaluate a variation in the CME-axis.*
  In the sensitivity analysis of the thesis work, the CME size has been changed to assess the impact of a smaller/larger storm on the performance of trajectories I - IV. However, it was assumed that the CME-axis remains constant for all CMEs approaching the Earth. In reality, this may not be the case. This variation should therefore be taken into account with regards to the assessment of the trajectory performance. A good starting point would be to analyse the data of previously detected CMEs to deduce a trend in CME-axis variation.

Additional work:

- *Generate periodic solar-sail trajectories that require multiple spacecraft to maintain continuous CME monitoring.*
  This thesis work included a constraint in the optimisation problem which states that the trajectory has to remain in the CME detection zone at all times, thereby only requiring one spacecraft to maintain continuous CME monitoring. However, it is interesting to assess the performance with regards to solar-storm detection if two or more solar-sail spacecraft are available. As a result, the trajectory does not have to remain in the CME detection zone at all times, as only one of the spacecraft has to be in the zone, thereby possibly increasing the performance of the overall

mission. The initial guess generation displayed that a maximum increase in warning time of approximately a factor 45 is achievable. Seven solar-sail spacecraft should be equally spaced in time throughout this trajectory to maintain continuous CME monitoring. Furthermore, note that the multiple solar-sail spacecraft do not necessarily have to be in the same trajectory, which makes the mission design of a constellation of solar-sail spacecraft even more flexible.

- *Evaluate if/what type of shielding is required to withstand the surpassing of a CME.*
  A CME is a large cloud of plasma containing its own magnetic field. Because of that, it may interact with the solar-sail spacecraft: it could be the case that the CME magnetic field causes the spacecraft electronic systems to malfunction. Furthermore, the plasma cloud may damage the solar sail. Sufficient shielding should be in place such that it is guaranteed the spacecraft withstands the surpassing of a CME. Currently, spacecraft that have the purpose to detect solar storms exist, such as SOHO, ACE, WIND, and DSCOVR, and therefore it may be assumed that appropriate shielding is available to protect the spacecraft. However, these spacecraft do not have a solar sail, meaning that this aspect should be evaluated before the launch of an actual solar-sail spacecraft for the purpose of solar-storm detection. Note that the shielding may add to the spacecraft mass, which reduces the lightness number of the solar-sail spacecraft, ultimately reducing the performance of the mission (according to the answer of research question D).

A

Verification & Validation

This appendix chapter will focus on the verification and validation of the models and numerical techniques that are used to obtain the periodic solar-sail trajectories presented in this thesis work. At first, the models are verified and validated in Sec. A.1 followed by Sec. A.2 that addresses the numerical techniques.

A.1. Models

This section displays the verification of the dynamical model and the solar-sail models that have been used throughout the journal article.

A.1.1. Dynamical model

First of all, it should be noted that the Circular Restricted Three-Body Problem (CRTBP) is widely used in astrodynamics problems, such as in Ref. [21], and also in solar-sail related problems, such as in Ref. [9, 22]. This means that the CRTBP can be considered validated.

Firstly, the implementation of the CRTBP with an ideal solar-sail acceleration is verified by retrieving the location of the SL_1 point as well as the eigenvalues as a function of the solar-sail lightness number, β. These results are compared to literature, in particular Table 2 from Ref. [22], and can be seen in Table A.1. It is observed that the values correspond to each other. Furthermore, manifold-like trajectories are obtained from the SL_1 point as a function of the solar-sail pitch angle, α, and compared to literature. This has been done by propagating the initial conditions (at the SL_1 point) in the unstable direction and simultaneously changing the solar-sail pitch angle. Figure 3 from Ref. [22] has been reproduced and can be seen in Fig. A.1, where it can be seen that the manifolds correspond to each other. Finally, the surfaces of AEPs as a function of lightness number in the vicinity of the L_1, L_2, and L_5 points have been computed and compared to Fig. 3 and Fig. 4 from Ref. [23] and can be seen in Fig. A.2. From inspection, it can be seen that the surfaces of AEPs match the results from Fig. 3 and Fig. 4 from Ref. [23].

As the three computed results comply with literature, it can be concluded that the CRTBP with an ideal solar-sail acceleration is correctly implemented, i.e., verified.

Table A.1: Comparison of the location of the SL_1 point and its eigenvalues between Ref. [23] and the thesis *MATLAB* script.

β	Table 2 from Ref. [22]			Thesis *MATLAB* script		
	x_{L_1}	λ_1	λ_2	x_{L_1}	λ_1	λ_2
0.01	0.98873	2.1399	1.8517	0.98873	2.1399	1.8517
0.02	0.98717	1.7820	1.6484	0.98717	1.7820	1.6484
0.03	0.98525	1.4696	1.4821	0.98525	1.4696	1.4821
0.04	0.98299	1.2088	1.3536	0.98299	1.2088	1.3536
0.05	0.98041	0.9983	1.2586	0.98041	0.9983	1.2586

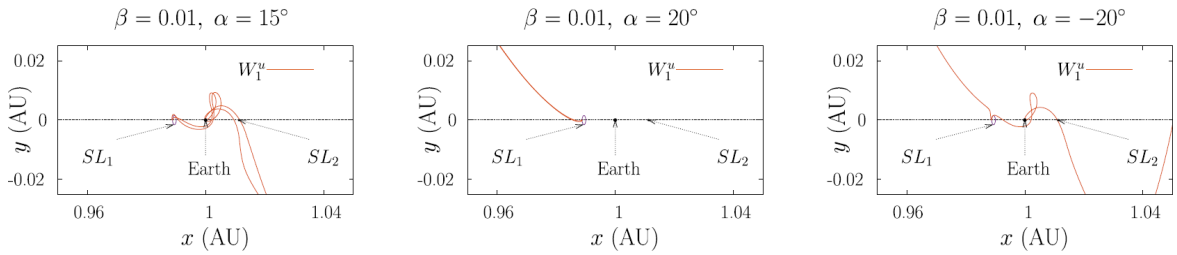

(a) Figure 3 from Ref. [22].

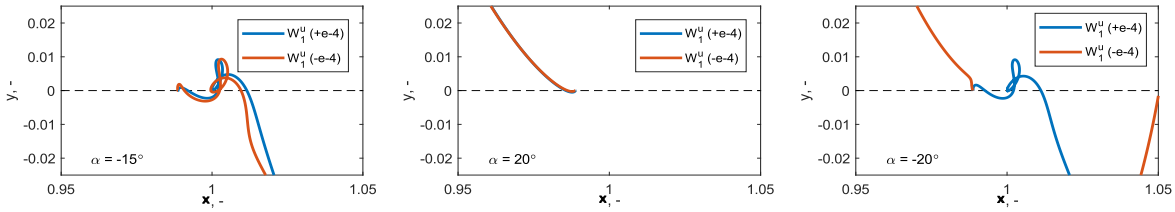

(b) Reproduction using the thesis *MATLAB* code.

Figure A.1: Comparison of the propagation of the initial conditions at the SL_1 point in the unstable direction while simultaneously changing the solar-sail pitch angle between Ref. [22] and the thesis *MATLAB* code.

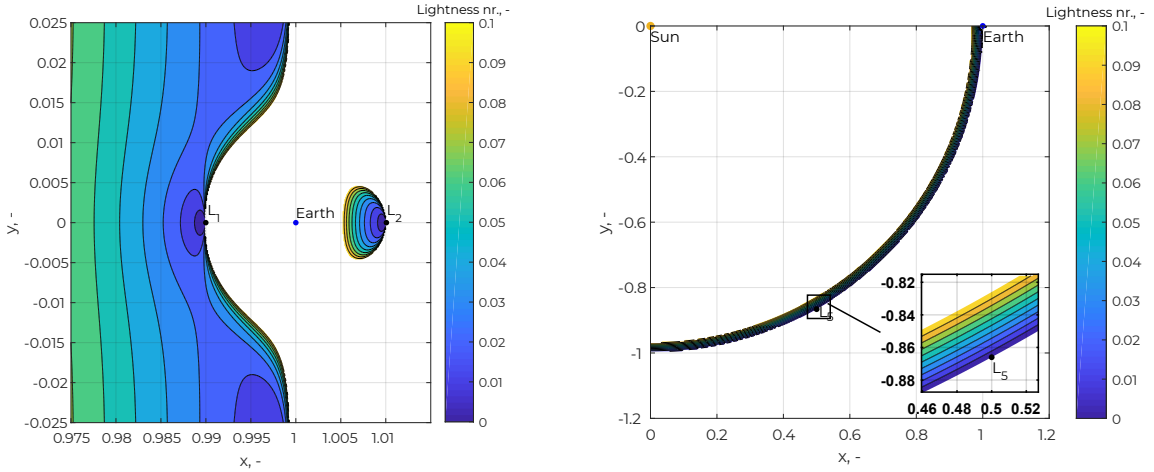

(a) The vicinity of the L_1 and the L_2 point.

(b) The vicinity of the L_5 point.

Figure A.2: Surfaces of Artificial Equilibrium Points (AEPs) in the vicinity of the Sun-Earth L_1, L_2, and L_5 point as a function of lightness number ($\beta \in [0, 0.1]$).

A.1.2. Solar-sail models

Throughout the thesis, use has been made of an ideal and optical solar-sail model. The previous subsection verified the ideal solar-sail model, whereas the optical sail model will be verified here. This will be done by computing the (ideal and) optical solar-sail model acceleration with the coefficient set that is presented in Ref. [10] and given in Table. A.2. The solar-sail acceleration for both an optical and ideal solar-sail model is computed as a function of the pitch angle and presented in Fig. A.3. The plot that is presented in Ref. [10] is also given for comparison purposes. It can be seen that the reproduced solar-sail acceleration matches with the plot from Ref. [10], and therefore it can be said that the implementation of the optical solar-sail model in the thesis *MATLAB* code is verified.

Table A.2: The optical solar-sail model coefficient set retrieved from Ref. [10].

Coefficient	$\tilde{r}$, -	s, -	B_f, -	B_b, -	e_f, -	e_b, -
Value	0.88	0.94	0.79	0.55	0.05	0.55

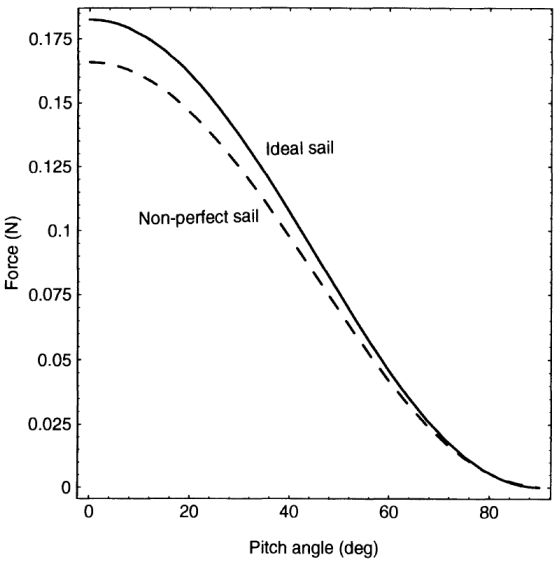

(a) Figure 2.9 from Ref. [10].

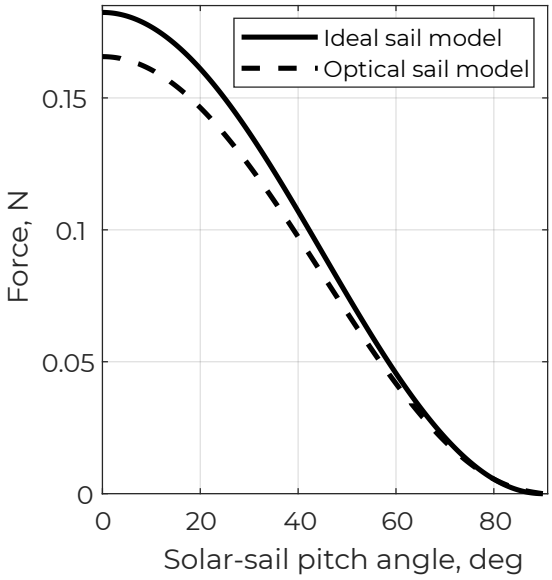

(b) Reproduction using the thesis *MATLAB* code.

Figure A.3: Comparison of solar-sail acceleration using the optical solar-sail model as a function of the pitch angle between Ref. [10] and the thesis *MATLAB* code. The coefficient set presented in Table. A.2 is used in the optical sail model.

A.2. Numerical Techniques

Two numerical techniques are utilised throughout the journal article that require verification and validation: the genetic algorithm and the optimisation algorithm $\mathcal{PSOPT}$, which is a direct pseudospectral method [20]. The verification and validation methods will be displayed in this section.

A.2.1. Genetic Algorithm

The *MATLAB* implementation of the Genetic Algorithm (GA), *ga.m*, is used. As it is a function that is provided by *MATLAB*, it may be assumed that the algorithm itself is verified [24].

Still, there are two aspects that require verification of the GA. The first aspect governs the question whether a GA is a suitable algorithm to find the desired trajectories and the second aspect contains the consideration whether the problem at hand is correctly implemented.

Regarding the first aspect, previous research has indicated that a GA can generate sufficiently accurate and representative trajectories, i.e., the GA is able to converge to a global optimum solution in the search space [17, 25]. In addition to that, the GA has been executed several times using seeds $[0, 1, 2, 3, 4]$ and it is checked whether the GA converges to (approximately) the same solution. It was observed that it was indeed the case, so it can be claimed with confidence that the GA is a capable enough algorithm for the problem at hand.

It is already known from Subsec. A.1.1 that the dynamical model used by the GA is verified. So, the only thing that requires verification is the implementation of the objective function. For this, the results of the GA are compared to the results from the grid search (outlined in in the journal article). It is observed that the results correspond to the hypotheses that were specified in the grid search. For example, for minimisation of J_1 (defined in the journal article), i.e., maximisation of the maximum increase in warning time, the GA returns a trajectory that takes $[p_1, p_2]$ as $[SL_1, P_1]$ with approximately the same solar-sail pitch angle values along each of the unstable and stable manifolds as resulted from the grid search.

As the GA performs as expected in the two aspects, it can be said that the GA is verified.

A.2.2. PSOPT

$\mathcal{PSOPT}$ should be verified and validated in three aspects. The first aspect regards the question whether $\mathcal{PSOPT}$ is able to converge to the global optimum solution within the search space, the second aspect concerns the correct implementation of the optimisation problem in $\mathcal{PSOPT}$, and the third aspect con-

tains the question whether the solution provided by $\mathcal{PSOPT}$ is a valid solution (which will be elaborated upon below).

Regarding the first aspect, there have been numerous published research articles that use $\mathcal{PSOPT}$ as the algorithm to solve a solar-sail optimal control problem, such as Ref. [25, 26]. Moreover, these articles use approximately the same dynamical model as the one used in this research, i.e., a restricted three-body problem with a solar-sail acceleration. Based on these observations, it can be said with confidence that $\mathcal{PSOPT}$ is qualified and able to find the global optimum solution for the problem at hand [20].

Now that it is known that $\mathcal{PSOPT}$ can be used to find the optimum, it should be verified whether the problem at hand is correctly implemented in $\mathcal{PSOPT}$. At first, the implementation of the dynamical model is checked by substituting an optimisation problem into the code for which the solution is known. In particular, a time-optimal trajectory from the SL_1 point towards the Region of Practical Stability (RPS) in the vicinity of the SL_5 point is computed and compared to the results from Ref. [22]. Note that the dynamical model is the same as the model that is used throughout the thesis. The initial guess is selected to be a heteroclinic connection from the SL_1 point to the SL_5 point, which is obtained during the initial guess generation of the thesis (displayed in the journal article). The positional state and the control profile of the initial guess and the optimised trajectory can be seen in Fig. A.4. In addition, the comparison with the result obtained in Ref. [22] can be seen in Table A.3. There is a modest difference in optimised transfer times, equal to 3.3%, which may be attributed to the large difference in initial guess. Since the difference in transfer time is small, it can be said that the dynamical model is correctly implemented in $\mathcal{PSOPT}$.

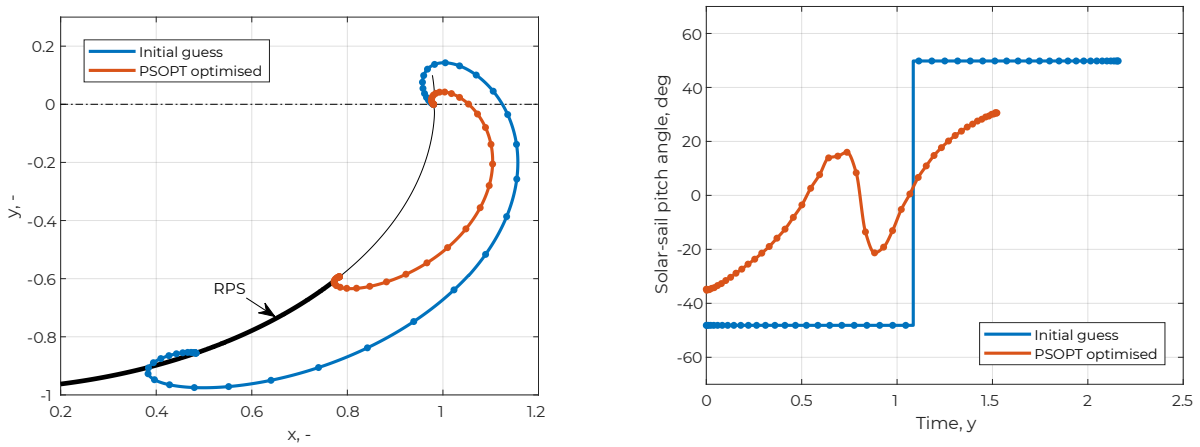

(a) Positional state of the initial guess and optimised solution.

(b) Control profile as a function of time of the initial guess and optimised solution.

Figure A.4: Overview of the initial guess and optimised solution of a time-optimal trajectory from SL_1 to the Region of Practical Stability (RPS) in the vicinity of the SL_5 point.

Table A.3: Comparison of the transfer times of the initial guess and optimised trajectory from SL_1 to the Region of Practical Stability (RPS) in the vicinity of the SL_5 point between Ref. [22] and the results from the thesis code.

$SL_1 \rightarrow$ RPS SL_5	Initial guess	Optimised	ΔOptimised
From Ref. [22]	563 days	538 days	3.3%
Thesis code	789 days	556 days	

Besides the dynamical model verification, it should be checked whether the objective function is correctly implemented. This can be done by performing optimisation runs for which the solution is known. The first run concerns solely optimising for the average increase in warning time. During the initial guess generation, it was hypothesised that the optimisation algorithm should return a trajectory that is stationary in close proximity of an AEP which is furthest upstream of the CME-axis, while remaining in the CME detection zone. The results of this optimisation run, using initial guess trajectories

N_1 and N_2 (outlined in the journal article), is presented in Fig. A.5. As can be seen, the optimisation run matches the hypothesis regardless of the selected initial guess. In addition, an optimisation run has been performed to solely minimise the average distance to the CME-axis. The returned solution is a trajectory that is stationary in close proximity of an AEP on the CME-axis, which is in accordance with the hypothesis. These two computations show that the objective function is correctly implemented, and therefore it can be said that the implementation of the problem in $\mathcal{PSOPT}$ is verified.

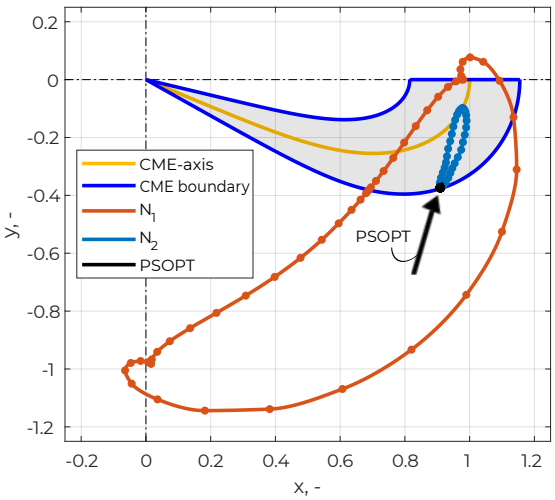

(a) Positional state of the initial guess and optimised solution.

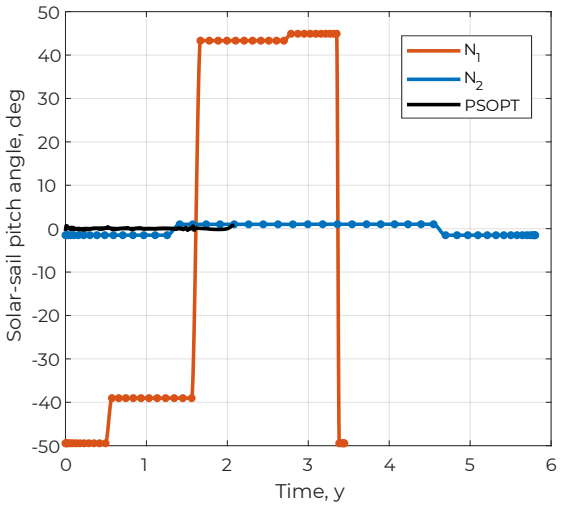

(b) Control profile as a function of time of the initial guess and optimised solution.

Figure A.5: Overview of the initial guess and optimised solution for a trajectory that maximises the average increase in warning time. Note that both N_1 and N_2 have been used as an initial guess.

Finally, the third aspect governs the question whether the solution provided by $\mathcal{PSOPT}$ is a valid solution. This should be validated as $\mathcal{PSOPT}$ only guarantees a valid solution *at* the Legendre-Gauss-Lobatto nodes, and not in-between the nodes [20]. If this is not checked, it could result in a trajectory where the path or boundary constraints are violated in-between the nodes. Validation of the $\mathcal{PSOPT}$ solution is done by fully re-integrating the solution in *MATLAB*. Full re-integration takes the initial conditions from $\mathcal{PSOPT}$ and integrates the state until the final time. The control, i.e., the solar-sail pitch angle, is interpolated from the $\mathcal{PSOPT}$ solution using shape-preserving piecewise cubic interpolation. From inspection it is observed that the re-integrated solution does not violate any constraints of the optimisation problem, and therefore it can be said that the $\mathcal{PSOPT}$ solution is a valid solution.

B

Supporting Computations

In the journal article, initial guess trajectories have been obtained that assume a constant hyper-plane, $\sum$, at the mid-distance between p_1 and p_2 (the AEPs from which heteroclinic connections are realised). The assumption that a constant hyper-plane may be assumed will be justified here.

The genetic algorithm that was laid out in the journal article has been executed using a constant and variable hyper-plane for several combinations of p_1 and p_2. Note that in these computations p_1 and p_2 are kept fixed to allow for a proper comparison. Furthermore, the objective function that was used in these computations is J_1, i.e., maximisation of the maximum increase in warning time. The combinations $[p_1, p_2] = [SL_1, SL_5]$ and $[SL_1, P_1]$ are presented in Fig. B.1. It can be seen that the constant and variable hyper-plane computations return practically the same trajectory. In addition, it was seen that the variable hyper-plane computation returns a location of the hyper-plane at approximately the same location as the constant hyper-plane computation. While the variable hyper-plane computation takes significantly longer to converge to its solution as the variable hyper-plane adds another dimension to the design space, the constant hyper-plane computation is far more efficient and is able to generate practically the same trajectories. Therefore, this assumption is employed in the search for initial-guess trajectories.

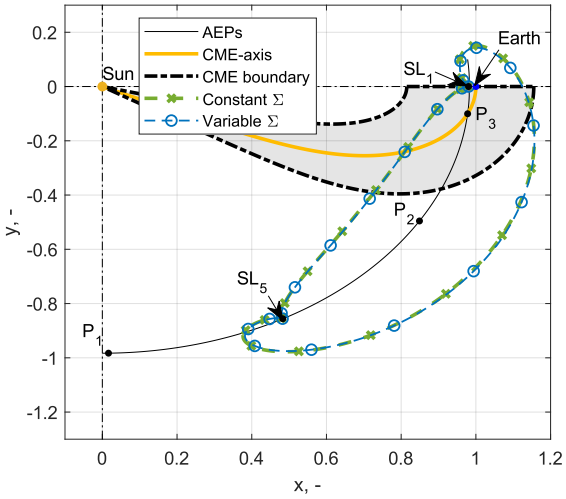

(a) Trajectories between SL_1 and SL_5.

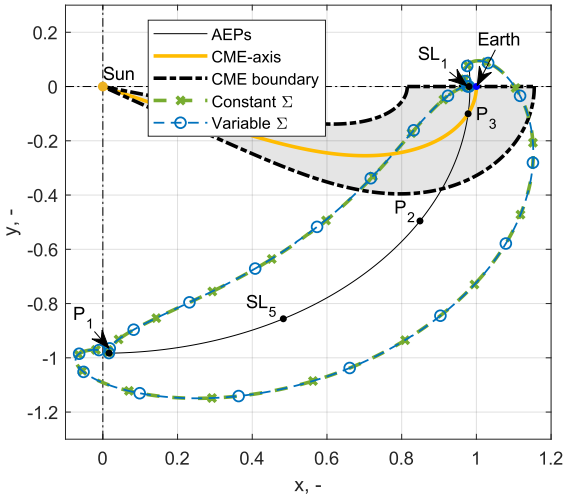

(b) Trajectories between SL_1 and P_1.

Figure B.1: A comparison between genetic algorithm computations that utilise a constant and variable hyper-plane assumption. The set of AEPs are kept fixed to properly compare the results.

Bibliography

[1] R. Schwenn, “Space Weather: The Solar Perspective,” *Living Reviews in Solar Physics*, 2006.

[2] S. Milan, M. Dunlop, A. Fazakerley, B. Hubert, B. Lavraud, N. Østgaard, J. Shi, C. Escoubet, M. Taylor, P. Falkner, and A. Wielders, “KuaFu: Exploring the Sun-Earth connection,” *Astronomy and Geophysics*, 2012.

[3] A. Benz, “Flare Observations,” *Living Reviews in Solar Physics*, 2017.

[4] G. Vulpetti, L. Johnson, and G. Matloff, *Solar sails: A novel approach to interplanetary travel*, 2015.

[5] P. Cannon, *Extreme space weather: impacts on engineered systems and infrastructures*, 2013.

[6] P. Riley, “On the probability of occurrence of extreme space weather events,” *Space Weather*, 2012.

[7] J. P. Eastwood, M. A. Hapgood, E. Biffis, D. Benedetti, M. M. Bisi, L. Green, R. D. Bentley, and C. Burnett, “Quantifying the Economic Value of Space Weather Forecasting for Power Grids: An Exploratory Study,” *Space Weather*, 2018.

[8] N. Homeier and L. Wei, “Solar Storm Risk to the North American Electric Grid,” Atmospheric and Environmental Research (AER), Tech. Rep., 2013. [Online]. Available: https://www.lloyds.com/news-and-risk-insight/risk-reports/library/natural-environment/solar-storm

[9] J. Heiligers, B. Diedrich, B. Derbes, and C. McInnes, “Sunjammer: Preliminary end-to-end-mission design,” in *AIAA/AAS Astrodynamics Specialist Conference 2014*. American Institute of Aeronautics and Astronautics, 2014, p. 4127.

[10] C. McInnes, *Solar sailing: Technology, Dynamics and Mission Applications*. Berlin: Springer-Praxis Books in Astronautical Engineering, Springer-Verlag, 1999.

[11] E. Gibney, “Europe lines up for solar-storm view,” *Nature*, vol. 541, p. 271, 2017.

[12] Y. Tsuda *et al.*, “Achievement of IKAROS-Japanese deep space solar sail demonstration mission,” in *Acta Astronautica*, 2013.

[13] L. Johnson, M. Whorton, A. Heaton, R. Pinson, G. Laue, and C. Adams, “NanoSail-D: A solar sail demonstration mission,” in *Acta Astronautica*, 2011.

[14] B. Betts *et al.*, “LightSail 2: Controlled solar sail propulsion using a CubeSat,” in *Proceedings of the International Astronautical Congress, IAC*, 2019.

[15] L. McNutt, L. Johnson, D. Clardy, J. Castillo-Rogez, A. Frick, and L. Jones, “Near-Earth Asteroid (NEA) Scout,” in *AIAA SPACE 2014 Conference and Exposition*, 2014.

[16] O. Mori *et al.*, “Solar power sail mission of OKEANOS,” *Astrodynamics*, vol. 4, pp. 233 – 248, 2020.

[17] G. Martínez, “Solar-sail surfing along invariant manifolds to increase the warning time for solar storms,” Master’s thesis, 2020, Delft University of Technology.

[18] J. Heiligers and C. McInnes, “Novel solar sail mission concepts for space weather forecasting,” vol. 152, 01 2014.

[19] D. Barnhart, T. Vladimirova, and M. Sweeting, “Very-Small-Satellite Design for Distributed Space Missions,” *Journal of Spacecraft and Rockets*, vol. 44, no. 6, pp. 1294 – 1306, 2007.

[20] V. Becerra, “Solving complex optimal control problems at no cost with PSOPT,” *Proceedings of the IEEE International Symposium on Computer-Aided Control System Design*, pp. 1391–1396, 2010.

[21] V. Szebehely and W. Jefferys, “Theory of Orbits: The Restricted Problem of Three Bodies,” *American Journal of Physics*, 1968.

[22] A. Farrés, J. Heiligers, and N. Miguel, “Road map to L4/L5 with a solar sail,” *Aerospace Science and Technology*, 2019.

[23] A. Farrés and A. Jorba, “Solar sailing with invariant manifolds in the earth-sun system,” *Proceedings of the International Astronautical Congress, IAC*, vol. 7, no. April, pp. 5323–5333, 2015.

[24] “MATLAB ga: find minimum of function using genetic algorithm.” 2021. Date Accessed: 21-06-2021. [Online]. Available: https://nl.mathworks.com/help/gads/ga.html

[25] M. Vergaaij and J. Heiligers, “Time-optimal solar sail heteroclinic-like connections for an Earth-Mars cycler,” *Acta Astronautica*, vol. 152, pp. 474–485, 2018.

[26] J. Heiligers, J. Fernandez, O. Stohlman, and K. Wilkie, “Trajectory design for a solar-sail mission to asteroid 2016 HO3,” *Astrodynamics*, vol. 3, no. 3, pp. 231–246, 2019.